โครงสร้างระดับอะตอมและสมบัติของพอลิเมอร์ไฮโดรเจล

นางสาวเกษร เมรัตน์

# ATOMISTIC STRUCTURES AND PROPERTIES OF

POLYMER HYDROGEL

Kesorn Merat

A Thesis Submitted in Partial Fulfillment of the Requirements for the

Degree of Doctor of Philosophy in Chemistry

Suranaree University of Technology

Academic Year 2012

ATOMISTIC STRUCTURES AND PROPERTIES OF POLYMER

HYDROGEL

Suranaree University of Technology has approved this thesis submitted in partial fulfillment of the requirements for the Degree of Doctor of Philosophy.

Thesis Examining Committee

_____
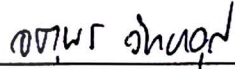
(Assoc. Prof. Dr. Jatuporn Wittayakun)

Chairperson

_____

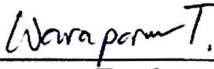(Asst. Prof. Dr. Visit Vao-soongnern)

Member (Thesis Advisor)

_____

(Prof. Dr. Kritsana Sagarik)

Member

_____

(Asst. Prof. Dr. Siriporn Jungsuttiwong)

Member

_____

(Dr. Waraporn Tanthanuch)

Member

_____

(Prof. Dr. Sukit Limpijumnong)

Vice Rector for Academic Affairs

_____

(Assoc. Prof. Dr. Prapun Manyum)

Dean of Institute of Science

เกษร เมรัตน์ : โครงสร้างระดับอะตอมของพอลิเมอร์ไฮโดรเจล (ATOMISTIC STRUCTURES AND PROPERTIES OF POLYMER HYDROGEL) อาจารย์ที่ปรึกษา : ผู้ช่วยศาสตราจารย์ ดร.วิสิษฐ์ แววสูงเนิน, 178 หน้า.

วัตถุประสงค์หลักของงานวิจัยนี้คือศึกษาโครงสร้างระดับอะตอมและระดับโมเลกุลของ พอลิเมอร์ไฮโดรเจลที่ก่อเจลด้วยการเติมไอออน หรือแบบกายภาพที่เกิดจาก "topological entanglement" ระหว่างพอลิเมอร์แบบวงและแบบสายโซ่ตรง โดยใช้วิธีทางการทดลองและการ จำลองแบบโมเลกุลด้วยคอมพิวเตอร์ ซึ่งงานวิจัยนี้ได้แบ่งออกเป็น 3 ส่วนหลักๆ คือ

งานในส่วนแรก ใช้เทคนิคการจำลองแบบโมเลกุลด้วยคอมพิวเตอร์โดยเทคนิคโมเลกุลาร์ ไดนามิคส์ (Molecular Dynamics (MD) Simulation) และเทคนิค extended X-ray absorption fine structure (EXAFS) spectroscopy ศึกษาโครงสร้างระดับอะตอมของแคลเซียม ไอออน ในตัวทำลาย ที่มีขนาดโมเลกุลเล็ก ได้แก่ น้ำ เอทานอล และไอโซโพรพานอล เพื่อที่จะได้ข้อมูลพื้นฐานของ ระบบที่ซับซ้อนมากขึ้นอย่างระบบของพอลิเมอร์/เกลือไฮโดรเจล จากนั้นศึกษาระบบพอลิเมอร์ สังเคราะห์คือ พอลิไวนิลแอลกอฮอล์ (poly(vinyl alcohol), PVA) และพอลิอะไครลิกแอซิด (poly(acrylic acid), PAA) จากนั้นเป็นระบบพอลิเมอร์ธรรมชาติ คือ เพคติน (pectin) และอัลจิเนต (alginate) ผลการศึกษาพบว่า ทั้งในตัวทำลายที่มีขนาดโมเลกุลเล็ก และพอลิเมอร์ มีการล้อมรอบ แคลเซียมไอออนเพียงหนึ่งชั้นที่สังเกตได้ชัดเจน โดยพบว่าอะตอมของออกซิเจนเท่านั้นที่ล้อมรอบ แคลเซียมไอออนใน first coordination shell โดยไม่พบ "Ca^{2+}–Cl^- contact ion pairs" ภายใต้สภาวะ ที่ใช้ในการศึกษาครั้งนี้ สำหรับระบบของพอลิเมอร์ธรรมชาติ คือ เพคติน และอัลจิเนต พบว่า แคลเซียมไอออนเข้าไปแทรกอยู่ระหว่างสายโซ่พอลิเมอร์ 2 สายโซ่ ซึ่งส่งผลให้เกิดโครงสร้างที่มี ความเสถียรระหว่างแคลเซียมไอออนและสายโซ่พอลิเมอร์

งานในส่วนที่สอง ศึกษาพอลิเมอร์ไฮโดรเจลแบบแผ่นฟิล์มที่ได้จากการผสมพอลิเมอร์สอง ชนิด คือ PVA กับ PAA เตรียมตัวอย่างโดยใช้อัตราส่วนพอลิเมอร์ หลายๆ อัตราส่วน ผลจากการ วิเคราะห์ FTIR แสดงให้เห็นว่ามีพันธะไฮโดรเจน และพันธะเอสเทอร์ เกิดขึ้นระหว่าง PVA และ PAA การบวมตัวของแผ่นฟิล์มจะลดลงเมื่อปริมาณของ PVA เพิ่มขึ้น อาจเนื่องมาจากอันตรกิริยา ระหว่างหมู่ OH และหมู่ COOH เกิดเป็นพันธะเอสเทอร์ ซึ่งเป็นการลดจำนวนหมู่ที่ชอบน้ำ (COOH) แต่เพิ่มจำนวนของการเชื่อมโยงระหว่างสายโซ่พอลิเมอร์

งานในส่วนที่สาม แบบจำลองของไฮโดรเจลแบบกายภาพที่เกิดขึ้นระหว่างพอลิเมอร์แบบ สายโซ่ตรง และแบบวงของพอลิเอทิลลีนออกไซด์ ((poly(ethylene oxide), PEO)) ศึกษาโครงสร้าง โดยการจำลองแบบโมเลกุลด้วยคอมพิวเตอร์เทคนิคมอนติคาร์โล (Monte Carlo (MC) simulation)

ซึ่งในการศึกษาครั้งนี้จะใช้เทคนิคที่เรียกว่า coarse-grained model และทำการศึกษาแบบจำลองโมเลกุลของพอลิเมอร์บนแลตทีช (lattice) ผลการศึกษาพบว่า สำหรับระบบ Pure Polymer นั้นพอลิเมอร์แบบสายโซ่ตรง (linear PEO) มีขนาดโมเลกุลใหญ่กว่าพอลิเมอร์แบบวง (cyclic PEO) ประมาณ 2 เท่า โดยสายโซ่พอลิเมอร์ที่มีน้ำหนักโมเลกุลสูงๆ นั้น พอลิเมอร์แบบวงมีค่าสัมประสิทธิ์การแพร่ (diffusion coefficients) มากกว่าพอลิเมอร์แบบสายโซ่ตรง ส่วนระบบพอลิเมอร์ผสม (polymer blends) ของพอลิเมอร์แบบสายโซ่ตรงและพอลิเมอร์แบบวง ค่าสัมประสิทธิ์การแพร่ของพอลิเมอร์ทั้งสองแบบ (สายโซ่ตรงและแบบวง) ลดลงเมื่ออัตราส่วนของพอลิเมอร์แบบสายโซ่ตรงเพิ่มขึ้น ซึ่งการเคลื่อนที่ของพอลิเมอร์แบบวงที่อยู่ในพอลิเมอร์แบบวงด้วยกันเองสามารถเคลื่อนที่ได้เร็วกว่าเมื่ออยู่ในพอลิเมอร์แบบสายโซ่ตรง โครงสร้างของโมเลกุลของเมทริกซ์ (matrix) มีอิทธิพลต่อการเคลื่อนที่ของพอลิเมอร์แบบวง

สาขาวิชาเคมี

ปีการศึกษา 2555

ลายมือชื่อนักศึกษา _____

ลายมือชื่ออาจารย์ที่ปรึกษา _____

ลายมือชื่ออาจารย์ที่ปรึกษาร่วม _Warapcin T,_

KESORN MERAT : ATOMISTIC STRUCTURES AND PROPERTIES OF
POLYMER HYDROGEL. THESIS ADVISOR : ASST. PROF. VISIT
VAO-SOONGNERN, Ph.D. 178 PP.

KEY WORD/ MOLECULAR DYNAMICS/EXAFS/CALCIUM ION/MONTE
CARLO/CYCLIC POLYMER

The main objective of this research was to study structures of polymer hydrogel
induced by either cation or physical network caused by chain topolygical
entanglement between linear and cyclic polymers at both atomistic and molecular
levels by experiment and computer simulation. This research work had been divided
into three main parts.

In the first part, Molecular Dynamics (MD) simulation and the extended X-ray
absorption fine structure (EXAFS) spectroscopy were employed to obtain the
atomistic solvation structure of calcium ion (Ca^{2+}) in small solvent molecules,
including water, ethanol, and isopropanol, in order to gain the basic background of
more complicated polymer/salt hydrogel system. Next, two synthetic polymer
hydrogels induced by Ca^{2+} were studied (i.e. poly(vinyl alcohol) (PVA) and
poly(acylic acid) (PAA)). Then, two natural polysaccharide hydrogels induced by
Ca^{2+} ions were also studied (i.e. pectin, and alginate). The results indicated that there
was only one dominant shell from mainly oxygen atoms from solvent molecule or
polymer to surround the Ca^{2+}. There was no evidence for the formation of significant
numbers of Ca^{2+}–Cl^- contact ion pairs under the condition of this study. In addition,
for Ca^{2+} in pectin and alginate hydrogel system, Ca^{2+} were trapped within the

chelation structure between polyuronate (pectin and alginate) that corresponded to a stable Ca^{2+}/polyuronate complex formation.

In the second part, hydrogel films based on PVA and PAA blend, with various blend composition were prepared. FTIR spectra analysis suggests that there were interaction i.e. hydrogen bonds and ester bonds forming in PVA/PAA blends system. Swelling property of the films showed that the swelling ratio decreased with increasing PVA. This was because the interaction between OH and COOH forming ester bonds were decreased the number of hydrophilic COOH and increased the number of nodes of networks.

In the third part, the model of physical hydrogel caused by the network formation between linear and cyclic polymers (poly(ethylene oxide), PEO) was studied by Monte Carlo simulation of coarse-grained PEO model on a modified diamond lattice. For the pure system, the results suggested that linear PEO had almost twice the size of cyclic PEO. The diffusion coefficient of cyclic molecules was higher than that of linear chains for high molecular weight. For the blend of cyclic/linear PEO, the diffusion coefficient of both cyclic and linear PEO decreased as the linear fraction increases. The diffusion coefficients of cyclic in cyclic (C/C) matrix were larger than cyclic in linear (C/L) matrix. The molecular topology of the matrix have an influence on the diffusion of cyclic polymers.

School of Chemistry   Student's Signature _____

Academic Year 2012   Advisor's Signature _____

                                      Co-advisor's Signature _____

ACKNOWLEDGEMENTS

CONTENTS

CONTENTS (Continued)

CONTENTS (Continued)

CONTENTS (Continued)

CONTENTS (Continued)

CONTENTS (Continued)

LIST OF TABLES

LIST OF TABLES (Continued)

LIST OF FIGURES

LIST OF FIGURES (Continued)

LIST OF FIGURES (Continued)

LIST OF FIGURES (Continued)

LIST OF FIGURES (Continued)

LIST OF FIGURES (Continued)

LIST OF FIGURES (Continued)

LIST OF FIGURES (Continued)

LIST OF FIGURES (Continued)

LIST OF FIGURES (Continued)

LIST OF ABBREVIATIONS

Å	=	angstrom
Ca^{2+}	=	calcium ion
Cl^-	=	chloride ion
CN	=	coordination number
D	=	diffusion coefficient
DSC	=	differential scanning calorimeter
eV	=	electron volt
EXAFS	=	extended X-ray absorption fine structure
$E\sigma, E\omega$	=	the first-, second-order short-range interaction energies
G'	=	storage modulus
G''	=	loss modulus
g ($g+$, $g-$)	=	*gauche* (*gauche* plus, *gauche* minus)
g(r)	=	pair correlation function
LJ	=	lennard-jones
m	=	molallity, mol/kg
MC	=	monte carlo
MD	=	molecular dynamics
MCS	=	monte carlo step
MSD	=	mean square displacement
NPT	=	isothermal-isobaric ensemble

LIST OF ABBREVIATIONS (Continued)

NVT	=	canonical ensemble
PAA	=	poly(acrylic acid)
PEO	=	poly(ethylene oxide)
PVA	=	poly(vinyl alcohol)
R_0	=	center of peak
Ref	=	references
RIS	=	rotation isomeric state
RDF	=	radial distribution function
$<R_g^2>$	=	mean square radius of gyration
SNND	=	2nnd second nearest neighbor diamond
t	=	(1) time, (2) *trans* conformation
Tg	=	glass transition temperature
Tm	=	melting temperature
U	=	statistical weight matrix
XRD	=	X-ray diffraction
ρ	=	density
$\chi(E)$	=	fine structure factor as a function of X-ray energy, E
$\mu(E)$	=	absorption coefficient as a function of X-ray energy, E
$\chi(k)$	=	fine structure factor as a function of wave-vector, k
$\chi(R)$	=	real-space representation of EXAFS spectrum

CHAPTER I

INTRODUCTION

Hydrogels are hydrophilic three-dimensional polymer networks that can absorb water or biological fluids and swell several times of their dry volume. Because of their water-absorbing capacity, hydrogels are a subject of investigation of researchers interested in fundamental aspects of swollen polymeric networks.

The first synthetic hydrogels have been synthesize by using poly (2-hydroxyethyl methacrylate) (PHEMA) that use as contact lenses (Wichterle and Lim, 1960). The growth of hydrogel technologies has advanced many fields ranging from food additives to pharmaceuticals to biomedical implants (Corkhill, Hamilton, and Tighe, 1989; Chen *et al.*, 1995; Kashyap, Kumar, and Kumar, 2005). Due to the high level of water in their composition and their elastic structure, hydrogels are considered as excellent biocompatible materials (Peppas, Bures, Leobandung, and Ichikawa, 2000). There are numerous applications of hydrogels in the medical and pharmaceutical sectors, such as contact lenses, membranes for biosensors and drug delivery devices (Hoffman, 2002; Peppas, Hilt, Khademhosseini, and Langer, 2006; Huynh *et al.*, 2008).

The well-known synthetic polymer hydrogels used as biomedical materials are poly(vinyl alcohol) (PVA) and poly(acrylic acid) (PAA) (Kurkuri and Aminabhavi, 2004; Hasimi, Stavropoulou, Papadokostaki, and Sanopoulou, 2008; Juntanon, Niamlang, Rujiravanit, and Sirivat, 2008). PVA is a candidate of the drug matrix

because of its biocompatibility, non-toxicity, good water permeability, and easy handling under swelling condition. PVA and PAA can form hydrogels by chemical cross-linking or physical cross-linking. PAA have been incorporate into PVA backbone by the formation of a sequential interpenetrating network (IPN) crosslinked with glutaraldehyde to obtain pH-sensitive polymeric matrix for drug controlled release application (Kurkuri and Aminabhavi, 2004). The proposed structure of PVA with calcium ion (Ca^{2+}) complex is shown in Figure 1.1.
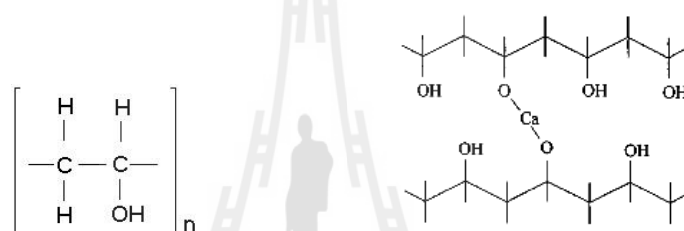
Figure 1.1 Repeating unit of poly(vinyl alcohol) (left) and examples of O-Ca-O linking in the interaction of calcium ion with PVA (right).

Furthermore, attention also been focused on the development of biodegradable, pH-sensitive hydrogels based on biopolymers such as polysaccharides (Sriamornsak and Kennedy, 2008; Hua, Ma, Li, Yang, and Wang, 2010). In recent years, biomedical and pharmaceutical industries have shown increased interest in this group of biopolymers. In view of their abundance and biocompatibility, natural polymers such as polysaccharides have been used in drug delivery systems. Among such natural polymers, alginate and pectin are water-soluble polysaccharide having a good hydrogel property, which can be readily crosslinked with glutaraldehyde or divalent as Ca^{2+}.

Understanding the mechanism of gel at an atomic level is important for controlling physical properties that required for applications. Structural details of ordered domains of gelling-networks were obtained from solid state X-ray diffraction studies and circular dichroism of solutions and films. The possibility of performing Extended X-ray Absorption Fine Structure (EXAFS) experiments directly on gels using synchrotron radiation, prompted us to use this technique to investigate the geometrical features of the binding sites of calcium atoms in polymer hydrogel.

Molecular modeling of ion–polymer interaction is important to understand the chemical and physical properties of hydrogel induced by multivalent cation. Molecular dynamics (MD) simulation technique provides a powerful approach to probe such processes in condensed phase environments. A detailed description of the solvent structure around the ion in solution can be obtained from a variety of experimental and theoretical techniques. MD simulations provide a detailed picture of structure and dynamics for complex systems that may not be tractable by other methods.

Due to the advancement of modern EXAFS algorithms and the availability of more accurate ion and solvent potential models, the number of studies that combine MD with EXAFS has increased considerably (D'Angelo, Di Nola, Filipponi, Pavel, and Roccatano, 1994; Roccatano, Berendsen, and D'Angelo, 1998). The accuracy of the existing theoretical models for the interatomic potential in solid and liquid of simple ionic systems was discussed in direct comparison of EXAFS and molecular-dynamics (MD) results (Di Cicco *et al.*, 1996).

On the other hand, the network-like structure can be formed by threading of linear chains through cyclic polymer. These structures are predicted to have

interesting properties that differ from the properties of the initial starting materials, because of the unique nature of these structures and the lack of a covalent bond between the cyclic and linear components. Very shortly after the first reports on the synthesis of polymer rings, their melt dynamics in blends with linear polymers were characterized (Antonietti, Coutandin, Gruetter, and Sillescu, 1984; Roovers, 1988; Cosgrove *et al.*, 1996), and found that for cyclic polymer, viscosity (η) increased rapidly on addition of small amounts of linear polymer. This lack of mobility was attributed to threading of the rings by chains during sample preparation as the solution concentration slowly increased.

To better understand the static and dynamic properties of topological polymer mixture. A computational study, Monte Carlo (MC) simulation methods was used to study the structure of cyclic/linear polymer. Poly(ethylene oxide) PEO was chosen as the subject of this study for variety of reason. (1) Linear POE has low entanglement molecular weight (Me ~ 2 kg/mol) and critical molecular weight for entanglement (Mc ~ 5.87 kg/mol), which means that unentangled and entangled regimes can be studied without simulated high-MW molecules with large box size that cause time consuming. (2) PEO structure is not too complicated for mapping in to coarse-grained beads and (3) the melt dynamics of cyclic POE or its blends with linear had not yet been reported.

In this research, MD simulations of Ca^{2+} in water, ethanol, isopropanol, alginate, pectin, poly(vinyl alcohol) and poly(acrylic acid) have been performed to obtain their structural details. Theoretical EXAFS spectra were also computed. The simulated MD-EXAFS spectra were compared with the EXAFS experimental result. Moreover, coarse-grained MC simulations were performed to investigate the

properties of linear and cyclic PEO. The influences of molecular weight and composition on the melt dynamics in blends of POE chains and rings were studied.

Research objective

To study structures and properties of physical and chemical polymer hydrogel network at the atomistic and molecular level.

Scope and limitations

This research work has divided into 3 main parts, including

- Molecular dynamics (MD) simulation and EXAFS measurement of Ca^{2+} in water, Ethanol, isopropanaol, PVA, PAA, Pectin and Alginate. Molecular Dynamic Simulation methods were employed to determine the atomistic structures such as distance between pair atoms, coordination number and to predict EXAFS spectra of these hydrogels induced by cation ie. Ca^{2+}/H_2O, $Ca^{2+}/Ethanol$, $Ca^{2+}/Isopropanol$, Ca^{2+}/PVA, Ca^{2+}/PAA, $Ca^{2+}/Pectin$ and $Ca^{2+}/Alginate$ to compare with EXAFS spectra from experiment.

- Preparation and Characterization of PVA/PAA hydrogel systems. This section, this hydrogel were prepared by thermal treatment to study their characteristics and swelling properties

- Monte Carlo simulation of linear and cyclic poly(ethylene oxide) in the melt state. This section, a new lattice-based Monte Carlo method developed by Vao-soongnern and Mattice for coarse-grained model of physical polymer network (linear and cyclic PEO mixture with monodisperse and bidisperse molecular weight) was employed to investigate the static and dynamic properties.

CHAPTER II

LITERATURE REVIEW

2.1 Polymer Hydrogel

Polymer hydrogels can contain a large amount of water while remaining insoluble in aqueous solutions due to chemical or physical crosslinking of individual polymer chains. Polymer hydrogels is a flexible molecular structure and it can be restored to original shape after extension (Jiang, Su, Mather, and Bunning, 1999; Sandolo, Matricardi, Alhaique, and Coviello, 2009). In polymeric network, hydrophilic groups or domains are present which are hydrated in an aqueous environment thereby creating the hydrogel structure, the crosslinks have to be present to avoid dissolution of the hydrophilic polymer chains/segments into the aqueous phase (Nguyen and West, 2002; Roy and Gupta, 2003). Properties of polymer hydrogels are dependent on their structure and type of crosslink. Hydrogel synthesis can be divided into 2 categories; physical and chemical cross-linking strategies.

2.1.1 Type of Polymer Hydrogel

Chemical gels or "permanent" gels are covalently-crosslinked networks (Hoare and Kohane, 2008). Chemical hydrogels may be generated by cross-linking of water-soluble polymers, or by conversion of hydrophobic polymers to hydrophilic polymers plus cross-linking to form a gel network. The crosslinked hydrogels reach an equilibrium swelling level in aqueous solutions which depends mainly on the

crosslink density estimated by the molecular weight between crosslinks, M_c (Ponomariova, Melnichenko, Albouy, and Rault, 1997).

Physical gels or "reversible" gels, are formed by the non-covalent cross-linked among polymer chains. When polymer networks are held together by molecular entanglements, or secondary forces such as ionic interaction, they are called physical gels (Hoare and Kohane, 2008). All of these interactions are reversible, and can be disrupted by changing in physical conditions such as ionic strength, temperature or application of stress.

(a)   (b)
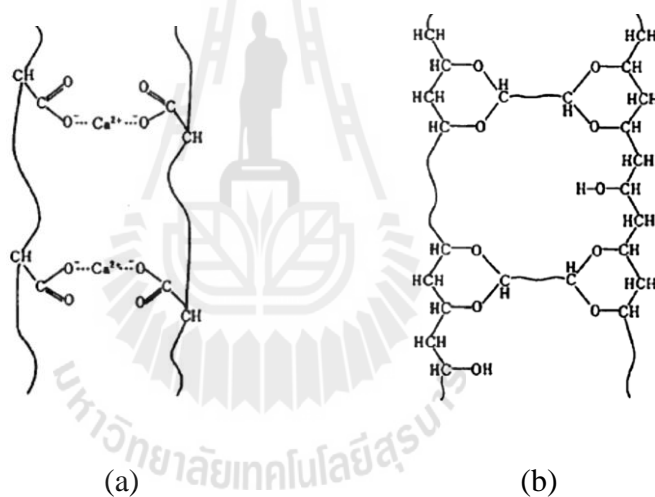
Figure 2.1 Schematic representations showing the physical (a) and chemical (b) crosslinking.

Physical crosslinking of polymer chains can be achieved using a variety of environmental triggers (pH, temperature,) and a variety of physicochemical interactions (hydrophobic interactions, charge condensation, hydrogen bonding, stereocomplexation, or supramolecular chemistry).

Charge interactions have been widely investigated for crosslinking in situ gelling polymers. One advantage of this approach is that biodegradation can occur as ionic species in extracellular fluid bind competitively with the gel components, breaking down the cross-linked network. Cross-linking (or decrosslinking) can also be triggered by pH changes which ionize or protonate the ionic functional groups that cause gelation. Charge interactions may occur between a polymer and a small molecule or between two polymers of opposite charge to form hydrogel (Lim, Nettles, Setton and Chilkoti, 2007; Chen, 2005).

2.1.2 Polymer Hydrogel Swelling

The favorable property of hydrogels is their ability to swell, when put in contact with a thermodynamically compatible solvent. When a hydrogel in its initial state is in contact with solvent molecules, the latter attacks the hydrogel surface and penetrates into the polymeric network. In this case, the unsolvated glassy phase is separated from rubbery hydrogel region with a moving boundary. Regularly the meshes of the network in the rubbery phase will start expanding, allowing other solvent molecules to penetrate within the hydrogel network (Ganji, Vasheghani-Farahani, and Vasheghani-Farahani, 2010).

The swelling behavior of polymer hydrogel is typically observed by immersing the specimens of dried gels (or hydrogel containing a small content of water) into an aqueous solution at a predetermined temperature and monitoring their mass and volume change with time (Ritger and Peppas, 1987; Ghi, Hill, and Whittaker, 2000). The volume (q_v) and mass (q_m) swelling ratio are defined using the following equations:

$$q_m = \frac{m_s}{m_d} \qquad\qquad (2.1)$$

$$q_v = \frac{V_s}{V_d} \qquad\qquad (2.2)$$

where m_d is the mass of the dry gel, m_s is that of the swollen hydrogel at a time, V_d is the volume of the dried gel and of V_s is that of the swollen hydrogel at a specific time.

2.1.3 Poly(vinyl alcohol)

Poly(vinyl alcohol), PVA, is the product of free radical polymerization of vinyl acetate with subsequent hydrolysis of acetate groups to hydroxyl groups. PVA is among the most promising polymer candidates for hydrogel studies. Crosslinking of PVA polymeric chains is carried out using chemical (e.g., crosslinking agents, electron beam, γ-irradiation) as well as physical (e.g., freezing/thawing) methods, with the crosslinks being critical for PVA in order to be useful for various applications in medical and pharmaceutical fields (Westedt *et al.*, 2007).
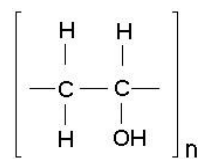
Figure 2.2   Repeating unit of poly(vinyl alcohol).

2.1.4 Poly(acrylic acid)

Poly(acrylic acid), PAA, is a homopolymer including acrylic acid repeating unit. There are several ways to crosslink PAA, such as gamma radiation (Jabbari and Nozari, 2000), and heat treatment (Manavi-Tehrani, Rabiee, Parviz, Tahriri, and

Fahimi, 2010). Hydrogel networks formed from PAA have the ability to absorb many times their weight in water and are the basis of a class of materials called super absorbents. These polymers are used in many applications including diapers and personal hygiene products, ion exchange resins, membranes for hemodialysis and ultrafiltration and controlled release devices (Gudeman and Peppas, 1995; Ende and Peppas, 1996). The ability of PAA to swell extensively is facilitated by the carboxylic acid groups on the polymer chain, which strongly associate with water molecules. These groups are readily ioniziable and sensitive to the effects of pH and ionic strength. Thus, the equilibrium swelling of PAA hydrogels is affected by the pH and ionic strength of the solution in which they are swelling (Shefer, Grodzinsky, Prime, and Busnel, 1993; Eichenbaum, Kiser, Dobrynin, Simon, and Needham, 1999).
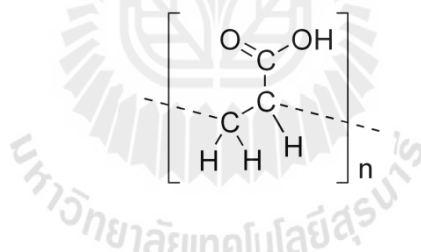
Figure 2.3   Repeating unit of poly(acrylic acid).

2.1.5   Pectin

Pectin is a heterogeneous grouping of acidic structural polysaccharides. Figure 2.4 displays the majority of the structure consists of homopolymeric partially methylated poly-α-(1$\longrightarrow$4)-D-galacturonic acid residues (Andrade, Raphael, and Pawlicka, 2009). The properties of pectin depend on the degree of esterification. High methoxyl-pectins (>50% esterified) gel formed by hydrogen-bonding and hydrophobic interactions in the presence of acids and sugars. Low methoxyl-pectins

(<40% esterified) gel by Ca^{2+} bridging between adjacent two-fold helical chains forming so-called "egg-box" structures. If the methoxyl esterified content is greater than about 50%, Ca^{2+} show some interaction but do not gel. The rheological properties of low methoxy-pectins are highly dependent on the salt cation, salt concentration and pH. Gel strength increases with increasing Ca^{2+} concentration but reduces with temperature and acidity increase.
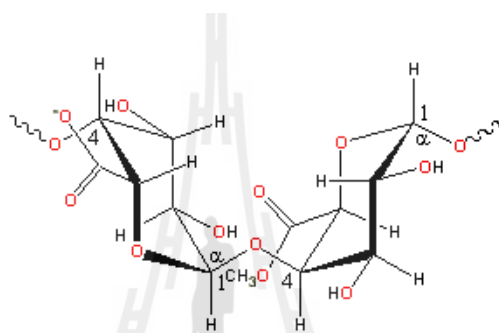
Figure 2.4 Chemical structure of pectin showing a polymer chain of α-(1⟶4)-D-
galacturonosyl sections linkages.

2.1.6 Alginate

Alginate is also water-soluble polysaccharide and is composed of alternating blocks of 1–4 linked α-l-guluronic and β-d-mannuronic acid residues. Figure 2.5 (Lee and Yuk, 2007) shows the structures of mannuronic and guluronic acid residues and the binding between these residues in alginate. The most important property of alginates is their ability to form gels by reaction with divalent cations such as Ca^{2+} (Rhim, 2004), and the stacking of guluronic groups to form the characteristic egg-box structure shown in Figure 2.6. The gel network are formed when each alginate chain form junctions with many other chains. This junction can be either temporary or permanent, depending on the amount of calcium present in the system. Temporary

associations are obtained with low levels of Ca^{2+}, giving rise to highly viscous solutions. The permanent associations are obtained with high calcium levels.
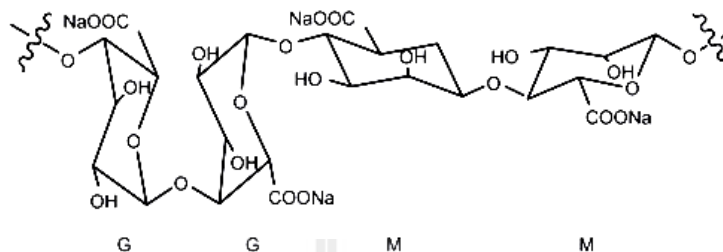
Figure 2.5 Chemical structure of alginate. Shown is a polymer chain of 2 guluronic acid (G) monomers and 2 mannuronic acid (M) monomers, with (1–4) linkages.
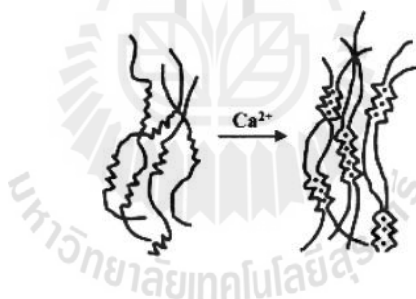
Figure 2.6 Egg-box structure of an alginate gel formed by chelation of Ca^{2+} ions.

2.1.7 Poly(ethylene oxide)

Linear poly(ethylene oxide), PEO, are prepared by polymerization of ethylene oxide. Crosslinking of PEO polymeric chains is carried out using chemical e.g., γ-irradiation (Stringer and Peppas, 1996) as well as physical e.g., supramolecular hydrogels methods (Huh *et al.*, 2001). A supramolecular system is composed of two or more molecular entities held together and organized by means of intermolecular

non-covalent binding interactions. PEO hydrogels can be crosslinked using alpha-cyclodextrin to form a reversible hydrogel (Huh *et al.*, 2001; Li and Leong, 2003).

$$-\left(CH_2CH_2O\right)_n-$$
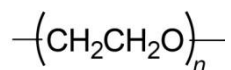
Figure 2.7 Repeating unit of linear poly(ethylene oxide).

Cyclic PEO is cyclic polyether and can be regarded as a polymeric homologue of crown ethers (Figure 2.8). In general, cyclic PEO have been prepared in the laboratory by Williamson etherification reactions, either by reaction of a hydroxyl-terminated PEO with a PEO ditosylate derivative in the presence of a base, (Gibson *et al.*, 1994) or by reaction of a hydroxyl-terminated PEO, which already has the required number of oxyethylene units, with arenesulfonyl chlorides and heterogeneous KOH or NaOH (Sun *et al.*, 1995; Ishizu and Akiyama, 1997).

$$\left(CH_2CH_2O\right)_n$$
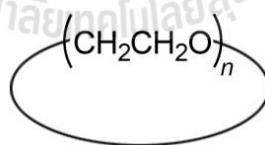
Figure 2.8 Repeating unit of cyclic poly(ethylene oxide).

2.2 Basic Principle of Differential Scanning Calorimetry

Differential scanning calorimetry (DSC) is a technique which is part of a group of techniques called Thermal Analysis (TA). Thermal Analysis is based upon the detection of changes in the heat content (enthalpy) or the specific heat of a sample

with temperature. DSC measures the difference in the heat flow rate of a sample and a reference over a controlled temperature range. These measurements are used to create phase diagrams and gather thermoanalytical information such as transition temperatures and enthalpies.
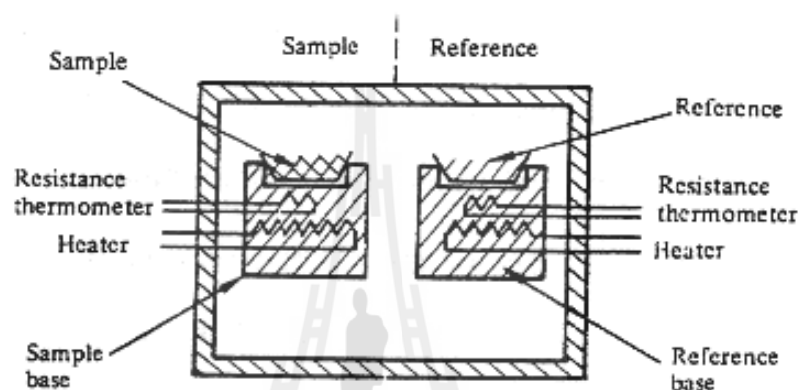
Figure 2.9 DSC experimental arrangements.

Figure 2.9 shows the DSC Experimental Arrangement. The sample and reference are placed in identical environments, metal pans on individual bases each of which contain a platinum resistance thermocouple or thermometer and a heater. The temperatures of the two thermocouples are compared, and the electrical power supplied to each heater adjusted so that the temperatures of both the sample and the reference remain equal to the programmed temperature, i.e. any temperature difference which would result from a thermal event in the sample is 'nulled'. The ordinate signal, the rate of energy absorption by the sample, is proportional to the specific heat of the sample since the specific heat at any temperature determines the amount of thermal energy necessary to change the sample temperature by a given

amount. Any transition accompanied by a change in specific heat produces a discontinuity in the power signal, and exothermic or endothermic enthalpy changes give peaks whose areas are proportional to the total enthalpy change. Changes in the sample that is associated with absorption or evolution of heat cause a change in the differential heat flow which is then recorded as a peak. DSC curves (Figure 2.10) typically consist of the heat flow plotted versus the temperature. The area under the peak is directly proportional to the enthalpic change and its direction indicates whether the thermal event is endothermic or exothermic.
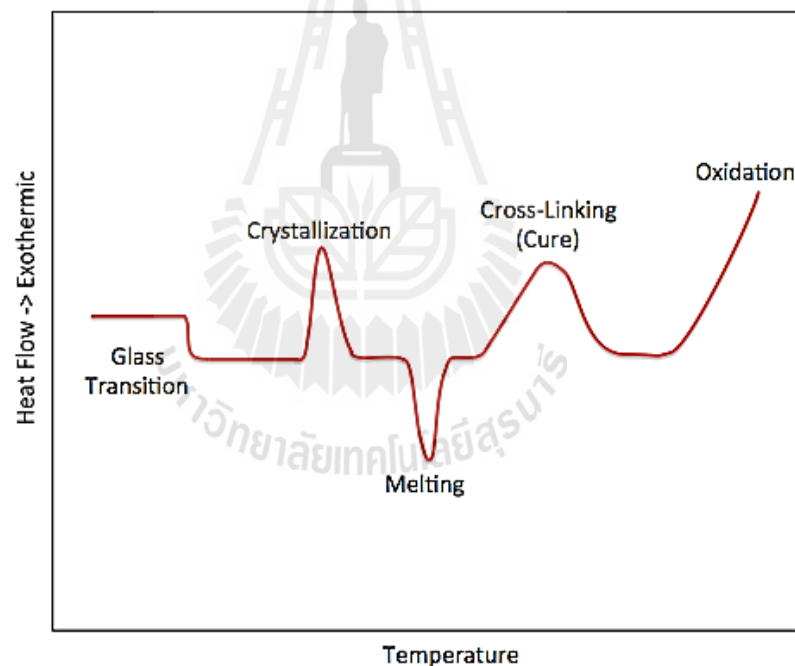
Figure 2.10 Typical DSC curve.

The DSC curve showing endothermic and exothermic effects, it gives information on the type of thermal transformations undergone by the sample. The common endothermic effects including of melting, phase transitions, evaporation,

dehydration, denaturation (protein), pyrolysis etc. There is a particular endothermic transition, called glass transition, which is not giving a peak. Glass transition (or rubbery transition) is related to a variation of the viscoelastic properties of the sample and is detected by a variation of the DSC baseline. This variation corresponds to a change in the heat capacity of the sample. The common exothermic effects including of crystallization, oxidation, decomposition, etc.

DSC is used widely for examining polymeric materials to determine their thermal transitions. The observed thermal transitions can be utilized to compare materials, however, the transitions do not uniquely identify composition. Composition of unknown materials may be completed using a technique such as IR. Melting points and glass transition temperatures for most polymers are available from standard compilations. The percent crystalline content of a polymer can be estimated from the crystallization/melting peaks of the DSC graph as reference heats of fusion.

2.3 Basic Principle of Infrared Spectroscopy

Infrared (IR) spectroscopy is a technique that used to identify and study the structure of molecules. IR spectroscopy deals with the interaction between a molecule and radiation from the mid-infrared region, approximately 4000-400 cm^{-1}, used to study the fundamental vibrations and associated rotational-vibrational structure. IR radiation causes the excitation of the vibrations of covalent bonds within that molecule. These vibrations include the stretching and bending modes. A common laboratory instrument that uses this technique is a Fourier transform infrared (FTIR) spectrometer. An FTIR spectrometer simultaneously collects spectral data in a wide spectral range, improving both speed and signal-to-noise ratio.

Transmission IR techniques, IR radiation is passed through a sample. Some of the infrared radiation is absorbed by the sample and some of it is passed through (Figure 2.11). The resulting spectrum represents the molecular absorption and transmission, creating a molecular fingerprint of the sample. This technique can use for quantitative analysis. However, sample preparation can be difficult.
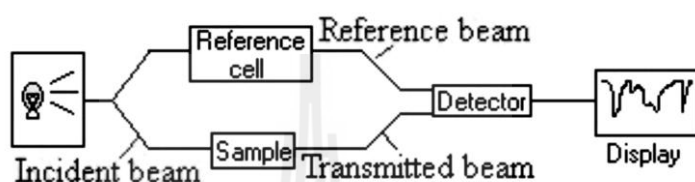
Figure 2.11 Transmission IR techniques.

Nowadays, IR-measurements are mainly performed in attenuated total reflection (ATR) mode as this technique is simpler to use than the conventional transmission mode. All types of samples (e.g. solids, liquids, powders, pastes, pellets, slurries, fibers etc.) are placed undiluted on the ATR crystal. The measurement is typically performed within a few seconds. The basic principle of ATR is shown in Figure 2.12. The ATR crystal comprises an IR transparent material with a high refractive index and polished surfaces as shown in Figure 2.12. As shown in the image, the infrared beam enters the ATR crystal at an angle of typically 45° (relative to the crystal surface) and is totally reflected at the crystal to sample interface. The fraction of light reaching into the sample is known as evanescent wave. Its penetration depth depends on the wavelength, the refractive indices of the ATR crystal and the sample and the angle of the entering light beam. It is typically of the order of a few microns. In the spectral regions where the sample absorbs energy, the evanescent wave is attenuated.

After one or several internal reflections, the IR beam exits the ATR crystal and is directed to the IR-detector.
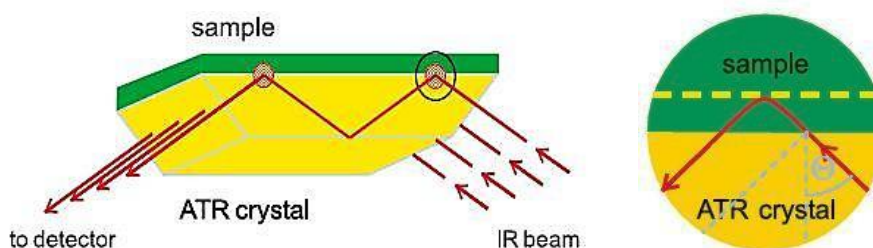
Figure 2.12 ATR principles.

IR spectroscopy is used to identify structures because functional groups give rise to characteristic bands both in terms of intensity and position (frequency). The positions of these bands are show in Appendix. In general terms it is convenient to split an IR spectrum into two approximate regions, 4000-1000 cm^{-1} known as the functional group region, and < 1000 cm^{-1} known as the fingerprint region (Figure 2.13). Most of the information that is used to interpret an IR spectrum is obtained from the functional group region. Hence, the most useful information obtained from an IR spectrum is what functional groups are present within the molecule. However, the fingerprint region can be useful for helping to confirm a structure by direct comparison with a known spectrum.
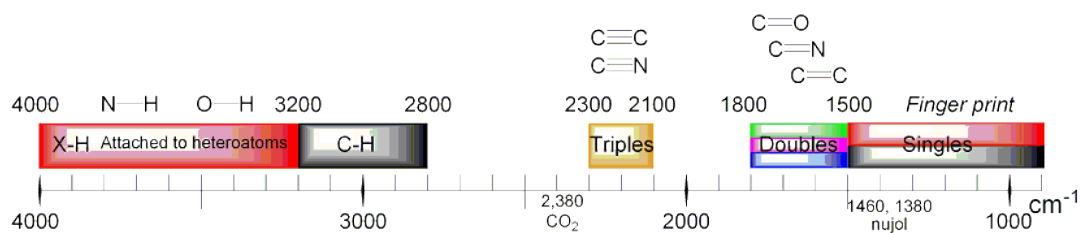
Figure 2.13 The positions of IR bands.

2.4   Basic Principle of Rheology

Rheology is the study of the flow of matter mainly liquids but also soft solids or solids under conditions in which they flow rather than deform elastically. It applies to substances which have a complex structure, including muds, sludges, suspensions, polymers, many foods, bodily fluids, and other biological materials. The science of rheology and the characterization of viscoelastic properties in the production and use of polymeric materials have been critical for the production of many products for use in both the industrial and military sectors.

The combined viscosity and gel behavior (viscoelasticity) can be examined by determining the effect that an oscillating force has on the movement of the material. Rheometer is instrument that measures viscosity over a wide range of shear rates, and viscoelasticity of fluids, semi-solids and solids. Rheometer is based on the relative rotation about a common axis of one of three tool geometries: concentric cylinder, cone and plate or parallel plates (Figure 2.14a, 2.14b and 2.14c respectively). The type of measuring geometry used is specific to the nature of the sample and the flow conditions generated. The cup and bob geometry is used for low viscosity material; the large surface area gives greater sensitivity at lower shear rates. It can often be used for measuring particulate material, since the gap between the bob and the base is noncritical. For higher viscosity samples, a cone and plane or parallel plate is generally used. Where one of the two is stationary and the other rotates. This model resembles twisting a roll of coins causing coins to be displaced by a small angle with respect to adjacent coins. This type of flow is caused in rotational rheometers with the samples placed within the gap of parallel-plate.
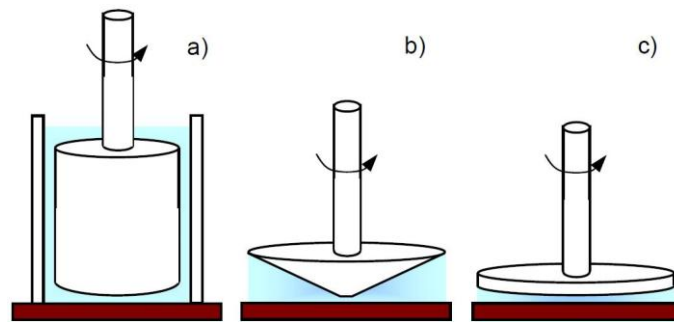
Figure 2.14 Measuring geometries for the rotational rheometer.

Simple deformation and flow: The shear stress (τ), denoted (Greek: tau), is defined as the component of stress coplanar with a material cross section. Shear stress arises from the force vector component parallel to the cross section. The formula to calculate average shear stress:

$$\tau = \frac{F}{A} \tag{2.3}$$

where τ is the stress, F is the force applied, A is the cross-sectional area of material with area parallel to the applied force vector. τ derived SI unit is the pascal (Pa).

The shear strain (γ), denoted (Greek: gamma), is the ratio of the deformation of a body along the loading axis to the original un-deformed length of the body.

$$\gamma = \frac{x(t)}{y_0} \tag{2.4}$$

where $x(t)$ is the transverse displacement measured in meters at the time t, y_0 is the distance between the two parallel plates, measured in meters.

The shear modulus (G) or modulus of rigidity is defined as the ratio of shear stress to the shear strain, measure of materials overall resistance to deformation. G derived SI unit is the pascal (Pa), although it is usually expressed in gigapascals (GPa) or in thousands of pounds per square inch (kpsi). The shear modulus is always positive.

$$G = \text{Stress/Strain} \tag{2.5}$$

$$G = G' + iG'' \tag{2.6}$$

The Elastic (Storage) Modulus (G'): Measure of elasticity of material, the ability of the material to store energy.

$$G' = (\text{stress/strain})\cos\theta \tag{2.7}$$

The Viscous (loss) Modulus: The ability of the material to dissipate energy, energy lost as heat.

$$G'' = (\text{stress/strain})\sin\theta \tag{2.8}$$
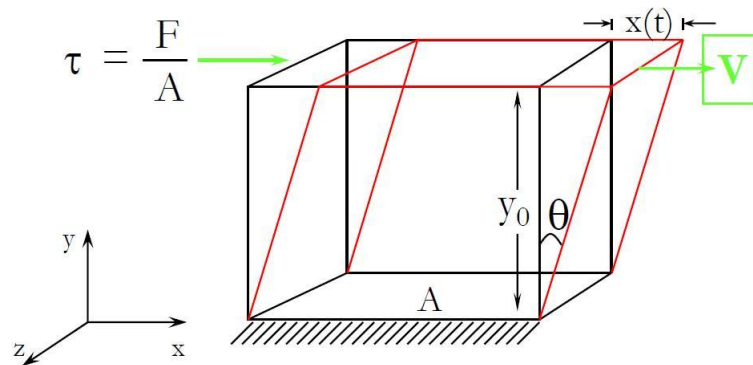
Figure 2.15 Simple shear deformation and shear flow.

2.5 Introduction to Extended X-ray Absorption Fine Structure

X-rays is a form of electromagnetic radiation. X-rays have a wavelength in the range of 0.1 to 10 Å, which is equivalent to the size of atoms and molecules. Thereby it can detect objects at the atomic and molecular level. X-rays is composed of elementary particles called photons, photon energy (E, eV) corresponding to the wavelength (λ, Å) of X-rays by Equation (2.9).

$$E = \frac{12398.2}{\lambda} \tag{2.9}$$

The responses of the object to the X-rays are coming from the interaction between photons and atoms in the material. X-rays are absorbed by all matter through the photo-electric effect. Which: An X-ray is absorbed by an atom when the energy of the X-ray is transferred to a core-level electron (K, L, or M shell) which is ejected from the atom. The atom is left in an excited state with an empty electronic level (a core hole). Any excess energy from the X-ray is given to the ejected photo-electron.

When x-rays are absorbed by the photo-electric effect, the excited core-hole will relax back to a "ground state" of the atom. A higher level core electron drops into the core hole, and a fluorescent X-ray or Auger electron is emitted. X-ray Fluorescence: An X-ray with energy equal to the difference of the core-levels is emitted. Auger Effect: An electron is promoted to the continuum from another core-level. X-ray fluorescence and Auger emission occur at discrete energies that are characteristic of the absorbing atom, and can be used to identify the absorbing atom.

(a) X-ray absorption   (b) Fluorescence X-ray emission   (c) Auger emission
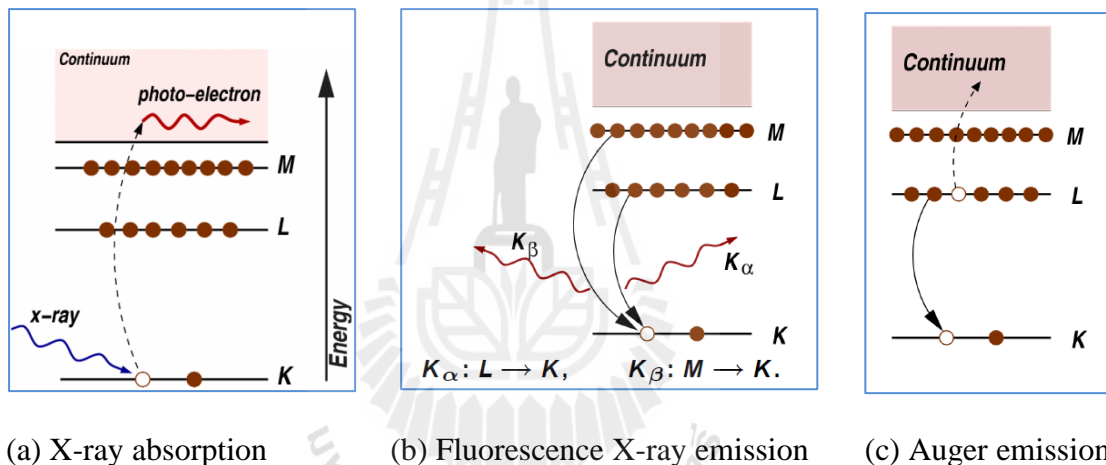
Figure 2.16 (a) X-ray absorption mechanism, (b) Fluorescence X-ray emission and (c) Auger emission (Newville, 2004).

X-ray absorption spectrometry is a technique for analyzing the chemical environment of an element in an unknown material. X-ray absorbance depends on the wavelength of X-rays, atomic number, chemical environment, and concentration of sample. X-rays are absorbed by matter and the intensity is attenuated.

An X-ray Absorption Spectroscopy experiment measures the probability as a function of energy that a material will absorb a photon in a given energy range. The intensity of an X-ray beam passing through a material of thickness t is given by the absorption coefficient μ.

$$I = I_0 e^{-\mu(E)t} \tag{2.10}$$

Where I_0 is the X-ray intensity hitting the material, and I is the intensity transmitted through the material. In addition, μ has sharp Absorption Edges corresponding to the characteristic core-level energies of the atom. In its simplest form, an XAS beam line can be illustrated as Figure 2.17.
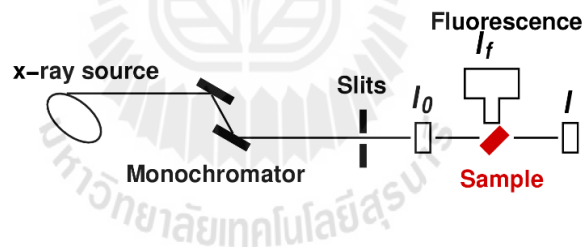
Figure 2.17 Schematic views of XAS beam line (Newville, 2004).

XAS measures the energy dependence of the X-ray absorption coefficient $\mu(E)$ at and above the absorption edge of a selected element. $\mu(E)$ can be measured two ways. Transmission: The absorption is measured directly by measuring what is transmitted through the sample (Equation (2.11)). Fluorescence: The re-filling the deep core hole is detected. Typically the fluorescent x-ray is measured (Equation (2.12)).

$$\mu(E)t = -\ln\left(\frac{I}{I_0}\right) \qquad (2.11)$$

$$\mu(E) \propto I_f/I_0 \qquad (2.12)$$

The X-ray absorption spectrum is typically divided into two regimes: X-ray absorption near-edge spectroscopy (XANES) and extended X-ray absorption fine-structure spectroscopy (EXAFS). XANES contains information about the valence and density of states of the absorber, as well as qualitative structural information. It is strongly sensitive to formal oxidation state and coordination chemistry (e.g., octahedral, tetrahedral coordination) of the absorbing atom. It is interpreted, often by simulation. EXAFS contains detailed information about the local atomic structure. It is used to determine the distances, coordination number and species of the neighbors of the absorbing atom. It can be analyzed by the curve fitting technique.
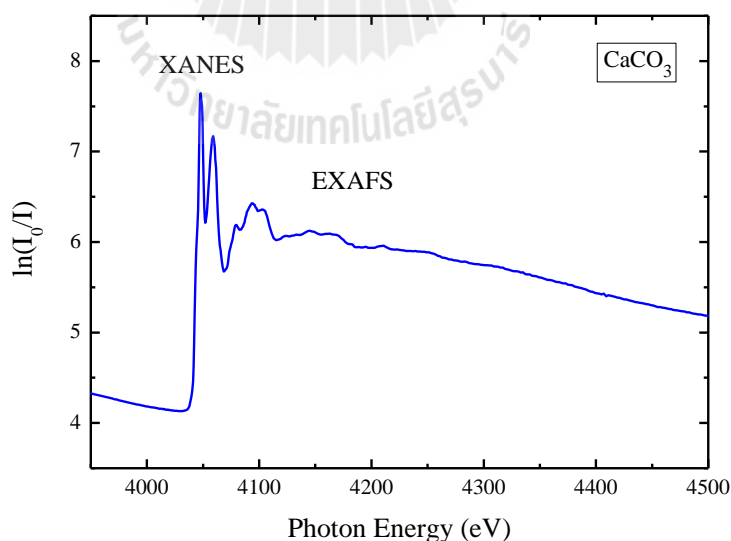
Figure 2.18 X-ray absorption spectra of $CaCO_3$ in the energy range of Cacilum K-edge.

2.6 Molecular Simulation

From the development of the first computers in the early 1950's, scientists have tried to explore how these machines might be used in Chemistry. From the very beginning, the field of computational chemistry focused either on solving complex mathematical problems, typically quantum mechanical, or has tried to model the dynamical behavior of atomic and molecular systems. The boundaries between these two areas have never been well defined and, today, we see a convergence between quantum chemistry and simulation in studying chemical reactions (Curtiss and Gordon, 2004).

Breakthrough in computer technology leading to ever faster computers, computational chemistry has become an increasingly reliable tool for investigating systems where experimental techniques still provide too little information. Ultra-fast spectroscopy can be used to follow fast reactions but only at a molecular level. A variety of diffraction techniques can also give detailed information about crystalline structure, but have difficulties monitoring changes at a molecular level. This is why the exponential growth in computer power has led to a corresponding growth in the number of computational chemists and in the variety of different computational techniques available for solving chemical problems: ab initio Quantum Mechanics (QM), Density Functional Theory (DFT), semi-empirical methods, Molecular Mechanics (MM), Monte Carlo (MC), Molecular Dynamics (MD), etc.

There are two main branches within computational chemistry: the computationally expensive methods which try to explore the electronic structure of small systems or systems with fixed crystal structures by quantum mechanical methods; and the methods which focus on the atomic structure and dynamics of much

larger systems but using less complex calculations. In this thesis, the focus is on the latter – simulating atomic and molecular interaction with the mathematics of classical mechanics (Allen, 1987).

2.7 Molecular Dynamics Simulation

In reality, atoms and molecules in solid materials are far from static unless the temperature is low; but even at 0 K, vibrational motion remains. Molecular Dynamics (MD) allows us to simulate the dynamics of the particles in a well-defined system to gain greater insights into local structure and local dynamics – such as ion transport in solid materials. In MD simulation, atomic motion in a chemical system is described in classical mechanics terms by solving Newton's equations of motion:

$$\vec{F}_i = m_i \vec{a}_i \tag{2.13}$$

for each atom i in a system of N atoms: m_i is their respective atomic mass; $a_i = d^2 r_i / dr^2$ is their acceleration; and $\vec{F}_i$ is the force acting upon atom i due to interactions with all other particles in the system. The forces are generated from a universal energy potential E:

$$-\frac{dE}{d\vec{r}_i} = \vec{F}_i = m_i \frac{d^2 \vec{r}_i}{dt^2} \tag{2.14}$$

With Newton's equations, it is possible to calculate sequentially the locations and velocities of all particles in the system. This generates a sequence of snapshots

which constitutes a "movie" of the simulated system on the atomic scale. Due to the massive computer time necessary to solve these equations for a large number of particles, the movies are generally fairly short – in this work in the pico- or nanosecond regime. All that is needed to solve the equations of motion are the masses of the particles and a description of the potentials, E.

The MD simulation method is very straightforward, but one must bear in mind that it is based on some severe approximations. At the highest level, the Born-Oppenheimer approximation is made, separating the wavefunction for the electrons from those of the nuclei. The Schrödinger equation can then be solved for every fixed nuclear arrangement, given the electronic energy contribution. Together with the nuclear –nuclear repulsion, this energy determines the potential energy surface, E. At the next level of approximation, all nuclei are treated as classical particles moving on the potential energy surface, and Schrödinger equation is replaced by Newton's equations of motion. At the lowest level of approximation, the potential energy surface is approximated to an analytical potential energy function which gives the potential energy and interatomic forces as a function of atomic coordinates.

2.7.1 Forcefiled for MD Simulation

In the context of molecular modeling, a forcefield means the energy functions and parameter sets used to calculate the potential energy of a system. The energy functions and parameter sets are either derived from quantum chemistry calculations or empirically from experimental data. Typically, classical forcefields employ two-body pairwise additive potentials and ignore multi-body dispersion and many-body polarization effects. The basic functional form of a classical forcefield can be

regarded as the sum of nonbonded interactions, also called intermolecular interactions, and intramolecular interactions (bond stretch, valence angles and dihedral angles):

$$E = \sum_{i \neq j} E_{ij}^{NB}(r) + \sum_{ij} E_{ij}^{s}(r) + \sum_{ijk} E_{ijk}^{b}(\theta) + \sum_{ijkl} E_{ijkl}^{t}(\Phi) \qquad (2.15)$$

Where r is the distance between atom centers, $E_{ij}^{NB}(r)$ is the nonbonded energy associated between atom i and j, $E_{ij}^{s}(r)$ is the covalent bond stretching energy between atom pair i and j, $E_{ijk}^{b}(\theta)$ is the bond-angle bending energy that depends on the angle θ formed by atoms i, j, and k, and $E_{ijkl}^{t}(\Phi)$ is the torsional energy arising from rotation around the dihedral angle Φ defined by atoms i, j, k, and l. Nonbonded interactions $E_{ij}^{NB}(r)$, the interactions between atoms in different molecules or in the same molecules separated by two or more bonds, are composed of electrostatic interactions and van der Waals interactions as given by:

$$E_{ij}^{NB}(r) = E_{ij}^{elec}(r) + E_{ij}^{vdw}(r) \qquad (2.16)$$

The summations run over all interactions of each type present in each molecule and between molecules. The bond-stretching, bond-angle and torsional-angle terms have many forms. In the vast majority of forcefields used in MD simulations, bond breaking is not possible; this is also the case for the forcefields used in this work. The electrostatic energy, E_{ij}^{elec}, also called the Coulombic energy, is directly related to atomic charges by Coulomb's law,

$$E_{ij}^{elec}(r) = \frac{1}{4\pi\varepsilon_0}\frac{q_iq_j}{r} \tag{2.17}$$

where q_i, q_j are the charges on atoms i and j, and ε_0 is the permittivity of free space. There are many forms used to describe the van der Waals energy. The two most popularly used are the Lennard-Jones (LJ) potential (Lennard-Jones, 1931),

$$U(r) = \left(\frac{A}{r^{12}}\right) - \left(\frac{B}{r^6}\right) = 4\varepsilon\left[\left(\frac{\sigma}{r}\right)^{12} - \left(\frac{\sigma}{r}\right)^6\right] \tag{2.18}$$

where $A = 4\varepsilon\sigma^{12}$ and $B = 4\varepsilon\sigma^6$ or the Buckingham potential,

$$U(r) = A'exp(-B'r) - \frac{C'}{r^6} \tag{2.19}$$

In Equation 2.18 and 2.19, A, B, ε, σ, A', B' and C' are constants fitted to *ab initio* and/or experimental data. The parameters A' and B' determine the short range repulsive interaction, C' is the dispersion parameter. The parameters ε and σ have the significance of being the depth and zero point of the potential. Both the LJ and Buckingham potential include the long-range London dispersion term.

2.7.2 Periodic Boundary Condition and Other Requirements

Since the computation time required calculating the trajectories of all N particles in a simulation box increases with N^2, the simulated system cannot be made large enough to accurately represent the bulk properties of an actual crystal or

amorphous material: surface effects would always be present. This problem is solved by implementing periodic boundary conditions, in which the simulation box is replicated through space in all directions; see Figure 2.19. The set of atom present in the box is thus surrounded by exact replicas of itself, i.e. periodic images. If an atom moves through a boundary on one side of the simulation box, so will its replica on the other side. This keeps the number of atoms in one box constant, and if the box has constant volume the simulation then preserves the density of the system, which can affect the properties of the simulation, but much less than the surface effect would have done without the periodicity. An MD simulation should also follow the laws of thermodynamics. At equilibrium, it should have a specific temperature, volume, energy, density, pressure, heat capacity, *etc*. In statistical thermodynamics, this constitutes the state of the system; its *ensemble*. Since MD is a statistical mechanic method, an evaluation of these physical quantities can be made from the velocities and masses of the particles in the system. MD can also serve as a link between these atomic-level quantities and macroscopic properties. Three different ensembles have been used here:

1) The microcanonical ensemble (NVE), which maintains the system under constant energy (E) and with constant number of particles (N) in a well-defined box with volume (V). This is appropriate during the initial equilibration phase of a simulation.

2) The isothermal-isobaric ensemble (NPT), where temperature and pressure are kept constant. This is normally the best model of the experimental conditions.

3) The canonical ensemble (NVT), where volume and temperature are kept constant. This ensemble has been used for most simulations, so that comparisons can be made with experimental data from structures with fixed dimensions.
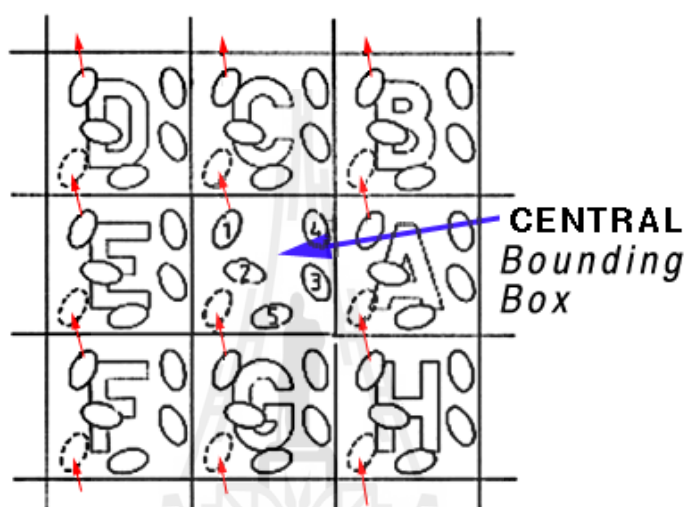
Figure 2.19 Periodic boundary conditions in molecular simulation (from http://www.sv.vt.edu/classes/MSE2094_NoteBook/MolecDyn/periodic.gif).

One factor that impacts total CPU time required by a simulation is the size of the integration time-step (Δt). This is the time length between evaluations of the potential. The time-step must be chosen small enough to avoid discretization errors (i.e. smaller than the fastest vibrational frequency in the system). Typical time-step for classical MD is in the order of 1 femtosecond (10^{-15} s). This value may be extended by using algorithms such as *SHAKE*, which fix the vibrations of the fastest atoms (e.g. hydrogens) into place. The SHAKE algorithm, a modification of the

Verlet algorithm, has become the standard approach for doing molecular dynamics with fixed bond lengths. It can also be used to hold angles fixed, but this is less common. It works well for time-step up to 5 fs, thereby enabling a five-fold speedup in computational time as long as the process of iteratively solving the constraint equations does not consume too much time (Mathiowetz, 1994).

2.7.3 Structures from MD Simulation

The trajectories given by MD simulations can be used to calculate different properties relating to structural behavior. This analysis and its chemical interpretation is the major part of this thesis work.

2.7.3.1 Radial Distribution Function

One of the most important properties extracted from MD simulation is the pair radial distribution function (RDF). It is a function, usually written as $g_{ab}(r)$, which presents the probability of finding a particle of type b at a distance r from particle of type a. In a perfect crystal without thermal motion, RDF would appear as periodically sharp peaks, which gives information about the short-range order in the system. RDF can be calculated by counting the number of atom pairs within some distance ranges, and averaging this over a number of time-steps and particle pairs:

$$g_{ab}(r) = \frac{\sum_{k=1}^{M} N_k(r_{ab}, \Delta r)}{M(\frac{1}{2}N)\rho V(r_{ab}, \Delta r)} \tag{2.20}$$

Where N_k is the number of atoms found at time k in a spherical shell of radius r and thickness Δr, and ρ is the average system density, N/V, of a given atom type.

Integrating this RDF over r gives the coordination number function (CNF), which is the average coordination number of particle type a to particle type b at distance r. RDF can be compared directly with experimental data from X-ray or neutral diffraction, and can thus be used as a check on the reliability of the potentials forcefield in many systems.

2.7.3.2 Bond Angle and Dihedral Angle

Local chain geometry is frequently characterized by measurements of valence and dihedral angle distributions. The latter, whose values are essentially determined by a combination of packing effects and local intramolecular interactions are strongly correlated with global dimensions, and are often experimentally measurable.

In a chemically complex system such as $LiPF_6$:PEO_6, the average atomic distances calculated as RDF can be too rough measurement to capture all the structural information available. The spatial arrangement of atoms can also be of major interest, and can be obtained throughout by calculating bond angle and dihedral angle distributions in the crystallographic asymmetric unit. The total distribution of all bond and dihedral angles contains all the information we need on the polymer configuration. Figure 2.20 shows the geometry of a simple chain molecule.

Plotting especially the dihedral angles in this way gives group information for the simulated system, which can be related to the crystallographically

determined space group. The appearance of new peaks indicates some new repeat unit.
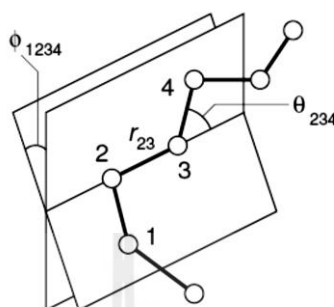
Figure 2.20 Geometry of a simple chain molecule, illustrating the definition of interatomic distance (r_{23}), bend angle (θ_{234}), and torsion angle (ϕ_{1234}) (Allen, 2004).

2.8 Molecular Dynamics Simulation Combined with EXAFS

Understanding the mechanism of gel at an atomic level is important for controlling physical properties that required for applications. Structural details of ordered domains of gelling-networks were obtained from solid state X-ray diffraction studies and circular dichroism of solutions and films. Molecular modeling of ion–polymer interaction is important to understand the chemical and physical properties of hydrogel induced by multivalent cation.

It would be of great interest to study the solvation structure of multivalent cation in polymer matrix. Calcium ion is divalent cation that is essential for the biological activity of polyelectrolytes (Kan *et al.*, 1993). The biological activity of such polyelectrolytes is affected by a binding of metal ions, and depends on ion

hydration (Manning, 1979). The problem of the Ca^{2+} hydration structure is made difficult by the weak and asymmetric nature of the Ca–O inter-action (Ohtaki and Radnai, 1993). Several structural studies have been performed by using a variety of experimental and theoretical techniques including wide-angle X-ray scattering (WAXS) (Licheri, Picacaluga, and Pinna, 1976; Yamaguchi, Hayashi, and Ohtaki, 1989), neutron diffraction isotope substitution (NDIS) (Hewish, Neilson, and Enderby, 1982) and X-ray absorption fine structure (XAFS) (Spångberg *et al.*, 2000; Jalilehvand *et al.*, 2001). In diluted aqueous solutions, the first coordination shell of calcium ion contains at least 6 water neighbors up to 12 (Probst, Radnai, Heinzinger, Bopp, and Rode, 1985; Smirnov, Yamagami, Wakita, and Yamaguchi, 1997; Chialvo and Simonson, 2003; Fulton, Heald, Badyal, and Simonson, 2003). The number of molecules coordinated by this ion depends on the salt concentration (Zavitsas, 2005).

Structural parameters can be calculated from theoretical techniques including ab initio electronic structure calculation or numerical simulations such as Molecular Dynamics (MD) simulation (Owczarek and Hawlicka, 2006; Owczarek, Rybicki, and Hawlicka, 2007). MD simulation techniques provide a powerful approach to probing such processes in condensed phase environments and provide a detailed picture of structure and dynamics for complex systems that may not be tractable by other methods (Allen and Tildeslet, 1987). Due to the advance of modern extended X-ray absorption fine structure (EXAFS) algorithms and the availability of more accurate ion and solvent potential models, the number of studies that combine MD simulation with EXAFS has increased considerably (D'Angelo, Di Nola, Filipponi, Pavel, and Roccatano, 1994; Filipponi and Di Cicco, 1995; Di Cicco, Minicucci, and Filipponi, 1997; Roccatano, Berendsen, and D'Angelo, 1998; Hoffmann, Darab, Palmer, and

Fulton, 1999; Witkowska, Rybicki, Panfilis, and Cicco, 2006; Anspoks and Kuzmin, 2011). The accuracy of existing theoretical models for inter-atomic potential in solid and liquid simple ionic systems was discussed through direct comparison of EXAFS and MD simulation results (D'Angelo, Petit, and Pavel, 2004; Dang, Schenter, Glezakou, and Fulton, 2006). Molecular dynamics (MD) simulation technique provides a powerful approach to probe such processes in condensed phase environments.

In this research, MD simulations of calcium ion in solvent, alginate, pectin, poly(vinyl alcohol) and poly(acrylic acid) have been performed to obtain structural details. Theoretical EXAFS spectra were also computed. The simulated MD-EXAFS spectra were directly compared with the EXAFS experimental result.

2.9 Monte Carlo Simulation

Monte Carlo (MC) Simulation is the application of MC methods to molecular problems. MC methods are utilized as computational tools in many areas of chemical physics. MC simulation attempt to follow the "time dependence" of a model for which change, or growth, does not proceed in some rigorously predefined fashion (e.g. according to Newton's equations of motion) but rather in a stochastic manner which depends on a sequence of random numbers which is generated during the simulation. MC simulation can find a conformational state in a stochastic way by generating random numbers. With a given potential like Equation (2.21), the simulation involves a successive energy evaluation to make a decision for acceptance of a move attempt which is chosen randomly.

$$V_{total} = \underbrace{V(r)_{bond} + V(\theta)_{angle} + V(\phi)_{torsion} + V(\chi)_{out\text{-}of\text{-}plane}}_{V_{bonded}} + \underbrace{V(r)_{vdw} + V(r)_{elec}}_{V_{non\text{-}bonded}} \quad (2.21)$$

Monte Carlo simulation uses random numbers for making decision during the simulation. The decision is accomplished by Metropolis algorithm (Metropolis, Rosenbluth, Rosenbluth, Teller, and Teller, 1953) in the most cases, which has the following criteria. (1) Start the walker at a random position r. (2) Make a trial move to a new position r'. (3) Accept the trial move to r' with probability (Equation (2.22)).

$$\begin{aligned} \Delta E \leq 0 & \qquad\qquad accepted \\[2mm] \Delta E > 0 \quad AND \; \exp\left(-\frac{\Delta E}{kT}\right) \geq rand(0,1) & \quad accepted \\[2mm] \Delta E > 0 \quad AND \; \exp\left(-\frac{\Delta E}{kT}\right) < rand(0,1) & \quad rejected \end{aligned} \qquad (2.22)$$

where

$$\Delta E = V(r') - V(r) \qquad (2.23)$$

If the new state is in a lower energy state, the new state replaces the previous state. If the new state is in a higher energy state, the decision is based on the energy difference between two states. For the decision procedure, MC simulation allows a system to move to higher energy state. The probability to overcome the higher energy barrier depends on the energy difference between the new attempt and the current conformation. By doing so, MC simulation explores the conformational space to calculate the ensemble averaged properties, while MD simulation deals with time

averaged properties. Both averaged properties should be same through the ergodic hypothesis.

Much effort has drawn attention to increasing the computational efficiency of MC simulation. One of the efforts is to run the simulation on a lattice, which reduces the floating number calculation. Another way to gain speed in the MC simulation is to use an efficient move algorithm that allows the faster relaxation or equilibration. Many beads can move at a single move attempt. The computational time of the lattice simulation based on MC method is proportional to the power of 1 to 2 depending on the quality of the potential energy function.

2.10 Monte Carlo Simulation and Topological Network Polymer

The network-like structure can be form by threading of linear chains through cyclic molecule. These structures are predicted to have interesting properties that differ from the properties of the initial starting materials.

The interest of cyclic polymers first developed when it was discovered in natural biological systems. In 1958, Jacob and Wollman reported that the genetic map of bacterial chromosomes has circularity, which was later confirmed by electron microscopy (Freifelder *et al*., 1964). In an effort to better understand these natural macrocycles and to emulate their unusual properties, chemists and polymer scientists have synthesized cyclic polymers. The first synthetic cyclic poly(dimethylsiloxane) was made in 1977 (Dodgson and Semlyen, 1977). Very shortly after the first reports on the synthesis of polymer cyclic, their melt dynamics in blends with linear polymers were characterized.

The solution-blended 16 kg/mol fluorescently labeled cyclic polystyrene (PS) with unlabeled linear PS (110 kg/mol) and used a holographic technique to study the selfdiffusion of cyclic in the melt (Antonietti, Coutandin, Gruetter, and Sillescu, 1984). When the binary blend sample was isolated by precipitation from solution, a self-diffusion coefficient (D) of 10^{-11} cm^2/s was measured. However, when the blend sample was prepared by slow evaporation of the solvent, no diffusion of the cyclic was observed, giving rise to an estimated $D < 10^{-14}$ cm^2/s. This lack of mobility was attributed to threading of the cyclic by chains during sample preparation as the solution concentration slowly increased.

The effect on the melt viscosity of linear polybutadiene (PB) upon adding cyclic PB has been examined (Roovers, 1988). The data revealed that the blend viscosity increased above that expected from the weighted average of the two pure components. When cyclic PB (40 kg/mol) was mixed with 20-25% linear PB, the blend viscosity was 10 times greater than that of the pure cyclic. The rapid increase in viscosity was attributed to the "increased number of entanglements per chain". Semlyen et al. prepared cyclic poly(dimethylsiloxane)s (PDMS) and examined the melt viscosities and self-diffusion coefficients for 50:50 blends of equivalent-molecular-weight cyclic and linear PDMS (Orrah, Semlyen, and Ross-Murphy, 1988; Cosgrove *et al.*, 1996). They covered the molecular-weight (MW) range from 0.3 to 30 kg/mol and found that the viscosities of the blends were lower than expected for the samples with less than 100 backbone bonds and higher than expected for the higher-MW samples.

Topological effects are also apparent in the self-diffusion behavior of cyclic and linear DNA. In 2007, Robertson and Smith used fluorescent microscopy to track the motion of labeled cyclic or linear DNA in solutions of chains or rings as a function of

molecular length and concentration. They refer to their four topologically distinct samples as linear tracers in chains (L-L), linear tracers in rings (L-C), cyclic tracers in chains (C-L), and cyclic tracers in rings (C-C) and find that $D_{C\text{-}C} > D_{L\text{-}C} > D_{L\text{-}L} > D_{C\text{-}L}$ at 1 mg/mL. They also report that $D_{C\text{-}L}$, in contrast to the D for the other three topological mixtures, decreases too steeply with increasing concentration to be described by reptation alone: "a process much slower than reptation governs that case" (Robertson and Smith, 2007).

The most experimental data on cyclic polymers are, in fact, data on cyclic-linear blends, due to contamination or limitations of purification methods. Important insights into the structure of cyclic/linear melts have been provided by modeling studies. Cyclic polymers are collapsed in their melts compared to linear polymers of the same lengths (Pakula and Geyler, 1988). The size and conformations of crown ethers as a function of solvent polarity were investigated using Monte Carlo (MC) simulations. In 1996, Müller, Wittmer, and Cates performed bulk simulations of cyclic alkane for degree of polymerization, N, of 16 -512, using the bond fluctuation method (BFM). The size of the cyclic molecules was found to be smaller than that of linear chains at the same degree of polymerization. The dynamics of cyclic chain was found to be similar to the dynamics of the linear chains, although Muller *et al.* did not observe any entanglement effects over the molecular weight range that was studied.

The idea is to use Monte Carlo simulations to study the statics and dynamics properties of pure linear, pure cyclic polymers and their blends in the melt state. The Monte Carlo (MC) simulation method was used to study the structure of cyclic/linear polymer. Poly(ethylene oxide) PEO was chosen as the subject of these study for variety of reason. (1) Linear POE has low entanglement molecular weight (Me $\sim$ 2

kg/mol) and critical molecular weight for entanglement (Mc ~ 5.87 kg/mol), which means that unentangled and entangled regimes can be studied without simulated high-MW molecules with large box size that cause time consuming. (2) PEO structure is not too complicated for mapping in to coarse-grained beads and (3) the melt dynamics of cyclic POE or its blends with linear had not yet been reported.

CHAPTER III

MOLECULAR DYNAMICS SIMULATION STUDY AND EXAFS MEASUREMENT OF CALCIUM ION IN WATER, ETHANOL, ISOPROPANAOL, POLY(VINYL ALCOHOL), POLY(ACRYLIC ACID), PECTIN AND ALGINATE

3.1 Abstract

Molecular Dynamics (MD) simulation and the extended X-ray absorption fine structure (EXAFS) spectroscopy were employed to obtain the atomistic solvation structure of calcium ion (Ca^{2+}) in water, ethanol, isopropanol poly(vinyl alcohol) (PVA), Poly(acylic acid) (PAA), pectin (polygalacturonate), and alginate (polyguluronate). From MD simulation results of the calcium Ca^{2+} in water, ethanol, isopropanol poly(vinyl alcohol)(PVA), and poly(acylic acid)(PAA), it is obvious that there is only one dominant shell from oxygen atoms around calcium ion. There is no evidence for the formation of significant numbers of Ca^{2+}–Cl^- contact ion pairs under the condition of this study. For calcium ion in pectin and alginate, the interaction between the carboxylate groups (O1-) and Ca^{2+} could be stronger than that between the hydroxyl (O2h) or ether (O2e) groups and the Ca^{2+}. Ca^{2+} ions were trapped within the chelation structure between polyuronate (pectin and alginate) that corresponded to

a stable Ca^{2+}/polyuronate complex formation. The MD and EXAFS technique is a powerful method to elucidate the detailed solvation structure of the probed ion in polymer matrix at the atomistic scale.

3.2 Introduction

Calcium ion plays a key role in many biological processes, and its biochemical activity probably depends on ion hydration. In diluted aqueous solutions, the first coordination shell of Ca^{2+} contains at least eight water neighbors, but higher value (about 12) has also been deduced from freezing point depression. Unlike other divalent ions, the hydration shell of Ca^{2+} does not show a regular symmetry, either tetrahedral or octahedral and the number of molecules coordinated by this ion depends on the salt concentration and temperature. The structure of its primary hydration shell has been investigated by diffraction techniques, MD simulation and ab initio calculation. The determination of solvation structure around the metal ion in solution is generally difficult task. EXAFS was widely used experimental methods. The EXAFS signal is a modulation of the X-ray absorption coefficient on the high energy side of an elemental absorption edge, and it contains information on the coordination shells surrounding that atom. The type and number of atoms in a shell, as well as the distance to and disorder within a shell, are all reflected in the EXAFS data.

EXAFS is the measure of oscillations in the absorption coefficient (μ) about its mean value at energies between 50 and 1000 eV above an atomic absorption edge. An absorption edge occurs when the energy of an X-ray is sufficient to cause the ejection of a photoelectron; the K-edge corresponds to the ejection of a 1s electron. Oscillations occur because the outgoing photoelectron wave can be backscattered by

neighboring atoms which leads to interference between the outgoing and backscattered waves. Qualitatively, the shape and period of the oscillations will be a function of the absorbing atom as well as the type, distance, and number of atoms around the absorbing atom. Generally, the distance between the central atom and the backscattering atom must be less than 6 Å in order for the interference to be significant.

The molecular modeling of ion–polymer interaction is important to understanding the chemical and physical properties of hydrogel that is induced by multivalent cation. MD simulations provide a detailed picture of structure and dynamics for complex systems that may not be tractable by other methods. Structural parameters are calculated from experimental measurements, ab initio electronic structure calculations or numerical simulations such as MD. Figure 3.1 gives a qualitative picture of these structural parameters, the coordination number of the nearest neighbors, N; Debye–Waller factor, σ^2, which corresponds to half-width of the peak in radial distribution function, $g_{ab}(r)$; and the average distance between the central absorbing atom (a) and surrounding atoms (b), which corresponds to the center of peak, R_0. The broken line depicts the (ideal) Gaussian peak centered at R_0, G, which in general, can be more symmetric and narrower than the real peak. This center is shifted compared to the one obtained experimentally, or even from the MD simulations. The coordination number (CN) can be calculated by direct integration of this first peak:

$$CN = 4\pi\rho \int\limits_{r1}^{r2} g_{ab}(r)r^2dr \qquad (3.1)$$

where $r1$ and $r2$ are the integration limits.
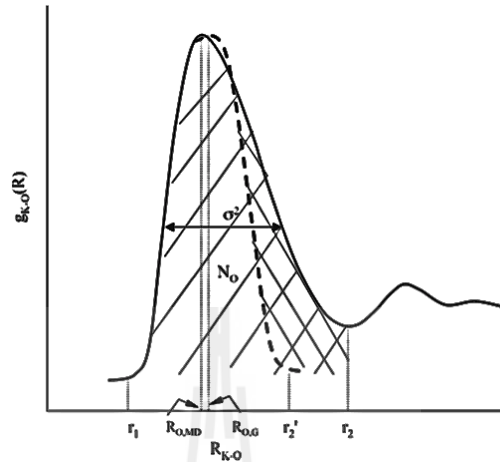
Figure 3.1 The fundamental quantities of ion solvation structure, coordination
number N_0 (area under curve), Debye–Waller factor σ^2, center of peak
R_0 (Glezakou, Chen, Fulton, Schenter, and Dang, 2006).

In EXAFS, an X-ray source is tuned to energies just slightly above an inner-
shell electron absorption edge. As a result, a low-energy electron is ejected and is
backscattered by atoms of the nearest solvent shells. This scattering process leads to
interferences with the outgoing wave, giving rise to the characteristic oscillations of
the EXAFS spectra. An analysis of the relation between EXAFS spectra and
molecular structure has benefited from the availability of efficient algorithms for the
evaluation of electron scattering analysis such as those implemented in the FEFF6
code. In standard EXAFS analysis, the fine structure factor is defined by

$$\chi(E) = \frac{\mu(E) - \mu_0(E)}{\Delta\mu_0(E_0)} \tag{3.2}$$

where $\mu(E)$ is the absorption coefficient as a function of the X-ray energy E, $\mu_0(E)$ is the background absorption coefficient, and $\Delta\mu_0(E_0)$ is the jump in the absorption background at the absorption edge, (E_0). Given a set of neighboring atoms located at positions r_i relative to the photoelectron source located at r_0, with $R_i = |r_i - r_0|$, the EXAFS signal in k-space is described by:

$$\chi(k) = \sum_i N_i \frac{F_i(k)}{kR_i^2} e^{-2\sigma_i^2 k^2} e^{-2R_i/\lambda} \sin[2kR_i + \varphi_i(k)] \tag{3.3}$$

where the photoelectron wave-vector, k, is related to the X-ray energy by $E = E_0 + (\hbar^2 k^2)$. N_i is the number of neighboring atoms in the ith coordination away from the absorbing atom. The backscattering amplitude and mean-squared displacement of the neighboring atoms are given by $F_i(k)$ and σ_i, respectively. The phase shift of the photoelectron is given by $\varphi_i(k)$, while the exponential term containing the mean free path λ of the photoelectron accounts for their inelastic scattering. It is this exponential damping term which accounts for the selectivity of EXAFS to short-ranged order. The backscattering amplitude and the phase shift functions are extracted from EXAFS spectra taken from a standard which has a known structure and which contains the same absorbing and scattering elements as the unknown. A Fourier transform of the oscillations in k-space yields a real-space distribution, similar to a radial distribution function. Fitting Equation (3.3) to the measured EXAFS spectra can provide the structural parameters: the number and type of surrounding atoms, their average distance to the central absorbing atom, and their distribution about the absorbing center.

In this research, MD simulations of calcium ion in water, ethanol, isopropanol, PVA, PAA, Pectin and Alginate have been performed to obtain structural solvation details. Theoretical EXAFS spectra were also computed. The simulated EXAFS spectra were directly compared with the experimental.

3.3 Calcium Ion in Water, Ethanol and Isopropanol

3.3.1 EXAFS Experimental Details

Anhydrous calcium chloride ($CaCl_2$ 99.99%, Aldrich), anhydrous ethanol (99.5%, Aldrich), anhydrous isopropanol (99.5%, Aldrich) and distilled, deionized water were used. In preparation of $CaCl_2$ aqueous solution for EXAFS measurement, Dang *et al.*, 2006 showed that for 6.0 m $CaCl_2$ in water (Ca^{2+}:O ratio ≈ 1:9), there are virtually no contact ion pairs. Thus, the dilute solution of Ca^{2+}:O ratio = 1:128 for $CaCl_2$/ethanol and $CaCl_2$/isopropanol system were selected to study, to avoid the formation of $Ca^{2+} - Cl^{-}$ contact ion pairs.

EXAFS spectra were obtained on the beam – line 8 (BL-8) at Synchrotron Light Research Institute (public organization) (SLRI), Nakhon Ratchasima, Thailand. The storage ring operated at the energy 1.2 GeV and average current 100 mA, data were collected at the exit of a double – crystal Si(111) monochromator. The spectra were recorded in transmission mode detector by two ionization chamber filled with nitrogen gas, gas pressure was approximately 160 and 872 mbars in the first and seconded chambers, respectively. The energy calibration was obtained by mean of $CaCO_3$ by setting the Calcium K - edge absorption at 4038.5 eV. Scan ranges of all measurements were set to 3938.5 - 4838.5 eV, energy step of 2 eV were used both in the pre – edge and in the EXAFS region, whilst 0.5 eV step were used in the edge

region with time step of 1 second. A total of 5 scans (1 scan ≈ 25 minute) were collected to improve the signal to noise ratio. And then data processing was done using Athena (ifeffit) (Newville, 2001) software and then experimental data were fitted with CaO standard using FEFF code (Zabinsky, Rehr, Ankudinov, Albers, and Eller, 1995) and experimental data were compared to those from simulation.

3.3.2 Computational Details

Molecular dynamics simulation was carried out using Materials Studio 4.2 simulations package provided by National Nanotechnology Center, Thailand. The COMPASS forcefiled (Sun, 1998) was employed for all simulation system. The pure solvent and their mixture with salt were built in the cubic unit cells under periodic boundary conditions using Amorphous Cell module. For Ca^{2+}/Solvent system consisting of solvent molecules, Ca^{2+} and Cl^- ion situated in a simulation box with Ca^{2+}:O ratio = 1:128 in equivalent with EXAFS experiment. Density of the mixture system was calculated from the density of individual component and volume fraction of each component. The densities of pure solvent taken from the literature were: density of water = 0.997 g/cm^3, density of ethanol = 0.785 g/cm^3, density of isopropanol = 0.781 g/cm^3. Then, simulation systems were allowed to vary its volume by performing the NPT ensemble (number of molecules, pressure and temperature are constant) run at 298 K and 1.0 atm to obtain an equilibrium density. The amorphous cell was energy-minimized using the Smart minimization method with a convergence level of 0.01 kcal/mol/Å. The Smart minimizer starts with the Steepest Descent method, followed by the Conjugate Gradient method and ends with a Newton method. After that, short NVT (constant Number of molecules, volume and Temperature)

simulations were run for 0.2 ns at 298 K to relax the structures. Then another 1 ns dynamics with a time step of 1 fs at 298 K was performed in the NVT ensemble for data analysis. In all simulation, the trajectories were recored every 5000 fs for subsequent analysis.

All simulation systems were computed for the pair correlation function (g(r)) (or radial distribution function, RDF) to obtain the distance and the coordination number. Furthermore, 100 configurations taken from each simulation were used to generate EXAFS spectra and then the averaged spectrum was directly compared with experimental data. For each configuration taken from the trajectory, a cluster was obtained by extracting all species that fell within 6 Å radius of the probed ion. The cluster was then used as an input to the program FEFF, which calculates the EXAFS spectrum $\mu(E)$ for the probed ion as a function of energy, E, using a multiple scattering approach.

In the MD-EXAFS procedure, the average EXAFS spectrum from the simulation was obtained from a configurationally average as:

$$\bar{\chi}(E) = \frac{\bar{\mu}(E) - \mu_0(E)}{\Delta\mu_0(E_0)} \tag{3.4}$$

where $\bar{\mu}(E)$ is the absorption coefficient as a function of the X-ray energy E (bars denote the configurationally average), $\mu_0(E)$ is the background absorption coefficient, and $\Delta\mu_0(E_0)$ is the jump in the absorption background at the absorption edge (E_0). EXAFS oscillation $\chi(k)$ is expressed by:

$$\bar{\chi}(k) = \sum_{i} N_i S_0^2 \frac{\bar{F}_i(k)}{k\bar{R}_i^2} e^{(-2\sigma_i^2 k^2)} e^{(-2R_i/k)} \times \sin\left[2k\bar{R}_i + \bar{\varphi}_i(k) - \frac{4}{3}C_{3,i}k^3\right] \quad (3.5)$$

where k is the photoelectron wave vector, $k = \sqrt{2m(hv - E_0)}/\hbar$. N_i is the number of the neighboring atoms in the ith coordination shell at a distance R_i away from the absorbing atom. $F_i(k)$ is the back scattering amplitude. σ_i^2 is Debye Waller factor, which is related to the mean-squared displacement of R_i parameter. $\bar{\varphi}_i(k)$ is the phase shift of the photoelectron, while the exponential term containing the mean free path λ of the photo electron account for their inelastic scattering. $C_{3,i}$ reflects the structural disorder of the system. S_0^2 is the amplitude reduction factor, accounts for many body effects in a single particle theory. In order to obtain a real-space representation of the EXAFS spectra, a Fourier transform of the structure factor is calculated as implemented in the FEFFIT package. Thus equation 3.5 is transformed to:

$$\bar{\chi}(R) = \frac{1}{\sqrt{2\pi}} \int_0^\infty k^2 \bar{\chi}(k) W(k) e^{i2kR} dk \quad (3.6)$$

where $W(k)$ is a Hanning window. Some configurations taken from each simulation were used to generate EXAFS spectra and then the averaged spectrum was compared with experimental data.

Table 3.1   Charge parameters used in the simulation.

Molecule	Atom	Description	Charge
Water	H	Water hydrogen	0.410
	O	Water oxygen	-0.820
Ethanol	H	Hydroxyl hydrogen	0.410
and	O	Hydroxyl oxygen	-0.570
Isopropanol	C	Methyl carbon	-0.159
	C	Hydroxyl carbon (of ethanol)	0.054
	C	Hydroxyl carbon (of iso-propanol)	0.107
	H	Alkane hydrogen	0.053
Ca^{2+}	Ca^{2+}	Calcium ion	2.000
Cl-	Cl-	Chloride ion	-1.000

3.3.3   Results and Discussions

3.3.3.1   Radial Distribution Functions (RDF)

RDF: Calcium ion/Water, The results of RDF are shown in Figures 3.2, to compare the coordination of Ca^{2+} by all other species in the Ca^{2+}:O = 1:128 system. The characteristic parameters, peak position and coordination number (CN) are summarized in Table 3.2. The RDF of calcium ion and oxygen atoms, $g_{Ca-O}(r)$ for water, exhibits the first maximum at 2.36 Å. Integrating the Ca^{2+}–O RDFs over the first coordination shells gives an average of 7.3 oxygen atoms coordinated to each Ca^{2+}. The RDF of calcium ion and hydrogen atoms, $g_{Ca-H}(r)$ for water, exhibits the first maximum at 3.06 Å. Integrating the Ca^{2+}–O RDFs over the first coordination

shells gives average 14.8 hydrogen atoms coordinated to each Ca^{2+}. For calcium ion and chloride anion, $g_{Ca-Cl}(r)$ for water, exhibits a broad curve starting from 5.9 Å. This result indicates that the first coordination shell of Ca^{2+} (distance $\leq$ 2.75 Å) in water including of oxygen without chloride ion under the condition of this study.
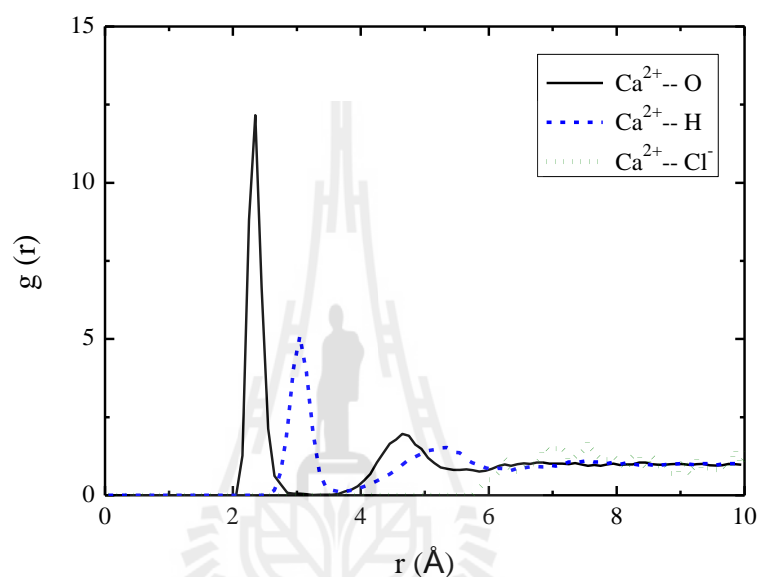
Figure 3.2 Radial distribution functions of Ca^{2+}/H_2O.

Table 3.2 Parameter characterizing the first peak of RDF determined from MD at 298 K for Ca^{2+}/H_2O (Ca^{2+}:O = 1:128) system.

ion	site	R_0 (Å), MD[a]	R_0 (Å), Ref[b].	CN, MD[a]	CN, Ref[b].
Ca^{2+}	O	2.36	2.42	7.3	8.1
	H	3.06	3.10	14.8	17

[a]this work. [b]EXAFS (D'Angelo, Petit, and Pavel, 2004) for Ca^{2+}−water.

RDF: Calcium ion/Ethanol, Figure 3.3 displays the atom labeling of ethanol molecule. The results of RDF are shown in Figures 3.4, to compare the coordination of Ca^{2+} by all other species in the Ca^{2+}:O = 1:128 system. For clarification, the Ca^{2+}– O, Ca^{2+}– C1, Ca^{2+}– C2, Ca^{2+}–Ho, Ca^{2+}–Hc, and Ca^{2+}–Cl$^-$ RDFs were calculated and plotted separately as seen in Figure 3.5, to examine how Ca^{2+} cations are coordinated by ethanol molecules and chloride anions. The characteristic parameters, peak position and coordination number (CN) are summarized in Table 3.3. The RDF of calcium ion and oxygen atoms, $g_{Ca-O}(r)$ for ethanol, exhibits the first maximum at 2.31 Å. Integrating the Ca^{2+}–O RDFs over the first coordination shells gives an average of 6.7 oxygen atoms to coordinated to each Ca^{2+} ion. For calcium ion and chloride anion, $g_{Ca-Cl}(r)$ for ethanol exhibits a signal starting from 7 Å. This result indicates that the first coordination shell of Ca^{2+} (at distance $\leq$ 2.75 Å) in ethanol including of oxygen without chloride ion, again indicating that the Cl$^-$ ion is not forming the ion pair with Ca^{2+} under the condition of this study.
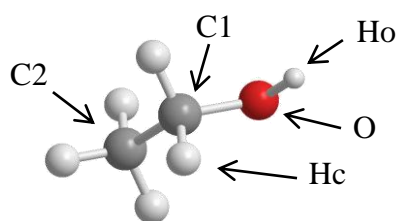
Figure 3.3   Atom labeling of ethanol.
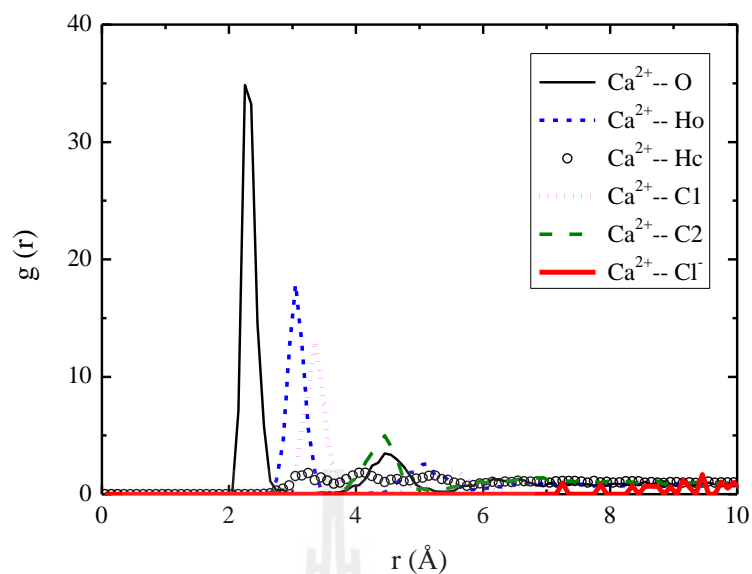
Figure 3.4 Radial distribution functions of Ca^{2+}/Ethanol (Ca^{2+}:O = 1:128).
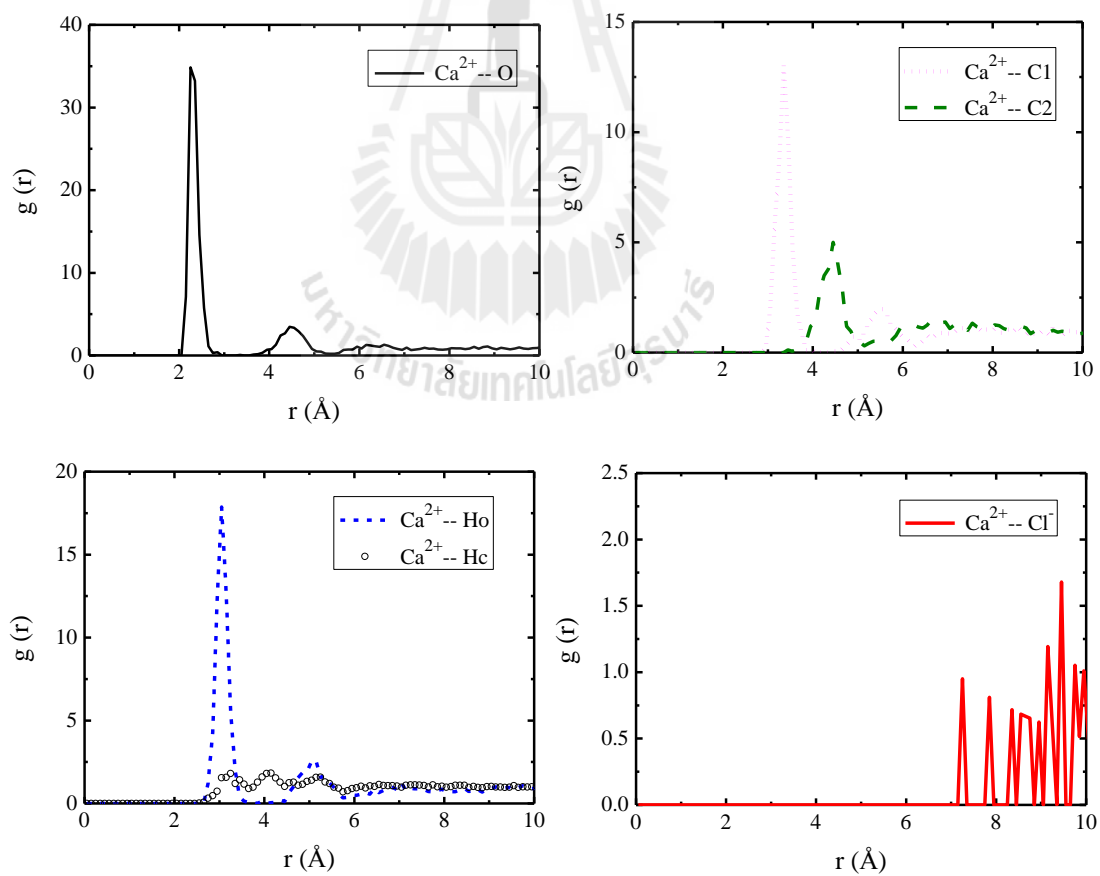
Figure 3.5 Radial distribution functions of Ca^{2+}/Ethanol (Ca^{2+}:O = 1:128), plotted

separately.

Table 3.3   Parameter characterizing the first peak of RDF determined from MD at 298 K for Ca^{2+}/Ethanol (Ca^{2+}:O = 1:128) system.

Atom Pair	R_0 (Å)	CN	Limit of integration
Ca^{2+}- O	2.31	6.7	$0 \leq R \leq 2.75$
Ca^{2+}- C_1	3.35	6.7	$0 \leq R \leq 3.85$
Ca^{2+}- C_2	4.41	7.2	$0 \leq R \leq 5.15$
Ca^{2+}- Ho	3.06	6.7	$0 \leq R \leq 3.55$
Ca^{2+}- Hc	3.28	7.2	$0 \leq R \leq 3.65$

RDF: Calcium ion/Isopropanol, Figure 3.6 displays the atom labeling of isopropanol molecule. The results of RDF are shown in Figures 3.7, to compare the coordination of Ca^{2+} by all other species in the Ca^{2+}:O = 1:128 system. For clarification, the Ca^{2+}–O, Ca^{2+}–C1, Ca^{2+}–C2, Ca^{2+}–Ho, Ca^{2+}–Hc, and Ca^{2+}–Cl^- RDFs were calculated and plotted separately as seen in Figure 3.8, to examine how Ca^{2+} are coordinated by isopropanol oxygen and chloride anions. The characteristic parameters, peak position and coordination number (CN) are summarized in Table 3.4. The RDF of calcium ion and oxygen atoms, $g_{Ca-O}(r)$ for isopropanol, exhibits the first maximum is 2.30 Å. Integrating the Ca^{2+}–O RDFs over the first coordination shells gives average 6.0 oxygen atoms coordinated to each Ca^{2+}. For calcium ion and chloride anion, $g_{Ca-Cl}(r)$ for isopropanol, exhibits a signal starting from 9 Å. This result indicates that the first coordination shell of Ca^{2+} (at distance $\leq$ 2.75 Å) in isopropanol including of oxygen without chloride ion, indicating that the Cl^- ion is not forming ion pairs with Ca^{2+} under the condition of this study.
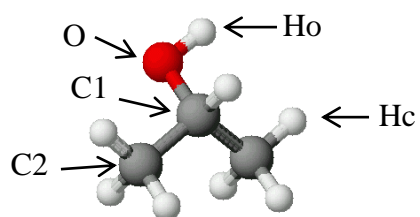
Figure 3.6   Atom labeling of isopropanol.
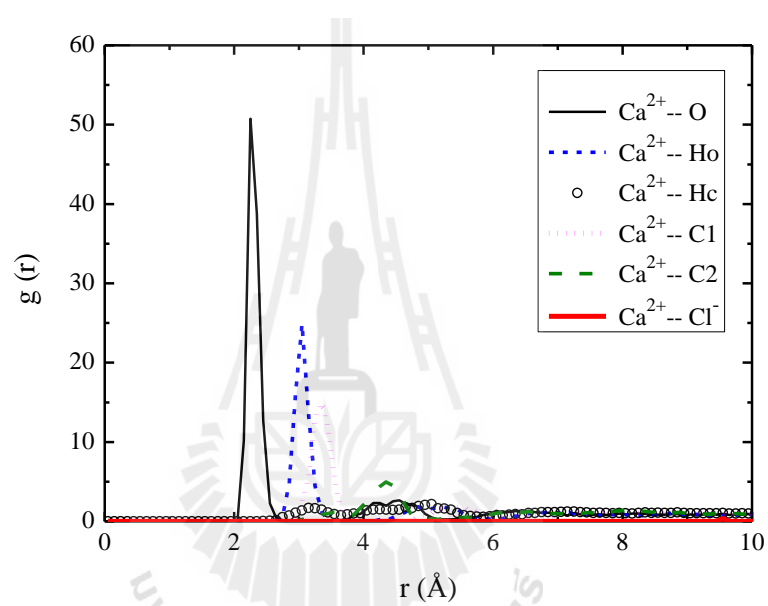
Figure 3.7   Radial distribution functions of Ca^{2+}/Isopropanol (Ca^{2+}:O = 1:128).
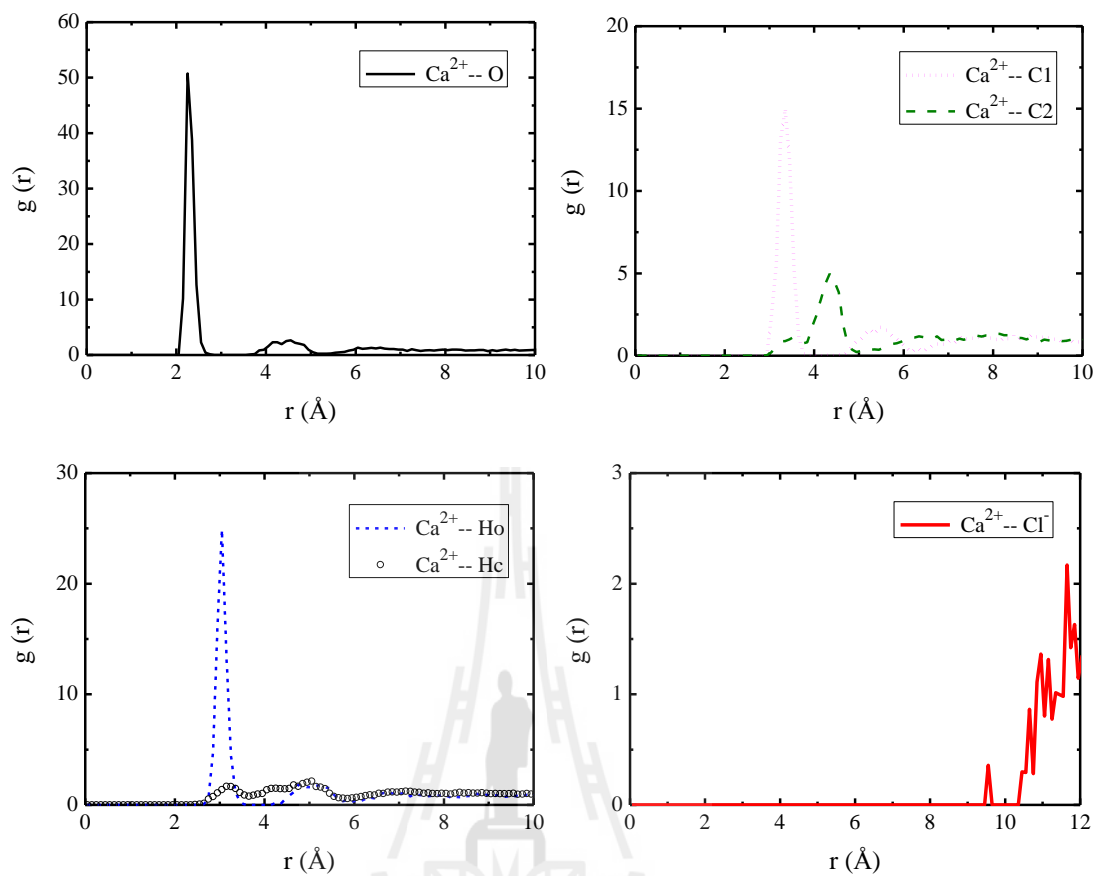
Figure 3.8 Radial distribution functions of Ca^{2+}/Isopropanol (Ca^{2+}:O = 1:128), plotted separately.

Table 3.4 Parameter characterizing the first peak of RDF determined from MD at 298 K for Ca^{2+}/Isopropanol (Ca^{2+}:O = 1:128) system.

Atom Pair	R$_0$ (Å)	CN	Limit of integration
Ca^{2+}- O	2.30	6.0	$0 \leq R \leq 2.65$
Ca^{2+}- C1	3.34	6.0	$0 \leq R \leq 3.85$
Ca^{2+}- C2	4.33	12.1	$0 \leq R \leq 4.95$
Ca^{2+} - Ho	3.04	6.0	$0 \leq R \leq 3.55$
Ca^{2+}- Hc	3.23	7.8	$0 \leq R \leq 3.65$

3.3.3.2 MD-EXAFS

MD-EXAFS: Calcium ion/Water, The comparison of k^2-weighted EXAFS spectra of CaCl$_2$/water sample having a calcium ion to hydroxyl oxygen equivalent ratio (Ca^{2+}:O) equal to 1:128 with experimental EXAFS to MD-EXAFS is shown in Figure 3.9. It is evident that the peak position is consistent between experimental and MD-EXAFS spectra. The peak in $|\chi(R)|$ is from the Ca-O scattering for the first shell oxygen from water as show in Figure 3.10. The corresponding Fourier transform (FT) in Figure 3.10 is almost featureless for distances beyond the largest peak. This shows that the single backscattering from the first hydration shell is dominating in the part of EXAFS region ($k > 2$ Å) used for the Fourier transform, and those contributions from multiple scattering within the first shell and the backscattering from the second shell with longer pathways are minor importance. The disorder in the first and second shells, which causes a considerable spread in the scattering pathways, is the reason for the lack of high R features in the Fourier transform.

Debye-Waller factors (σ^2) reflect the structural disorder of the system. We use the Gaussian distribution function (Dang, Schenter, Glezakou, and Fulton, 2006) to fit the first peak of the radial distribution function of the simulation data to obtain the Debye-Waller factors (σ_G^2), $\sigma_G^2 = 0.0088$ Å^2. For the EXAFS experiment, the Debye-Waller factors (σ_i^2) were obtained by fitting the expression given by Equation (3.5) to the measured EXAFS spectra, $\sigma_i^2 = 0.0097$ Å^2. The Debye-Waller factors determined from simulation is smaller than those determined form analysis of EXAFS measurements. Indicate that the structural disorder of experimental data is more than

those of the simulation data. In overall, MD-EXAFS signals are good agreement with experiment.

Figure 3.11 shows the representative cluster (only five clusters are exemplified) extracted from MD configuration, for the Ca^{2+}/H_2O system with a typical distance distribution and distorted coordination geometry. We found that the coordination number of oxygen atom around Ca^{2+} for the first coordination shell (within 2.75 Å) are varied from six to eight, the case of seven oxygen atoms coordinated to Ca^{2+} is the most frequently observed. The position of oxygen atoms in the solvation structure is quite asymmetric.
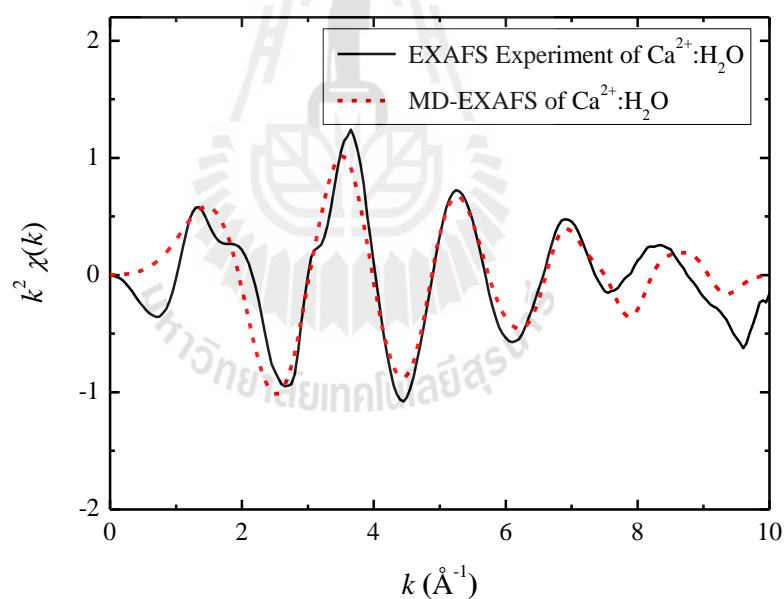
Figure 3.9 Comparison of calcium EXAFS k^2-weighted $\chi(k)$ plots for Ca^{2+}/H_2O system from experiment and MD simulation.
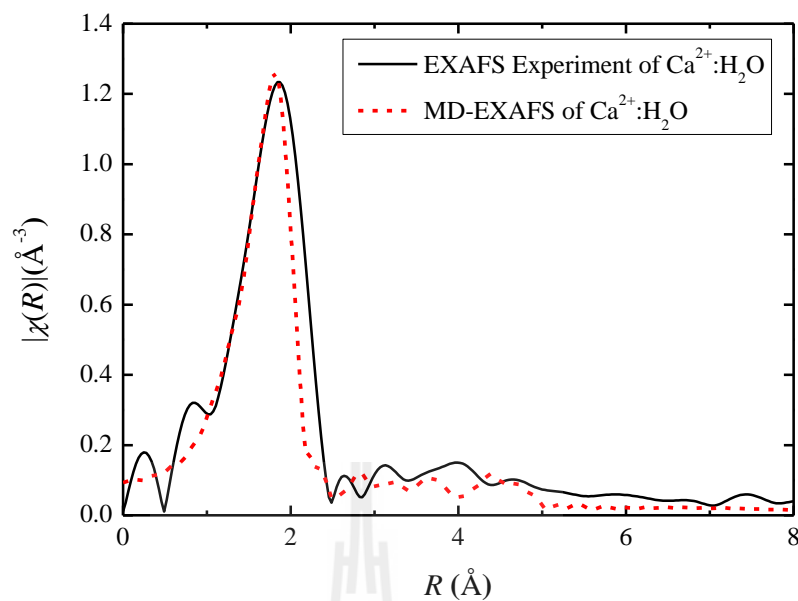
Figure 3.10 The $|\chi(R)|$ plots corresponding to the Fourier transformed $k^2\chi(k)$ as shown in Figure 3.9.
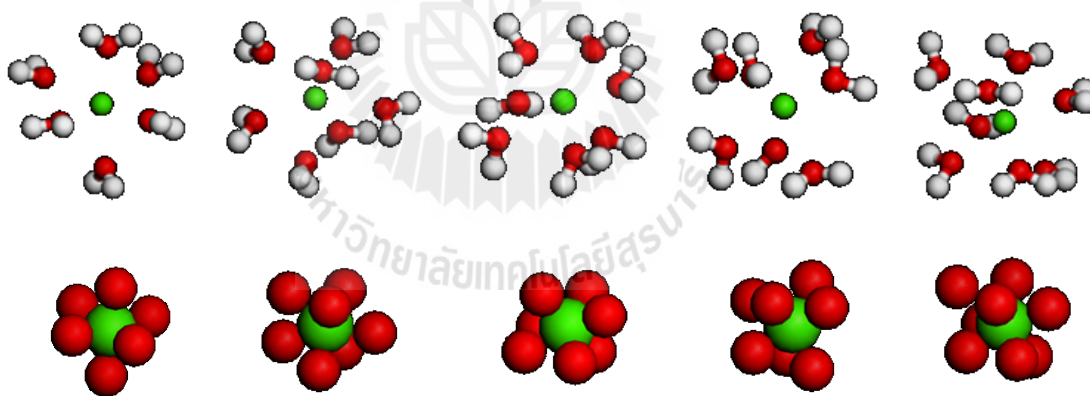
Figure 3.11 Schematics show that how Ca^{2+} ions are coordinated by H_2O. The upper figures show hydrogen atoms while the lower figures do not display hydrogen atoms. (Colors: calcium cations–green, oxygen atoms–red, and hydrogen atoms–white).

MD-EXAFS: Calcium ion/Ethanol, The comparison of k^2-weighted EXAFS spectra of CaCl$_2$/ethanol sample having a calcium ion to hydroxyl oxygen equivalent ratio (Ca^{2+}:O) equal to 1:128 with experimental EXAFS to MD-EXAFS is shown in Figure 3.12. It is evident that the peak position is consistent between experimental and MD-EXAFS spectra. The peak in $|\chi(R)|$ is from the Ca-O scattering for the first shell oxygen from ethanol as show in Figure 3.13. The corresponding Fourier transform (FT) in Figure 3.13 is almost featureless for distances beyond the largest peak. This shows that the single backscattering from the first hydration shell is dominating in the part of EXAFS region ($k > 2$ Å) used for the Fourier transform, and those contributions from multiple scattering within the first shell and the backscattering from the second shell with longer pathways are minor importance. The disorder in the first and second shells, which causes a considerable spread in the scattering pathways, is the reason for the lack of high R features in the Fourier transform. Debye-Waller factors (σ^2) reflect the structural disorder of the system. The Debye-Waller factors determined from simulation ($\sigma_G^2 = 0.0088$ Å^2) is smaller than those determined form analysis of EXAFS measurements ($\sigma_i^2 = 0.0096$ Å^2). Indicate that the structural disorder of experimental data is more than those of the simulation data. In overall, MD-EXAFS signals are good agreement with experiment.

Figure 3.14 shows the clusters (only five clusters are exemplified) extracted from MD configuration, for the Ca^{2+}/H$_2$O system with a typical distance distribution and distorted coordination geometry. We found that the coordination number of oxygen atom around Ca^{2+} for the first coordination shell (within 2.75 Å) are varied from six to eight, the case of seven oxygen atoms coordinated to Ca^{2+} is the

most frequently observed. The position of oxygen atoms in the solvation structure is quite asymmetric.
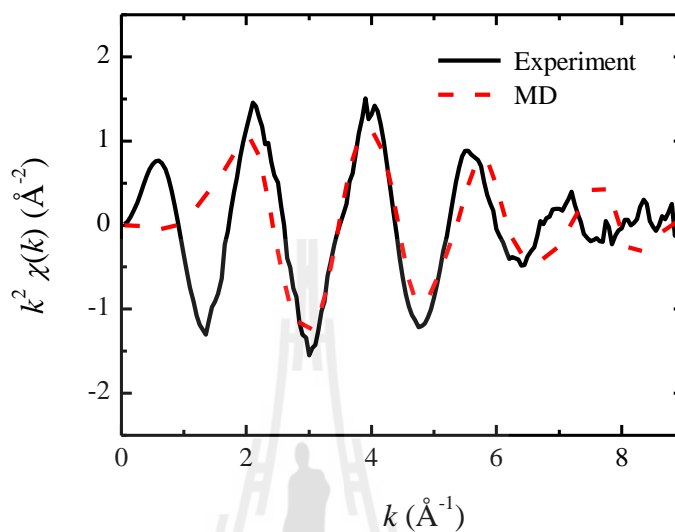
Figure 3.12 Comparison of calcium EXAFS k^2-weighted $\chi(k)$ plots for Ca^{2+}/Ethanol system from experiment and MD simulation.
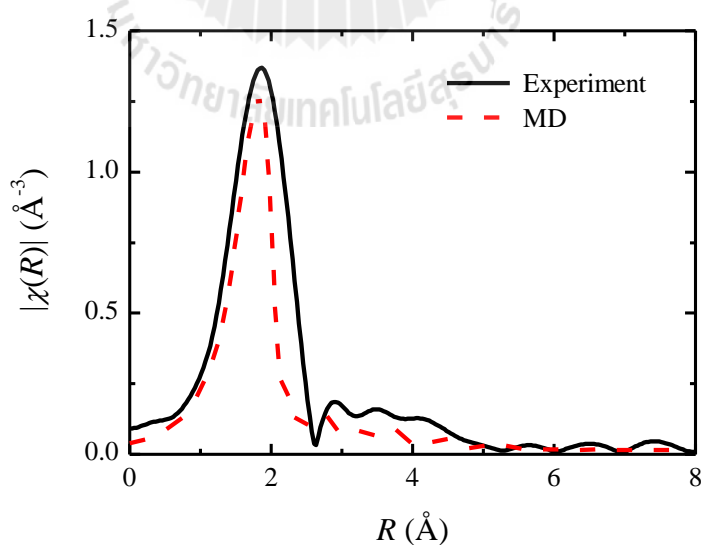
Figure 3.13 The $|\chi(R)|$ plots corresponding to the Fourier transformed $k^2\chi(k)$ as shown in Figure 3.12. The distances were not corrected for phase shifts.
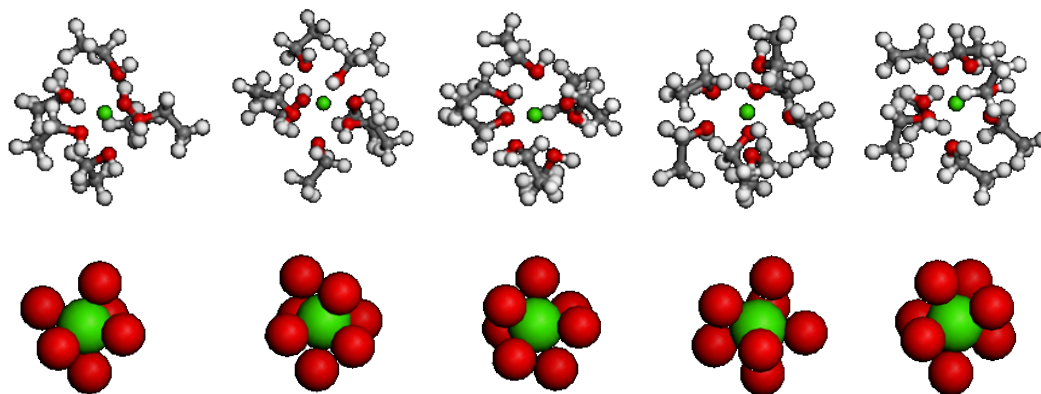
Figure 3.14 Schematics show that how Ca^{2+} ions are coordinated by Ethanol. The

upper figures show hydrogen atoms while the lower figures do not

display hydrogen atoms. (Colors: calcium cations–green, oxygen atoms–

red, carbon atom–gray, and hydrogen atoms–white).

MD-EXAFS: Calcium ion/Isopropanol, The comparison of k^2-

weighted EXAFS spectra of $CaCl_2$/water sample having a calcium to hydroxyl

oxygen equivalent ratio (Ca^{2+}:O) equal to 1:128 with experimental EXAFS to MD-

EXAFS is shown in Figure 3.15. It is evident that the peak position is consistent

between experimental and MD-EXAFS spectra. The peak in $|\chi(R)|$ is from the Ca-O

scattering for the first shell oxygen from isopropanol is shown in Figure 3.16. The

corresponding Fourier transform (FT) in Figure 3.16 is almost featureless for

distances beyond the largest peak. This shows that the single backscattering from the

first hydration shell is dominating in the part of EXAFS region ($k > 2$ Å) used for the

Fourier transform, and those contributions from multiple scattering within the first

shell and the backscattering from the second shell with longer pathways are minor

importance. The disorder in the first and second shells, which causes a considerable

spread in the scattering pathways, is the reason for the lack of high R features in the Fourier transform. The Debye-Waller factors determined from simulation ($\sigma_G^2 = 0.0060$ Å^2) is smaller than those determined form analysis of EXAFS measurements ($\sigma_i^2 = 0.0075$ Å^2). Indicate that the structural disorder of experimental data is more than those of the simulation data. In overall, MD-EXAFS signals are good agreement with experiment.

Figure 3.17 shows the clusters (only five clusters are exemplified) extracted from MD configuration, for the Ca^{2+}/isopropanol system with a typical distance distribution and distorted coordination geometry. We found that the coordination number of oxygen atom around Ca^{2+} for the first coordination shell (within 2.75 Å) are varied from six to eight, the case of seven oxygen atoms coordinated to Ca^{2+} is the most frequently observed. The position of oxygen atoms in the solvation structure is quite asymmetric.
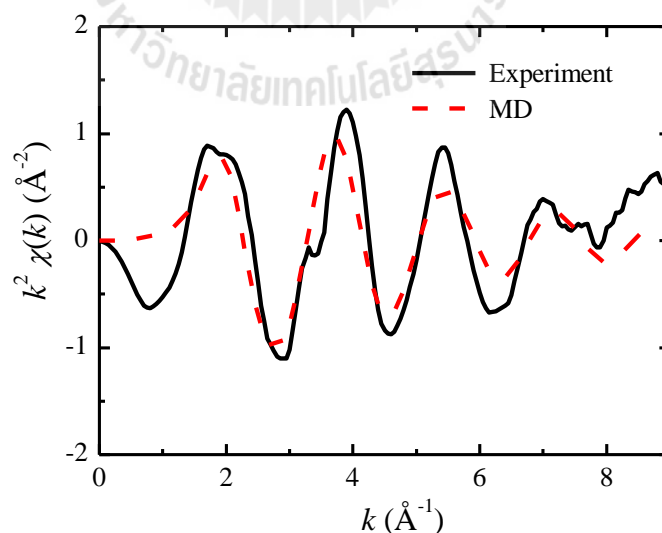
Figure 3.15 Comparison of calcium EXAFS k^2-weighted $\chi(k)$ plots for Ca^{2+}/Isopropanol system from experiment and MD simulation.
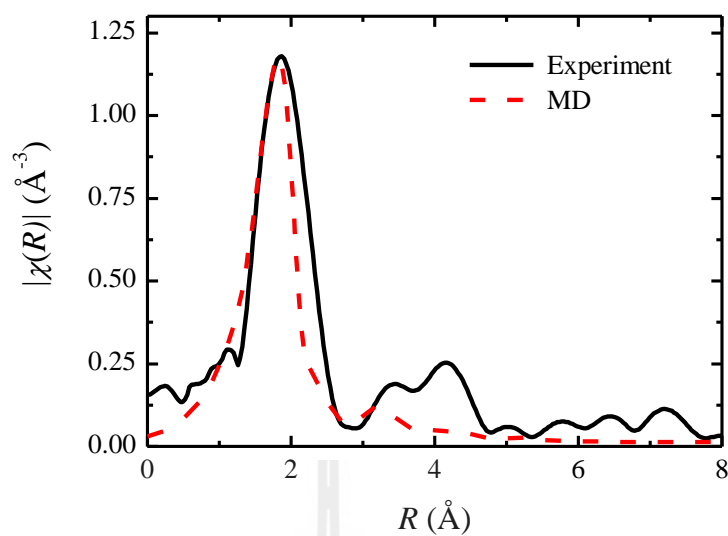
Figure 3.16 The $|\chi(R)|$ plots corresponding to the Fourier transformed $k^2\chi(k)$ as shown in Figure 3.15.
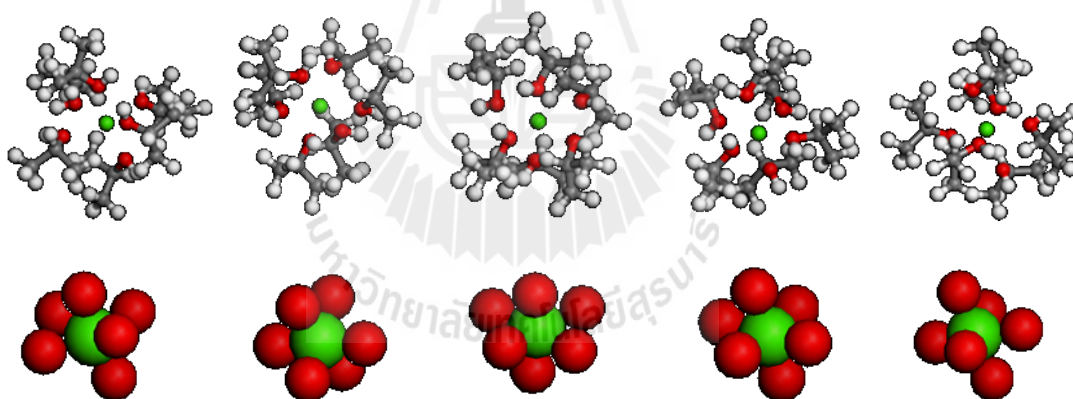
Figure 3.17 Schematics show that how Ca^{2+} ions are coordinated by Isopropanol. The upper figures show hydrogen atoms while the lower figures do not display hydrogen atoms. (Colors: calcium cations–green, oxygen atoms–red, carbon atom–gray, and hydrogen atoms–white).

3.4 Calcium ion/Poly(vinyl alcohol)

3.4.1 EXAFS Experimental Details

Anhydrous calcium chloride (CaCl$_2$ 99.99%, Aldrich) and PVA (98% hydrolyzed, Weight-average molecular weight Mw ~125,000 g/mol; manufacture's data) from Aldrich were used without further purification. Distilled, deionized water was use throughout. Since CaCl$_2$/PVA film system might be forming Ca-Cl contact ion pairs that would complicate the interpretation of the solvated Ca^{2+} ion. Thus, a series of concentration of Ca^{2+}:O ratio = 1:50, 1:25 and 1:17 for CaCl$_2$/PVA were studies. Furthermore we also examined a mixture of Ca(SCN)$_2$ in PVA with Ca^{2+}:O = 1:17. Because of its much large anion size and it is a weak ion pair former.

Sample preparation details; PVA will be dissolved in distilled, deionized water at 100°C for 3 hours to obtain homogeneous PVA solution. After the solution was cooled down to room temperature, CaCl$_2$ aqueous solution was added. PVA/CaCl$_2$ mixture solutions were stirred overnight at room temperature to achieve complete dissolution, then the solution was transferred to plastic plates and allowed to dry and solidity at an atmosphere condition in a dust free chamber and then the resulting dried films were cut to small film size 1.5 × 2.5 cm. and then dried in vacuum oven at 70°C for 24 hours to eliminate the solvent, continue drying in vacuum oven at room temperature for 6 hours, after that PVA/CaCl$_2$ films were wrapped with polypropylene film and kept in zipper plastic bag and stored in desiccators until future use. EXAFS experiment spectra, the beamline and sample handing methods for Ca^{2+} in PVA are the same with Ca^{2+} in solvent system. And then use experimental data to compare with simulation.

3.4.2 Computational Details

Molecular dynamics simulation was carried out by using Materials Studio 4.2 simulations package provided by National Nanotechnology Center, Thailand. The COMPASS forcefiled was employed for all simulation system. Bulk amorphous states for pure PVA and their mixture with salt were built using the cubic unit cells under periodic boundary conditions by using amorphous cell module. The pure PVA system consisting of 10 PVA chains with chain length 21 monomer units in a simulation box, Density of pure PVA taken from the literature (Grulke, 1999) were: density of PVA = 1.269 g/cm^3. For Ca^{2+}/PVA system consisting of 10 PVA chains with chain length 21 monomer units, Ca^{2+} ions and Cl^- ions in a simulation box with Ca^{2+}:O = 1:50 (that equivalent with experimental). Density of the mixture system was calculated from the density of individual component and volume fraction of each component. Then, simulation systems were allowed to vary its volume by performing a NPT ensemble (Number of molecules, Pressure and Temperature constant) run at 298 K and 1.0 atm to obtain an equilibrium density. The amorphous assembly was energy-minimized using the Smart minimization method with a convergence level of 0.01 kcal/mol/Å. The Smart minimizer starts with the steepest descent method, followed by the conjugate gradient method and ends with a Newton method. After that, short NVT (Number of molecules, volume and Temperature constant) simulations were run for 0.2 ns at 800 K to relax the structures. Then another 1 ns dynamics with time step 1 fs at 298 K was performed in the NVT ensemble for data analysis. In all simulation, the trajectories were saved every 5000 fs for subsequent analysis.

All simulation systems were computed for the pair correlation function (g(r)) (or radial distribution function, RDF) to obtain distance and coordination number.

Furthermore, 100 configurations taken from each simulation were used to generate EXAFS spectra and then the averaged spectrum was compared with experimental data. For each configuration taken from the trajectory, a cluster was obtained by extracting all species that fell within 6 Å radius of the probed ion. The cluster was then used as an input to the program FEFF, which calculates the EXAFS spectrum, $\mu(E)$, for the probed ion as a function of energy, E, using a multiple scattering approach.

Table 3.5   Charge parameters used in the simulation.

Molecule	Atom	Description	Charge
PVA	H	Alkane hydrogen	0.053
	H	Hydroxyl hydrogen	0.410
	C	Alkane carbon	-0.106
	C	Hydroxyl carbon	0.107
	O	Hydroxyl oxygen	-0.570
Ca^{2+}	Ca^{2+}	Calcium ion	2.000
Cl^-	Cl^-	Chlorine ion	-1.000

3.4.3   Results and Discussions

3.4.3.1   Solubility Parameter

Due to computer data storage space limitations, simulations could not be performed using the actual size of the polymers and hence, size of the polymer used in model calculations is important while computing thermodynamic quantities to understand what minimum level molecular size is sufficient to represent the real

polymer coil. To determine this minimum size, solubility parameters of PVA were computed. Hildebrand's solubility parameter (δ) represent to the strength of inter molecular interactions of pure liquid (cohesive energy density). δ is the square root of the cohesive energy density, as following:

$$\delta = \sqrt{\text{CED}} = \sqrt{\frac{\Delta H - RT}{V_M}} \tag{3.7}$$

where CED is cohesive energy density, ΔH is heat of vaporization, R is gas constant, T is temperature and V_M is the molar volume.
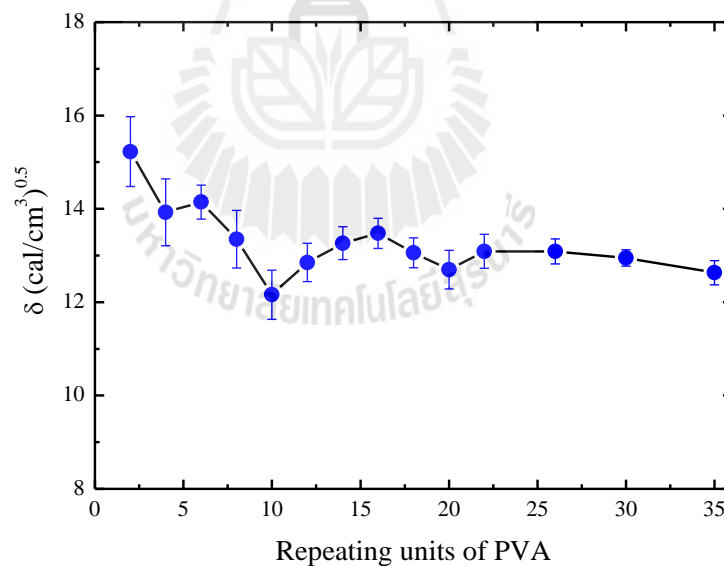
Figure 3.18 Computed solubility parameters of PVA versus number of repeating units of PVA.

The δ of PVA has been calculated for different chain lengths to obtain the minimum representative polymer chain length. The method to choose polymer

chain length used in simulation was previously described in details (Mu, Li, and Zhou, 2011). Dynamics was performed to find Hildebrand's solubility parameter (δ) plotted vs number of repeating units of the polymer. When a stable value of δ was obtained, it confirmed that the number of repeating units is sufficient for the simulation. As shown in Figure 3.18, for chain extensions up to 35 monomer units, suggests that δ did not vary much beyond 20 monomer units. δ of PVA with chain length 20 units is 12.70 ± 0.41 $(cal/cm^3)^{0.5}$. The reported experimental value for the solubility parameters of PVA (Grulke, 1999) is 12.60 $(cal/cm^3)^{0.5}$, in agreement with the estimated results. In the present work, atactic PVA of 21 units were used to generate the amorphous cell of all system.

3.4.3.2 Cation - Anion Interaction

The RDFs of Ca^{2+}– O, Ca^{2+}–Cl^-, Ca^{2+}–H, and Ca^{2+}–C were calculated from MD trajectories (Figure 3.19) to obtain the characteristic parameters including, the peak position (R_0) and its coordination number (CN) that are summarized in Table 3.6. The simulated RDF of calcium ion and oxygen atoms, $g_{Ca-O}(r)$ for PVA/salt complex, exhibits a sharp first maximum at 2.35 Å as shown in Figure 3.20. Integrating the Ca^{2+}–O RDFs over the first coordination shells gives 7.1 oxygen atoms coordinated to each Ca^{2+}. For Ca^{2+} and Cl^- interaction, $g_{Ca-Cl}(r)$ exhibits a first maximum at 6.33 Å, integrating the Ca^{2+}–Cl RDFs over the first peak gives an average only 0.25 Cl^- coordinated to each Ca^{2+}. This MD result suggests that the first coordination shell of Ca^{2+} (at distance ≤ 2.75 Å) in PVA/salt included only hydroxyl oxygen without chloride counter ion, and that the degree of coordination of Ca^{2+} by

Cl$^-$ is much weaker than that by hydroxyl oxygen, again indicating that Cl$^-$ ion can hardly form ion pairs with Ca^{2+} under the condition of this study.

The k^2-weighted experimental EXAFS spectra of CaCl$_2$/PVA sample having Ca^{2+} to hydroxyl oxygen at the equivalent ratio (Ca^{2+}:O) of 1:50, 1:25 and 1:17 are reported in Figure 3.21. The $\chi(k)$ data for all three conditions were very similar, for both frequency and amplitude of the oscillations over k range from 1 to 10 Å^{-1}, indicating that the neighbor atoms are the same element and the number of neighbor atoms is nearly independent of salt concentration. Furthermore, Ca(SCN)$_2$/PVA sample at Ca^{2+}:O ratio = 1:17 were also examined. SCN$^-$ has larger size and weaker ion pair former compared to Cl$^-$. The k^2-weighted EXAFS $\chi(k)$ spectra of these samples are reported in Figure 3.22. The spectra of Ca(SCN)$_2$/PVA sample were almost the same as that of CaCl$_2$/PVA sample, for both frequency and amplitude of the oscillations over k range from 1 to 10 Å^{-1}. The frequency matching of these oscillations means that the neighbor atoms are the same element, this experimental result suggesting that the neighbor atoms in the first shell are oxygen atom and the degree of contact ion pairing between Cl$^-$ and Ca^{2+} ions is small and negligible under the condition of this study.
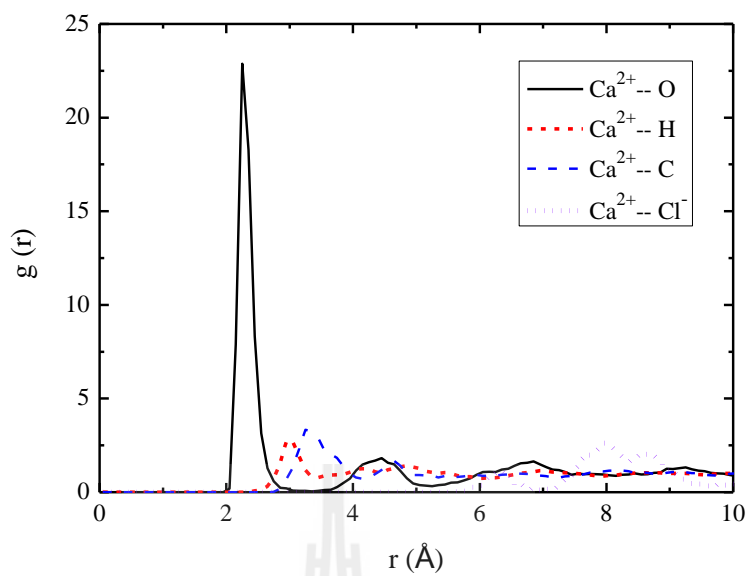
Figure 3.19 Radial distribution functions of Ca^{2+}/PVA (Ca^{2+}:O = 1:50).
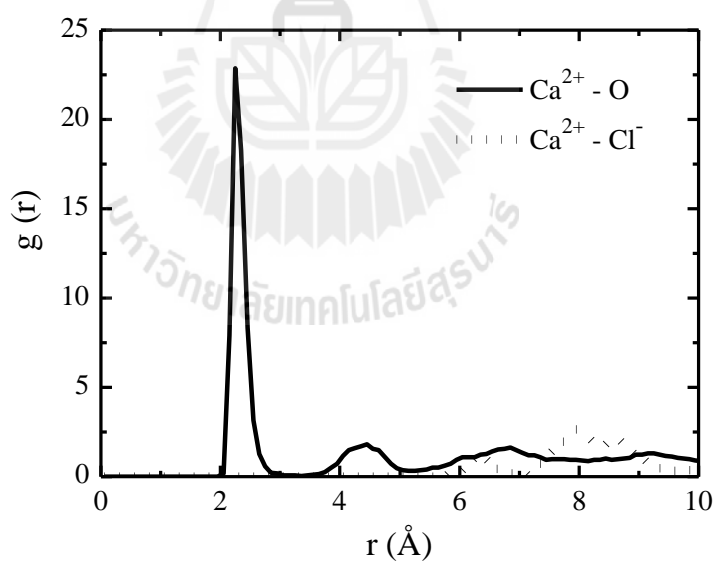
Figure 3.20 Radial distribution functions of Ca^{2+}/PVA (Ca^{2+}:O = 1:50), for Ca^{2+}-O

and Ca^{2+}-Cl$^-$ interaction.

Table 3.6 Parameter characterizing the first peak of RDF determined from MD at 298 K for Ca^{2+}/PVA (Ca^{2+}:O = 1:50).

	Ca^{2+}-O	Ca^{2+}-H	Ca^{2+}-C	Ca^{2+}-Cl⁻
R_0 (Å)	2.35	3.04	3.50	6.33
CN	7.1	10.2	12.3	0.25
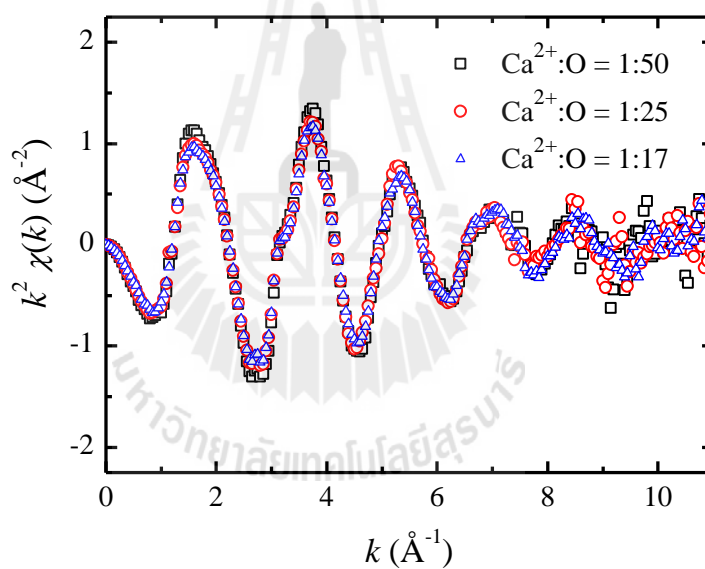
Figure 3.21 Comparison of calcium EXAFS k^2-weighted $\chi(k)$ plots for $CaCl_2$/PVA system from experiment.
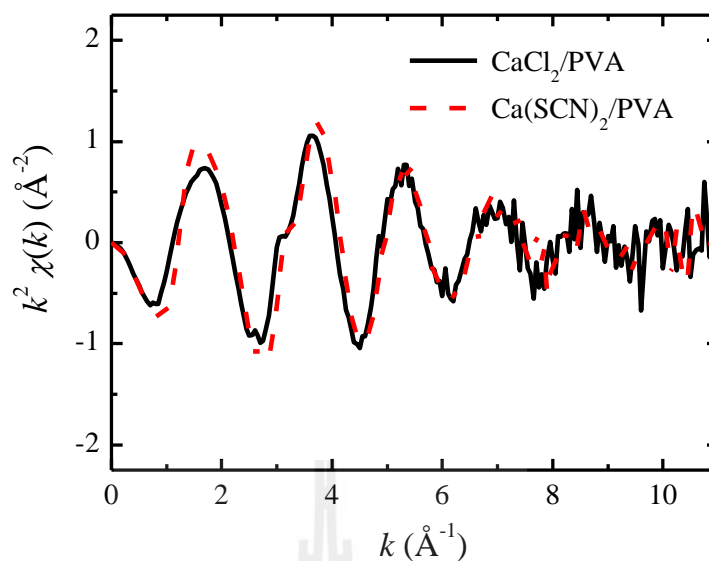
Figure 3.22 Comparison of calcium EXAFS k^2-weighted $\chi(k)$ plots for Ca^{2+}/PVA (Ca^{2+}:O = 1: 17) system from experiment.

3.4.3.3 Ca^{2+}/PVA Complexation

A comparison of k^2-weighted EXAFS spectra of $CaCl_2$/PVA sample with Ca^{2+}:O ratio = 1:50 between an experiment and MD simulation are presented in Figure 3.23. The curves are in good agreement for frequency and fair agreement for the amplitude of the oscillations over the k range from 2 to 10 $Å^{-1}$. The frequency matching of these oscillations means that the distances of Ca^{2+} - O are nearly the same for data from experiment and simulation. It is evident that the peak position is consistent between experimental and MD-EXAFS spectra.

The $|\chi(R)|$ from both experiment and simulation are compared in Figure 3.24. The $|\chi(R)|$ was generated by Fourier transform of the $k^2\chi(k)$ data. For the simulated spectra, the contribution has included from the first coordination shell (r < 2.75 Å), while the higher solvation shells has been neglected. So, MD data in Figure 3.24 do not have as many peaks as the experimental one. In general, the contribution

from second and higher solvation shells has negligible effect on the measured or simulated EXAFS spectra because the distances and the disorder are too large (Dang, Schenter, Glezakou, and Fulton, 2006). For experimental data, Figure 3.24 shown that the Fourier transforms features beyond 2.7 Å cannot be distinguished from artifacts of the transform function and noise. This is due to the fact that configurationally disorder in the second and higher solvation shells decreases their direct distribution to the EXAFS signal. There is little or no evidence of Ca-C scattering from $-CH_2-$ or $-CH_3$ in the experiment that means there is a large amount of position disorder for Ca-C distance.

For the comparison of $|\chi(R)|$ EXAFS spectra between experimental and MD simulation, the first peaks of both spectra as shown in Figure 3.24 are good agreement, which mean the radial structures in the first solvation shell of the experimental data are nearly the same as MD results. There is a remarkably good agreement between the radial structures of experimental and simulated data. These results suggest that Ca^{2+} ions are coordinated to oxygen atoms without Cl^- ion in the first shell as described in RDFs results.

Debye-Waller factors (σ^2) reflect the structural disorder of the system. We use the Gaussian distribution function (Dang, 2006) to fit the first peak of the radial distribution function of the simulation data to obtain the Debye-Waller factors (σ_G^2), $\sigma_G^2 = 0.0099$ Å^2. For the EXAFS experiment, the Debye-Waller factors (σ_i^2) were obtained by fitting the expression given by Equation 3.5 to the measured EXAFS spectra, $\sigma_i^2 = 0.0114$ Å^2. The Debye-Waller factors determined from simulation is smaller than those determined form analysis of EXAFS measurements.

Indicate that the structural disorder of experimental data is more than those of the simulation data. In overall, MD-EXAFS signals are good agreement with experiment.

The representative model of Ca^{2+} ion solvated in PVA matrix is given in Figure 3.25, Ca^{2+} ion was wrapped by seven oxygen atoms from three PVA chains. Figure 3.25 show that the conformation of PVA chains is changed upon Ca^{2+} complexation, due to the strong Coulombic attraction between Ca^{2+} ion and oxygen which tends to pull segments of the chains together, particularly as adjacent oxygens coordinate a Ca^{2+} ion. Figure 3.26 displays the probability of oxygen atoms that are coordinated with Ca^{2+} ion for PVA/$CaCl_2$ (Ca^{2+}:O ratio = 1:50) system. The coordination number of oxygen atom around Ca^{2+} for the first coordination shell (within 2.75 Å) are varied from six to eight (from 3 - 4 PVA chains); the case of seven oxygen atoms from three PVA chains coordinated to Ca^{2+} is the most frequently observed.
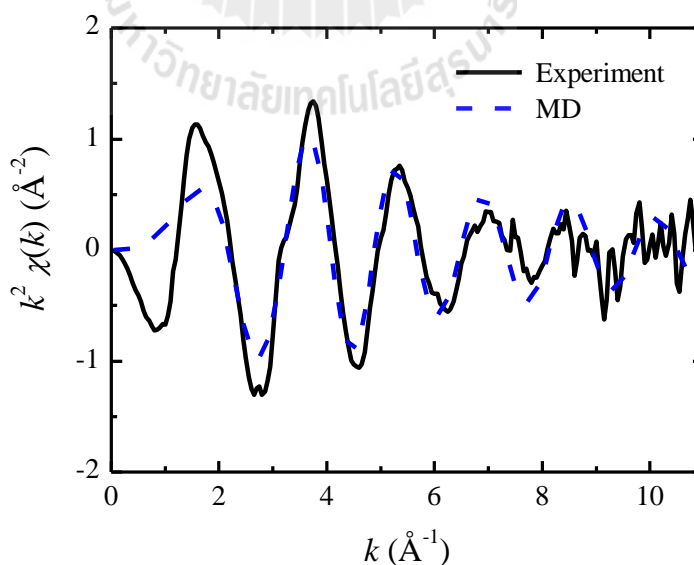
Figure 3.23 Comparison of calcium EXAFS k^2-weighted $\chi(k)$ plots for Ca^{2+}/PVA system from simulation and experiment.
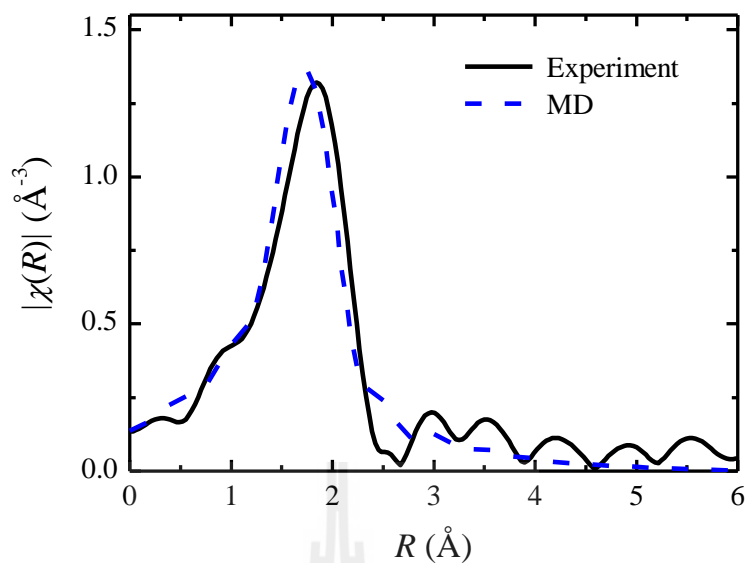
Figure 3.24 Comparison of calcium EXAFS |χ(R)| plots corresponding to the Fourier

transformed $k^2\chi(k)$ as shown in Figure 3.23.
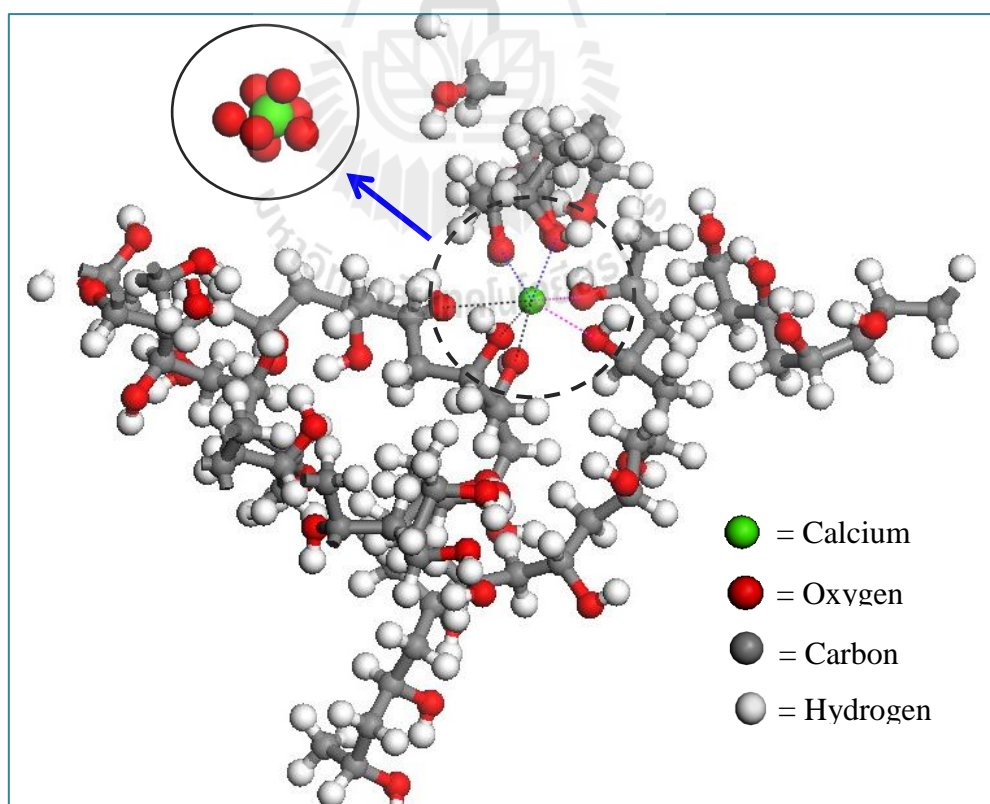
Figure 3.25 Snapshots from MD simulation of Ca^{2+}/PVA with Ca^{2+}:O = 1:50.
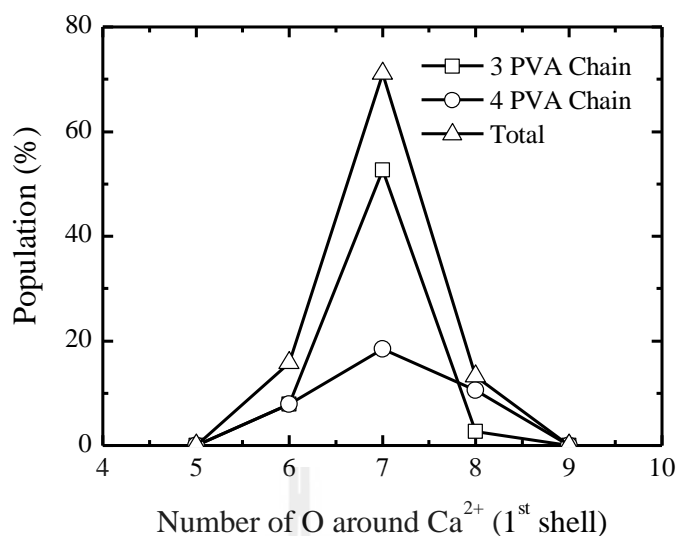
Figure 3.26 Probability of an oxygen atom coordinating a Ca^{2+} for Ca^{2+}:O = 1:50 in

PVA/CaCl$_2$ system.

3.4.3.4 Chain Conformation

X-ray diffraction (XRD) has been used to determin structure of PVA and

PVA:salt complexes (Bhargav, Mohan, Sharma, and Rao, 2009). They observed that,

on the incorporation of salt into the polymer, the degree of crystallinity of the

complex was decrease; this could be due to the disruption of the PVA structure by

salt. XRD pattern reveals that salt disrupts the crystalline nature of PVA-based

polymer electrolytes and converts them into an amorphous phase (Mohamad *et al.*,

2003). Thus, metal ion complexation with PVA chain is expected to change the

conformation of PVA chains.

To examine the conformation of PVA chains, the time-averaged

population density distributions of backbone dihedral angles (ϕ) around C*–C bonds

(Figure 3.27) were calculated from MD simulation results. The conversion to define

the conformation with heavy atoms is eclipsed as $\phi = 0º$ and called *gauche+*

conformations (*g+*) if the torsional angle has a value $0° < \phi < 120°$, *gauche-*conformations (*g-*) if $240° < \phi < 360°$, and *trans* conformations (*t*) if $120° < \phi < 240°$ as illustrated in Figure 3.28.
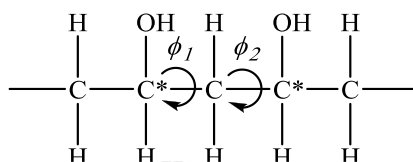
Figure 3.27   Atom sequence in PVA.

Angle	$0° < \phi < 120°$	$120° < \phi < 240°$	$240° < \phi < 360°$
Name	*gauche*$^+$ (g^+)	*trans* (*t*)	*gauche*$^-$ (g^-)
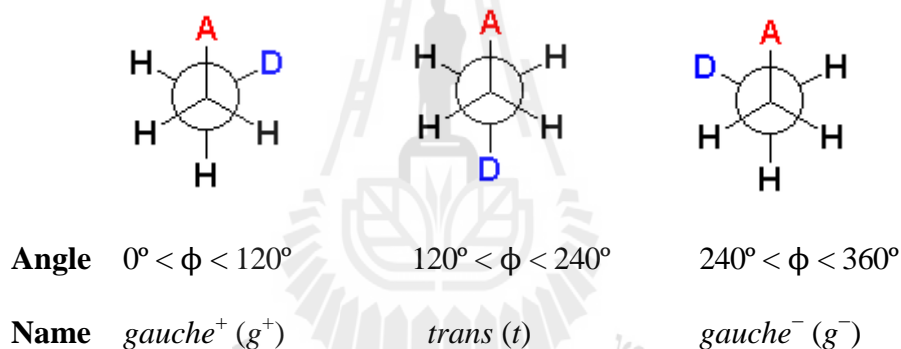
Figure 3.28 Diffinition of the conformation: g^+ if $0° < \phi < 120°$, t if $120° < \phi < 240°$, and g$^-$ if $240° < \phi < 360°$.

Comparison of dihedral angles for PVA and PVA/CaCl$_2$ is shown in Figure 3.29. For pure PVA, the dihedral angle along C*-C bonds there are three peaks: with the two smaller peaks at the two ends centered around 68° and 290° and between them a large peak centered around 179°. Similar results study by using Rotational Isomeric States (RIS) and 2,4-pentanediol as a model compound for PVA give dihedral angles at $\phi_t = 185°$, $\phi_{g+} = 65°$ and $\phi_{g-} = 290°$ (Wolf and Suter, 1984). The corresponding fractions were calculated and compared in Table 3.7. The fractions

of *trans* conformation around the C*-C bond are in good agreement with the molecular modeling of isotactic PVA (De La Rosa, Heux, Cavaillé, and Mazeau, 2002), $f_t^{C^*C} = 0.65$, $f_{g^+}^{C^*C} = 0.19$ and $f_{g^-}^{C^*C} = 0.16$. Dihedral angles distribution of PVA/CaCl$_2$ along C*–C bonds show small difference compared to pure PVA. The population of both g^+ and g^- conformations slightly increases (~4 and ~3%) relative to those of pure PVA while t state slightly decreases (~7%). This result should be from the interaction of Ca^{2+} ions with the oxygen atoms of polymer.

Main-chain torsional angles, ϕ_1 and ϕ_2, are measured in the right-handed or left-handed sense, depending on the stereochemical character of the diad along C-C*-C-C*-C PVA chain sequence. Populations of PVA diads in neat PVA and PVA/CaCl$_2$ are also shown in Figure 3.30. For neat PVA, *tt* conformers predominate and their population decrease upon Ca^{2+} complexation. While the population of *tg$^+$*, *g$^-$t*, *g$^+$g$^-$*, *g$^-$g$^+$* and *g$^-$g$^-$* conformers increases. The decrease of the population of the most stable structure, the *tt* conformer, upon Ca^{2+} complexation indicates that the Coulombic attraction between Ca^{2+} ion and oxygen tends to pull segments of the chains together. The preference for the *tg$^+$* and *g$^-$t* conformation in PVA/CaCl$_2$ indicates that the *gauche* angle around C*-C bond enables hydroxyl oxygen atom at the side chain to coordinate with Ca^{2+}, and the *trans* state implies a further distance between the side chain and Ca^{2+} ion which lowers the repulsions than *gauch* state.

The segment of the chain that prefers g^+ or g^- state should be the inner portion of a PVA chain that includes at least two adjacent oxygen atoms that are coordinated to a Ca^{2+}, this portion of a chain forms a local structure of Ca^{2+} - O complexation. If only one oxygen atom from the end of a PVA chain complex with a Ca^{2+} ion, there should be a segment that prefers t state. These results suggest that PVA

backbone adopt a *gauche* conformation which facilitates oxygen atoms at the side chain to coordinate with Ca^{2+} ion. The complexation of Ca^{2+} ion with hydroxyl oxygens is a short range interaction and influences only the local structures of PVA chain.
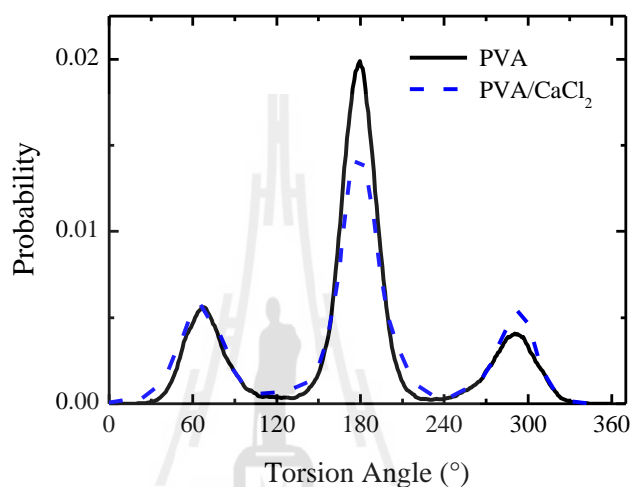
Figure 3.29 Average population density distributions of PVA backbone dihedral angles around C*-C bond.
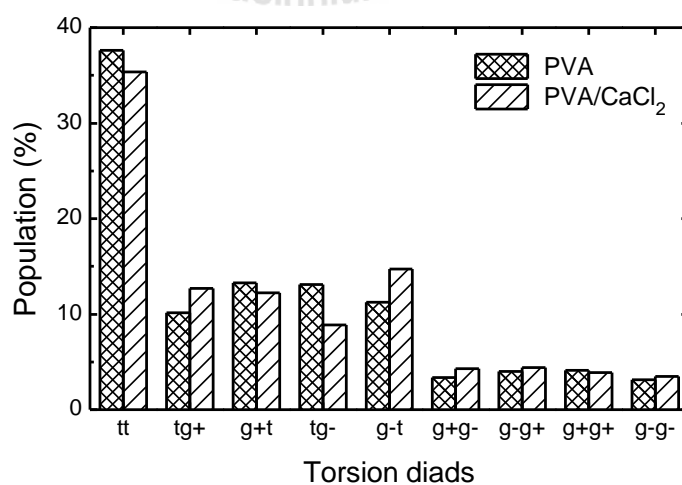
Figure 3.30 Populations of conformational (C-C*-C-C*-C backbone atom sequences) for pure PVA and PVA/CaCl$_2$ (Ca^{2+}:O = 1:50).

Table 3.7 The population of *gauche*$^{\pm}$ and *trans* in PVA and PVA/CaCl$_2$.

Torsion	Population					
	g$^+$	t	g$^-$	g$^{+(a)}$	t$^{(a)}$	g$^{-(a)}$
PVA; CC*CC*	0.20	0.63	0.17	0.19	0.65	0.16
PVA:CaCl$_2$; CC*CC* , M:O = 1:50	0.24	0.56	0.20	-	-	-

[a]De La Rosa, Heux, Cavaillé, and Mazeau (2002) for isotactic PVA.

3.5 Calcium ion/Poly(acrylic acid)

3.5.1 EXAFS Experimental Details

Anhydrous calcium chloride (CaCl$_2$ 99.99%, Aldrich) and Poly(acrylic acid) solution 35%(wt) in H$_2$O, MW = 100,000 g/mol, from Aldrich were used without further purification. Distilled, deionized water was use throughout. Since CaCl$_2$/PAA film system might form Ca-Cl contact ion pairs that would complicate the interpretation of the solvated Ca^{2+} ion. To check if there is the ion pair in our system, a series of concentration of Ca^{2+}:O ratio = 1:100, 1:50 and 1:35 for CaCl$_2$/PAA were studies. Furthermore we also examined a mixture of Ca(SCN)$_2$ in PAA with Ca^{2+}:O = 1:34. Because of its much large anion size and it is a weak ion pair former.

PAA and CaCl$_2$ aqueous solution were mix together. PAA/CaCl$_2$ mixture solutions were stirred overnight at room temperature to achieve complete dissolution, then the solution was transferred to plastic plates and allowed to dry and solidity at an atmosphere condition in a dust free chamber and then the resulting dried films were cut to small piece with the size of 1.5 × 2.5 cm. The sample were then dried in vacuum oven at 80°C for 24 h to eliminate the solvent, continue drying in vacuum

oven at room temperature for another 6 h, after that PAA/CaCl$_2$ films were wrapped with polypropylene film and kept in zipper plastic bag and stored in desiccator until future use. EXAFS experiment, sample handing method for Ca^{2+} in PAA are the same with Ca^{2+} in water system.

3.5.2 Computational Details

Molecular dynamics simulation was carried out by using Materials Studio 4.2 simulation package provided by National Nanotechnology Center, Thailand. The COMPASS forcefiled was employed for all simulation. Bulk amorphous states for neat PAA and its mixture with salt were built using the cubic unit cell under the periodic boundary condition by using Amorphous Cell module. The neat PAA system consisting of 10 PAA chains with chain length 20 monomer units in a simulation box, Density of PAA taken from the literature (Grulke, 1999) was 1.23 g/cm^3. For Ca^{2+}/PAA system, 10 PAA chains with chain length 20 monomer units were mixwd with Ca^{2+} ions and Cl$^-$ ions in a simulation box with Ca^{2+}:O = 1:100 (equivalent to experimental concentration). Density of the mixture system was calculated from the density of individual component and their volume fraction of each component. The simulation procedure, data analysis and EXAFS spectra calculation methods were the same as that in PVA system.
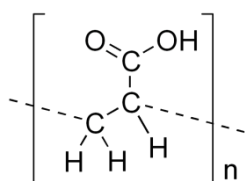
Figure 3.31 PAA repeating unit.

Table 3.8   Charge parameters used in the simulation.

Molecule	Atom	Description	Charge
PAA	H	Alkane hydrogen	0.053
	H	Hydroxyl hydrogen	0.410
	C(H$_2$)	Alkane carbon	-0.106
	C(H$_1$)	Alkane carbon	-0.053
	C(=)	Carboxyl carbon	0.495
	O(=)	Carboxyl oxygen	-0.450
	O(−)	Hydroxyl oxygen	-0.455
Ca^{2+}	Ca^{2+}	Calcium ion	2.000
Cl$^-$	Cl$^-$	Chlorine ion	-1.000

3.5.3 Results and Discussions

3.5.3.1 Cation - Anion Interaction

The RDFs of Ca^{2+}– O(=), Ca^{2+}– O(−), and Ca^{2+}–Cl$^-$ were calculated from MD trajectories to obtain the characteristic parameters including, the peak position (R$_0$) and its coordination number (CN) that are summarized in Table 3.9. The simulated RDF of calcium ion and carboxyl oxygen atoms, for PAA/salt complex, exhibits a sharp first maximum at 2.38 Å as shown in Figure 3.32. Integrating the Ca^{2+}–O(=) RDFs over the first coordination shells gives 7.6 oxygen atoms coordinated to each Ca^{2+}. For Ca^{2+} and Cl$^-$ interaction, g$_{Ca-Cl}$(r) exhibits the first maximum at 9.5 Å as shown in Figure 3.33. Integrating the Ca^{2+}–Cl RDFs over the first peak gives an average only 0.45 Cl$^-$ coordinated to each Ca^{2+}. This MD result suggests that the first coordination shell of Ca^{2+} (at distance ≤ 2.85 Å) in PAA/salt

included carboxyl oxygen without chloride counter ion, and that the degree of coordination of Ca^{2+} by Cl^- is much weaker than that by carboxyl oxygen, again indicating that Cl^- ion can hardly form ion pairs with Ca^{2+} under the condition of this study.

The k^2-weighted experimental EXAFS spectra of $CaCl_2$/PAA sample having Ca^{2+} to hydroxyl oxygen at the equivalent ratio (Ca^{2+}:O) of 1:100, 1:50 and 1:34 are reported in Figure 3.34. The $\chi(k)$ data for all three conditions are very similar, for both frequency and amplitude of the oscillations over the k range from 2 to 10 $Å^{-1}$, indicating that the neighbor atoms are the same element and the number of neighbor atoms is nearly independent of salt concentration. Furthermore, $Ca(SCN)_2$/PAA sample at Ca^{2+}:O ratio = 1:34 were also examined. SCN^- has larger size and weaker ion pair formed compared to Cl^-. The k^2-weighted EXAFS $\chi(k)$ spectra of these samples are reported in Figure 3.35. The spectra of $Ca(SCN)_2$/PAA sample were almost the same as that of the $CaCl_2$/PAA sample, for both frequency and amplitude of the oscillations over the k range from 2 to 10 $Å^{-1}$. The frequency matching of these oscillations means that the neighbor atoms are the same element, this experimental result suggests that the neighbor atoms in the first shell are oxygen atom and the degree of contact of ion pairing between Cl^- and Ca^{2+} ions is small and negligible under the condition of this study.
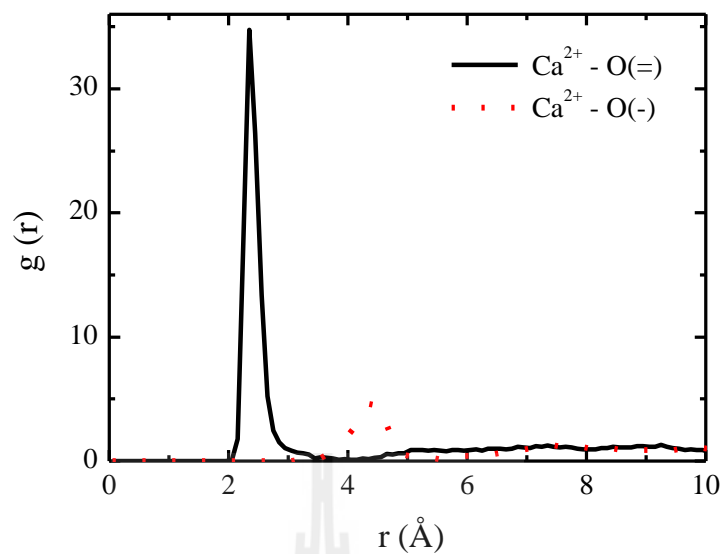
Figure 3.32 Radial distribution functions of Ca^{2+}/PAA (Ca^{2+}:O = 1:100) for Ca^{2+}-O interaction.
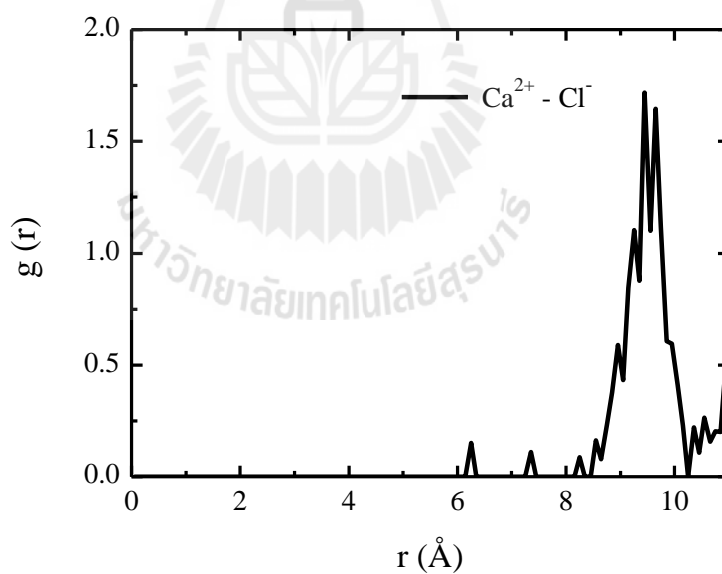
Figure 3.33 Radial distribution functions of Ca^{2+}/PAA (Ca^{2+}:O = 1:100), for Ca^{2+}-Cl^- interaction.

Table 3.9   Parameter characterizing the first peak of RDF determined from MD at

298 K for Ca^{2+}/PAA (Ca^{2+}:O = 1:100).

Interaction	R (range, Å)	R_0 (Å)	CN
Ca^{2+}-O(=)	1.95 - 2.85	2.38	7.6
Ca^{2+}-O(-)	3.05 - 5.25	4.37	8.3
Ca^{2+}-Cl^-	8.45 - 10.25	9.50	0.45
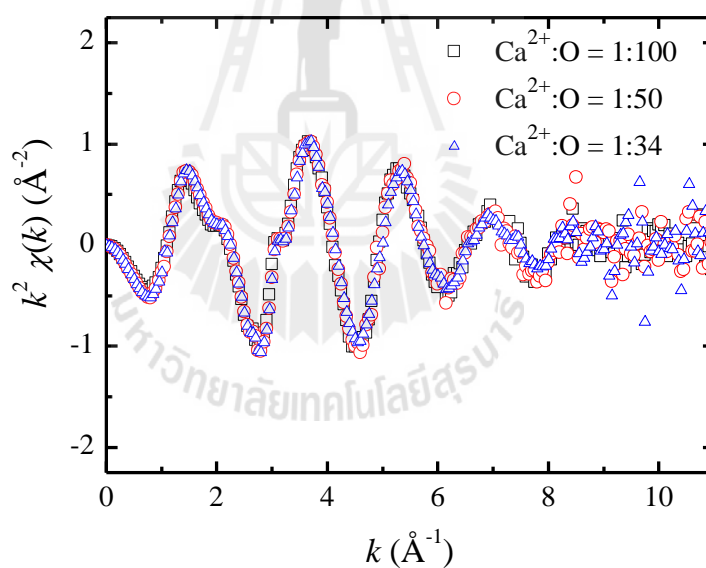
Figure 3.34 Comparison of calcium EXAFS k^2 -weighted $\chi(k)$ plots for $CaCl_2$/PAA

system from experiment.
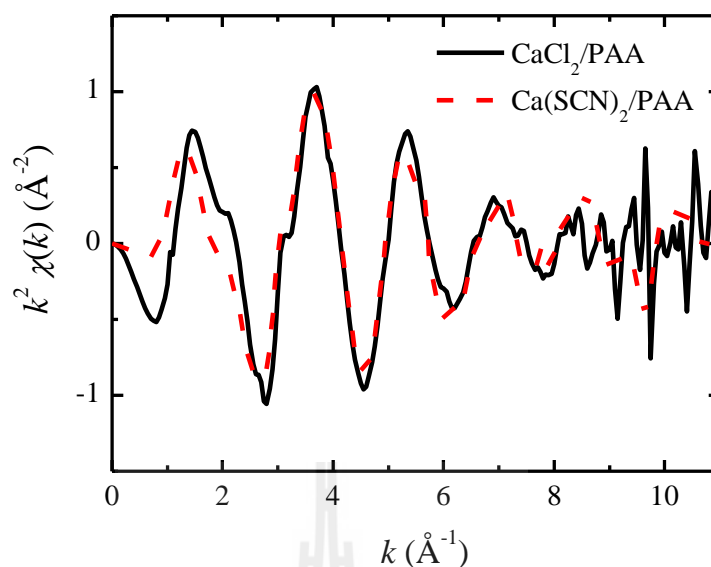
Figure 3.35 Comparison of calcium EXAFS k^2-weighted $\chi(k)$ plots for Ca^{2+}/PAA

(Ca^{2+}:O = 1: 34) system from experiment.

3.5.3.2 Ca^{2+}/PAA Complexation

A comparison of k^2-weighted EXAFS spectra of $CaCl_2$/PAA sample with

Ca^{2+}:O ratio = 1:100 between the experiment and MD simulation is presented in

Figure 3.36. The curves are in good agreement for frequency and fair agreement for

the amplitude of the oscillations over the k range from 2 to 10 $Å^{-1}$, it is evident that

the peak position is consistent between the experimental and MD-EXAFS spectra.

The $|\chi(R)|$ from both the experiment and simulation are compared in Figure 3.37. The

$|\chi(R)|$ was generated by Fourier transform of the $k^2\chi(k)$ data. For the experimental

data, Figure 3.37 shows that the Fourier transform features beyond 2.7 Å cannot be

distinguished from the artifacts of the transform function and noise. This is due to the

fact that a configurationally disorder in the second and higher solvation shells

decreases their direct distribution to the EXAFS signal. There is little or no evidence

of Ca-C scattering from $–CH_2–$ or $–CH$ in the experiment that means there is a large

amount of position disorder for Ca-C distance. For the comparison of $|\chi(R)|$ EXAFS spectra between the experiment and MD simulation, the first peaks of both spectra as shown in Figure 3.37 are in good agreement. This means the radial structures in the first solvation shell of the experimental data are nearly the same as the MD results. Debye-Waller factors (σ^2) reflect the structural disorder of the system. The Debye-Waller factors determined from simulation ($\sigma_G^2 = 0.0095$ Å^2.) is smaller than those determined form analysis of EXAFS measurements ($\sigma_i^2 = 0.0121$ Å^2.). Indicate that the structural disorder of experimental data is more than those of the simulation data. Again, there is a remarkably good agreement between the radial structures of the experimental and simulated data. These results suggest that Ca^{2+} ions are coordinated to oxygen atoms without Cl$^-$ ion in the first shell as described in the RDF results.

The representative model of Ca^{2+} ion solvated in PAA matrix is given in Figure 3.38, Ca^{2+} ion was wrapped by about seven oxygen atoms from four PAA chains. Figure 3.39 displays the probability of oxygen atoms that are coordinated with Ca^{2+} ion for PAA/CaCl$_2$ (Ca^{2+}:O ratio = 1:100) system. The coordination number of oxygen atoms around Ca^{2+} ion for the first coordination shell (within 2.85 Å) are varied from seven to nine (from 3 to 4 PAA chains); the case of seven oxygen atoms from four PAA chains coordinated to Ca^{2+} is the most frequently observed.
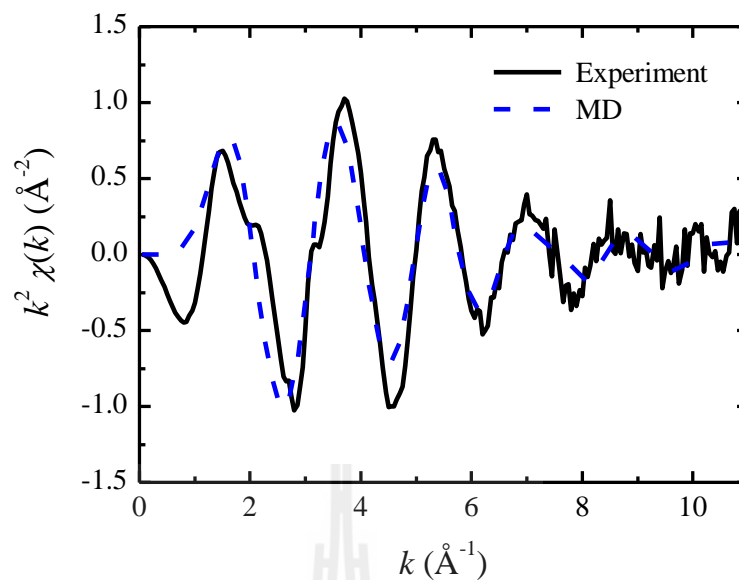
Figure 3.36 Comparison of calcium EXAFS k^2-weighted $\chi(k)$ plots for $CaCl_2$/PAA

system from simulation and experiment.
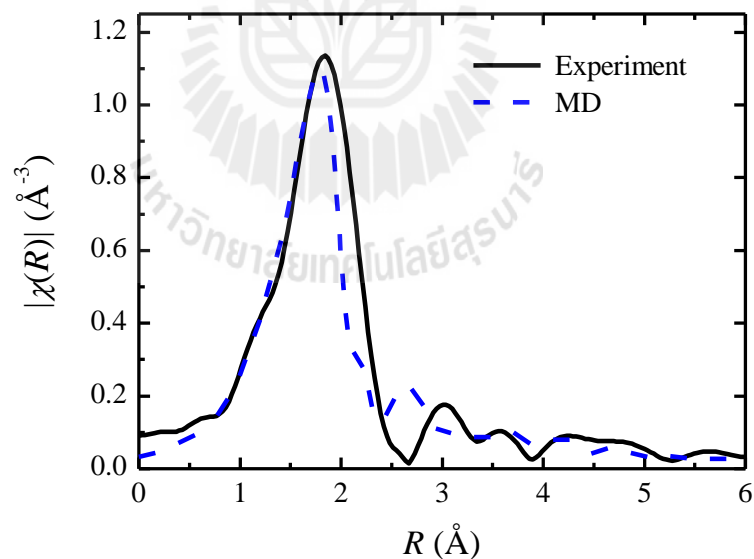
Figure 3.37 Comparison of calcium EXAFS $|\chi(R)|$ plots corresponding to the Fourier

transformed $k^2\chi(k)$ as shown in Figure 3.36.
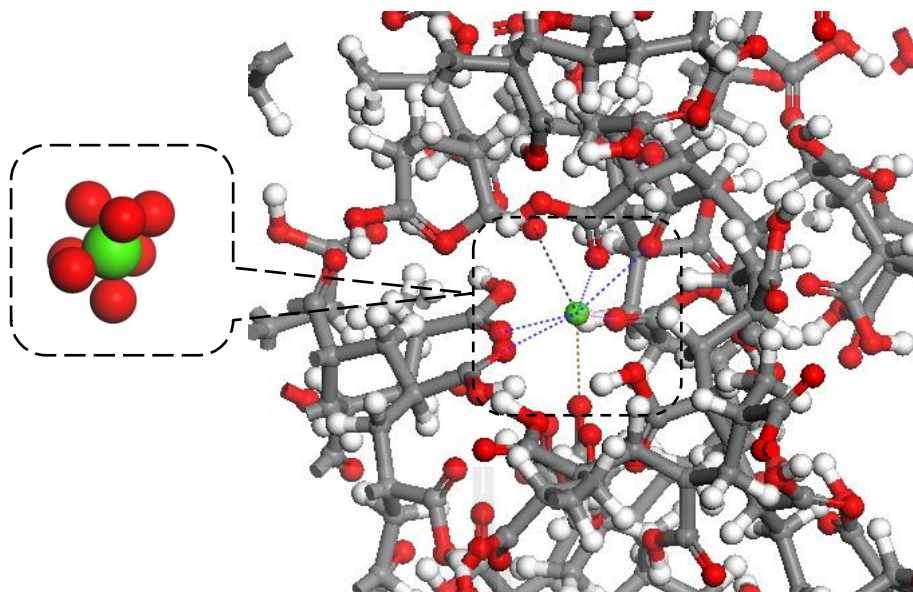
Figure 3.38 Representative snapshot from MD simulation of Ca^{2+}/PAA with Ca^{2+}:O
= 1:100 (Colors: hydrogen atoms: white, oxygen atoms: red, carbon
atoms: gray, calcium atoms: green).
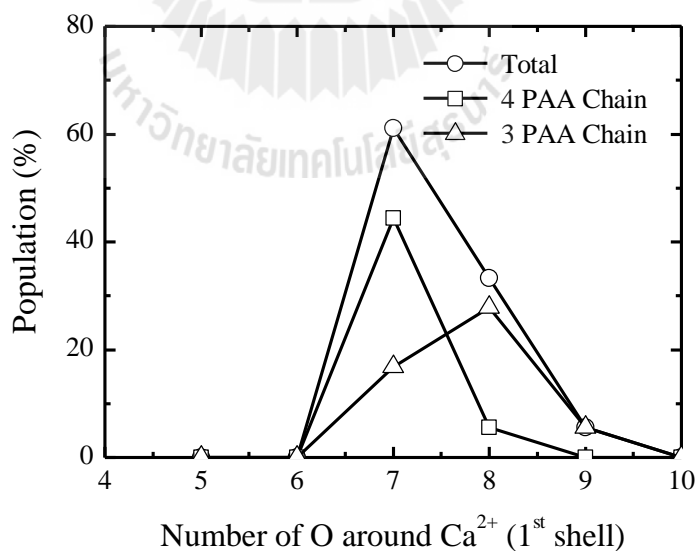
Figure 3.39 Probability of an oxygen atom coordinating a Ca^{2+} for Ca^{2+}:O = 1:100 in
PAA/CaCl$_2$ system.

3.5.3.3   Chain Conformation

To examine the conformation of PAA chains, the time-averaged population density distributions of backbone dihedral angles (ϕ) around C*–C bonds were calculated from MD simulation results. Comparison of dihedral angles for PAA and PAA/CaCl$_2$ is shown in Figure 3.40. For neat PAA, the dihedral angle along C*-C bonds, there are three peaks: with the two smaller peaks at the two ends centered around 59º and 303º and between them a large peak centered around 183º. The corresponding fractions were calculated and compared in Table 3.10.

Dihedral angles distribution of PAA/CaCl$_2$ along C*–C bonds shows slightly difference compared to neat PAA. The population g^- conformations slightly increases (~1%) relative to those of neat PAA while t state slightly decreases (~1%). The segment of the chain that prefers the *gauche* state should be the inner portion of a PAA chain that includes at least two adjacent carboxyl oxygen atoms that are coordinated to a Ca^{2+}, this portion of chain forms a local structure of Ca^{2+} - O complexation. If only one oxygen atom from the end of a PAA chain complex with a Ca^{2+} ion, there should be a segment that prefers t state. These results suggest that PAA backbone adopt the *gauche* conformation to facilitate oxygen atoms at the side chain to coordinate with Ca^{2+} ion. The complexation of Ca^{2+} ion with carboxyl oxygen is a short range interaction and influences only the local structures of PAA chain.

Main-chain torsional angles, ϕ_1 and ϕ_2, are measured in the right-handed or left-handed sense, depending on the stereochemical character of the diad along C-C*-C-C*-C PAA chain sequence. Populations of PAA diads in neat PAA and PAA/CaCl$_2$ are also shown in Figure 3.41. For neat PAA, tt conformers predominate and their population decrease upon Ca^{2+} complexation. While the population of tg^+,

g^+t, g^+g^-, and g^-g^+ conformers increases. A decrease of the population of the most stable structure, the *tt* conformer, upon Ca^{2+} complexation indicates that the Coulombic attraction between Ca^{2+} ion and oxygen tends to pull the segment of the chains together. The preference for the tg^+ and g^+t conformation in PAA/CaCl$_2$ indicates that the *gauche* angle around C*-C bond enables carbonyl oxygen atom at the side chain to coordinate with Ca^{2+}, and the *trans* state implies a further distance between the side chain and Ca^{2+} ion which lowers the repulsion than *gauch* state.

Table 3.10 The population of *gauche*$^\pm$ and *trans* in PAA and PAA/CaCl$_2$.

Torsion	Population		
	g^+	t	g^-
PAA; CC*CC*	0.27	0.52	0.21
PAA:CaCl$_2$; CC*CC* , M:O = 1:100	0.27	0.51	0.22
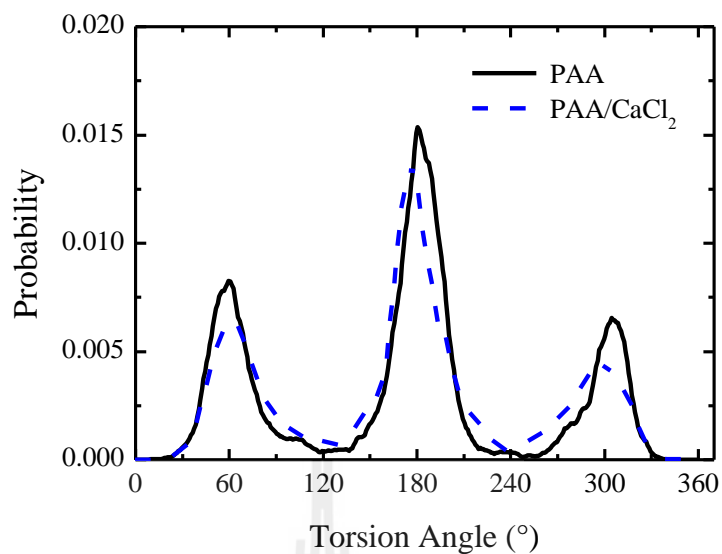
Figure 3.40 Average population density distributions of PAA backbone dihedral angles around C*-C bond.
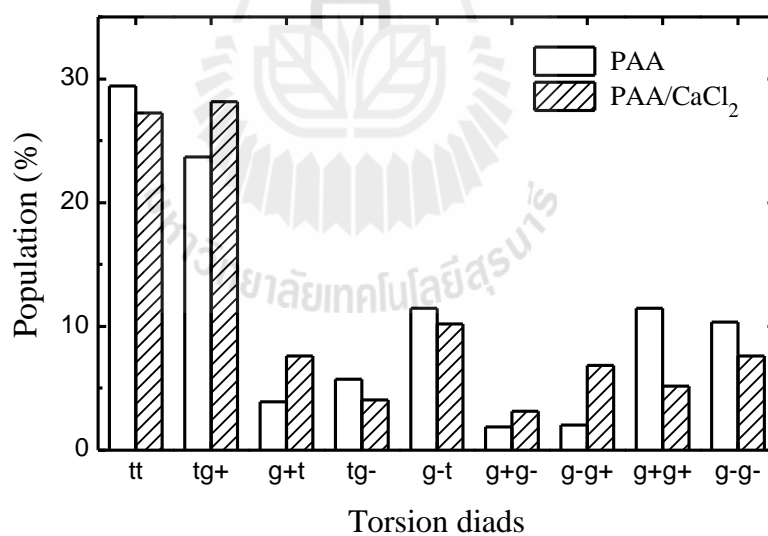
Figure 3.41 Populations of conformational (C-C*-C-C*-C backbone atom sequences) for pure PAA and PAA/CaCl$_2$ (Ca^{2+}:O = 1:100).

3.6 Calcium ion/Pectin and Calcium ion/Alginate

Pectin and alginate are two characteristic examples of natural polyelectrolytes undergoing chain-chain association and forming hydrogels upon addition of divalent cations e.g., Ca^{2+}. Calcium-induced gelation is resulted from specific and strong interactions between calcium ions and guluronate and galacturonate block in alginate and pectin, respectively. The analogy is drawn largely because of the strong simililarities of the sructures and calcium-binding behavior of the two polymers. To gain more understanding of these network structure, the complexation geometry of Ca^{2+}/pectin and Ca^{2+}/alginate were investigated using MD simulation to obtain detailed three-dimensional molecular models. Finally, the structure data obtained were used to calculate EXAFS spectra and were directly compared with experimental EXAFS spectra.

3.6.1 Experimental Details

Anhydrous calcium chloride ($CaCl_2$ 99.99%, Aldrich), Low methoxyl, Polygalacturonic acid (Pectin) from oranges, (Aldrich) and Alginate from brown algae (Fluka) were used without further purification. Distilled, deionized water was used throughout. Pectin was dissolved in 0.12 M NaOH solution to prepare a sodium pectinate solution at a concentration of 2%(w/v) and then sodium pectinate solution was added drop wise into $CaCl_2$ aqueous solution, hydrogel were formed in this step (stir vigorously for 30 minutes). The formed hydrogel beads were allowed to harden for 12 h in the $CaCl_2$ solution. After that the hydrogel were filtered and washed repeatedly with deionized water, then transferred to plastic plates and allowed to dry at 40 ˚C in hot air oven for 2 days, then grinding it in a mortar and dry again in

vacuum oven at room temperature for 12 h, then stored it in a desiccator before further analytical testing. For the Calcium Alginate gels, the preparation method was the same as Pectin gel. EXAFS experiment spectra, the beamline handing methods for Ca^{2+} in Pectin and Alginate are the same with Ca^{2+} in water system (see section 3.2.1). The experimental EXAFS data was then directly compared with simulated EXAFS spectra.

3.6.2 Computational Details

Molecular dynamics simulation of calcium ion in pectin (Polygalacturonic acid) at 298 K, were performed under NVT ensemble with COMPASS force field. For calcium ion in pectin simulation, the cubic boxes contained Polygalacturonate chains with the chain length of 12 repeating units with Ca^{2+} ions in a simulation box with Ca^{2+}:monomer = 1:4 (that equivalent with experimental). Then, simulation systems were allowed to vary its volume by performing a NPT ensemble (Number of molecules, Pressure and Temperature constant) run at 298 K and 1.0 atm to obtain an equilibrium density. The amorphous assembly was energy-minimized using the Smart minimization method with a convergence level of 0.01 kcal/mol/Å. The Smart minimizer starts with the steepest descent method, followed by the conjugate gradient method and ends with a Newton method. After that, short NVT (Number of molecules, volume and Temperature constant) simulations were run for 0.2 ns at 800 K to relax the structures. Then another 1 ns dynamics with time step 1 fs at 298 K was performed in the NVT ensemble for data analysis. Simulation procedures of Ca^{2+}/Alginate (polygururonate) are the same as Pectin simulation procedures. In all simulation, the trajectories were saved every 5000 fs for subsequent analysis.

Table 3.11 Charge parameters used in the simulation.

Molecule	Atom	Description	Charge
Polygalacturanate,	H	Alkane hydrogen	0.053
Polygururonate	H	Hydroxyl hydrogen	0.410
	C(-O)	Carboxylate carbon	0.297
	O	Carboxylate oxygen	-0.534
	O	Hydroxyl oxygen	-0.570
	O	Ether oxygen	-0.320
Ca^{2+}	Ca^{2+}	Calcium ion	2.000
Cl^-	Cl^-	Chlorine ion	-1.000

3.6.3   Results and Discussions of Calcium/Pectin

3.6.3.1 Radial Distribution Function (Ca^{2+}/Pectin)

Molecular dynamics simulation of the Ca^{2+}/polygalacturonate was carried out to investigate the specific groups of polygalacturonate that interact with Ca^{2+} ion. To obtain a clear molecular picture for the polygalacturonate complex with metal ions, oxygen atoms were separated to O1-, O2h, and O2e that represent to carboxylate oxygen, hydroxyl oxygen, and ether oxygen respectively. Figure 3.42 shows the atom labeling of polygalacturonate. The RDFs of Ca^{2+}– O1–, Ca^{2+}– O2h, and Ca^{2+}– O2e were calculated from MD trajectories to obtain the characteristic parameters including, the peak position (R_0) and its coordination number (CN) that are summarized in Table 3.12.

The simulated RDF of calcium ion and oxygen atoms, for Ca^{2+}/Pectin complex are shown in Figures 3.43, to compare the coordination of Ca^{2+} by all

oxygen species. RDFs were calculated and plotted separately as seen in Figure 3.44, to examine how Ca^{2+} cations are coordinated by oxygen atoms. The simulated RDF of calcium ion and carboxylate oxygen atoms (O1-), for Pectin/Ca^{2+} complex, exhibits a sharp first maximum at 2.07 Å as shown in Figure 3.44 (left). Integrating the Ca^{2+}–O1- RDFs over the first coordination shells gives 4.4 oxygen atoms coordinated to each Ca^{2+}. The simulated RDF of calcium ion and hydroxyl oxygen atoms (O2h), for Pectin/Ca^{2+} complex, exhibits a sharp first maximum at 2.36 Å as shown in Figure 3.44 (right). Integrating the Ca^{2+}–O2h- RDFs over the first coordination shells gives 1.9 oxygen atoms coordinated to each Ca^{2+}. The simulated RDF of calcium ion and ether oxygen atoms (O1-), for Pectin/Ca^{2+} complex, exhibits a sharp first maximum at 2.37 Å as shown in Figure 3.44 (bottom). Integrating the Ca^{2+}–O2e RDFs over the first coordination shells gives 0.4 oxygen atoms coordinated to each Ca^{2+}.

Figure 3.43 shows that the O1-, O2h, and O2e groups are located within the first shell of the Ca^{2+} ion (r ≤ 2.75 Å). The center of the first peak of the O1- groups is smaller than O2h and O2e groups, thus the interaction between the O1- groups and calcium ion could be stronger than those of the O2h or O2e groups. Due to the strong interaction between Ca^{2+} and polygalacturonate, Ca^{2+} can act as a transient cross-linker to enlarge the interaction of functional groups of polygalacturonate. The representative model of Ca^{2+} ion solvated in polygalacturonate matrix is given in Figure 3.45, Ca^{2+} ion was wrapped by seven oxygen atoms from two polygalacturonate chains. Ca^{2+} ions were trapped within the chelation structure between polygalacturonate that corresponded to a stable Ca^{2+}/polygalacturonate complex formation.
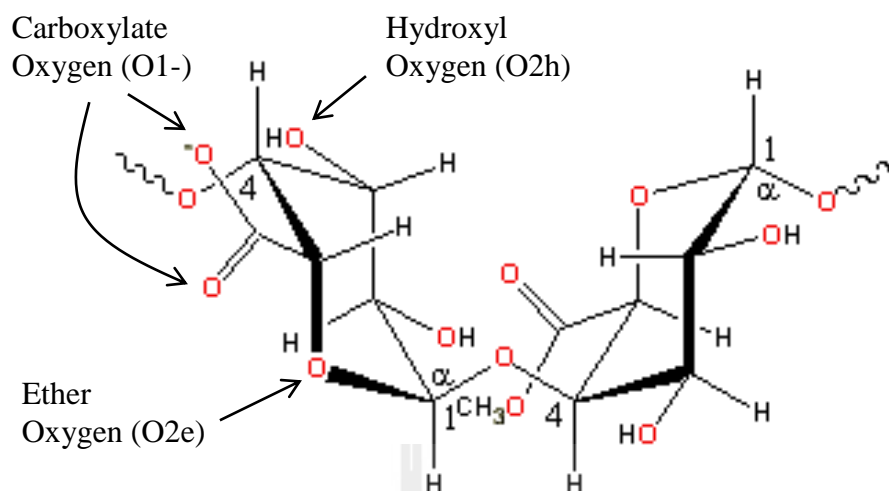
Figure 3.42 Atom labeling of Pectinate (polygalacturonate).
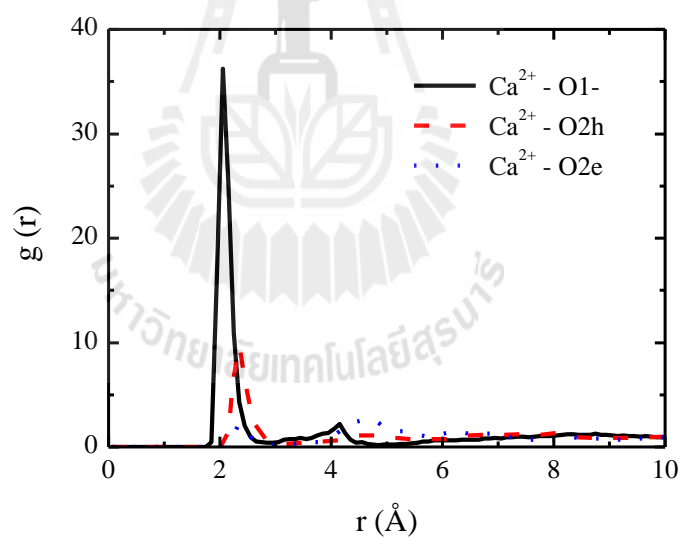
Figure 3.43 Radial distribution functions of Ca^{2+}/Polygalacturonate.
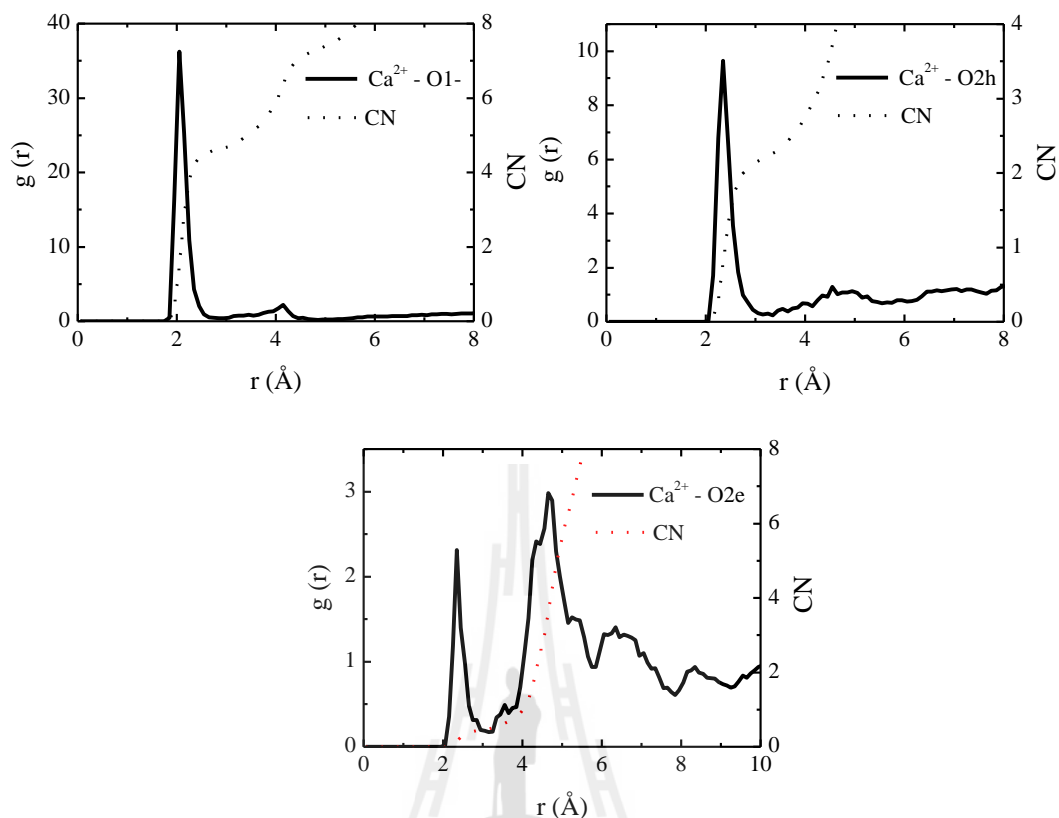
Figure 3.44 Radial distribution functions of Ca^{2+}/Polygalacturonate, plotted separately.

Table 3.12 Parameter characterizing the first peak of RDF determined from MD at 298 K for Ca^{2+}/Polygalacturonate.

Atom Pair	R_0 (Å)	CN	limited of integration
Ca^{2+}- O1-	2.07	4.4	$0 \leq R \leq 2.55$
Ca^{2+}- O2h	2.36	1.9	$0 \leq R \leq 2.75$
Ca^{2+}- O2e	2.37	0.4	$0 \leq R \leq 2.75$
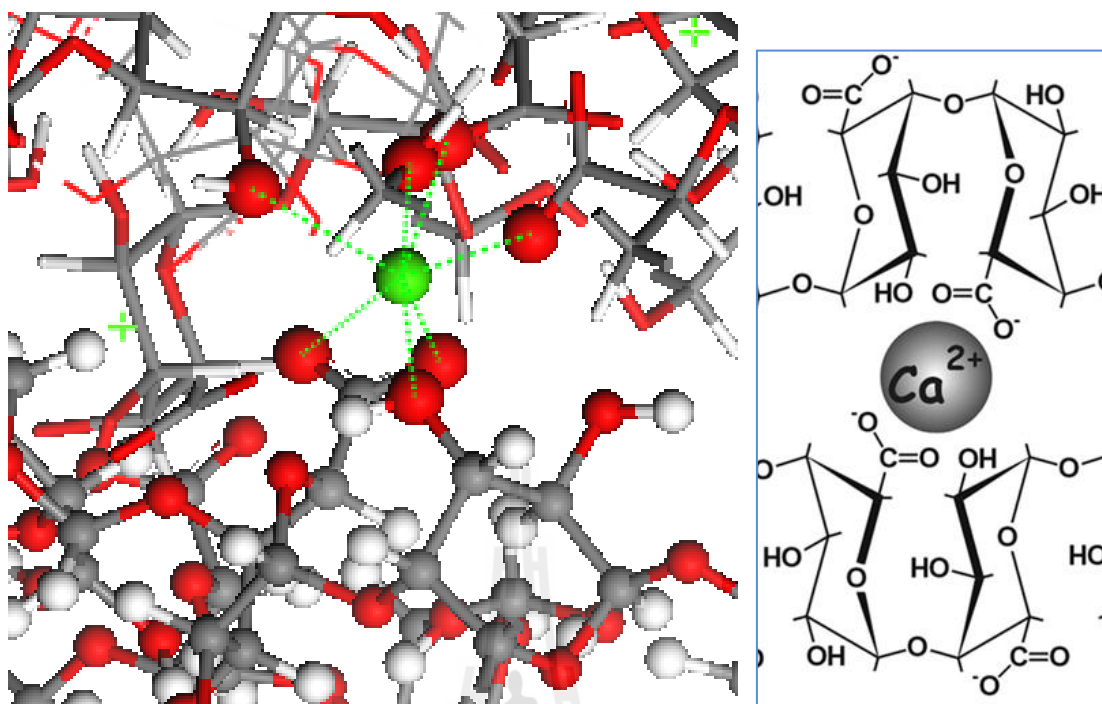
Figure 3.45 Schematics display the Ca^{2+} ions are coordinated by two different chain

of polygalacturonate. (Colors: calcium cations–green, oxygen atoms–red,

carbon atom–gray, and hydrogen atoms–white).

3.6.3.2 MD-EXAFS

A comparison of k^2-weighted EXAFS spectra of CaCl₂/

polygalacturonate sample between an experiment and MD simulation are presented in

Figure 3.46. The curves are in good agreement for frequency and fair agreement for

the amplitude of the oscillations over the k range from 2 to 10 Å^{-1}, it is evident that

the peak position is consistent between experimental and MD-EXAFS spectra. The

$|\chi(R)|$ from both experiment and simulation are compared in Figure 3.47. The $|\chi(R)|$

was generated by Fourier transform of the $k^2\chi(k)$ data. There is little or no evidence of

Ca-C scattering from –CH₂– or –CH₃ in the experiment that means there is a large

amount of position disorder for Ca-C distance. For the comparison of $|\chi(R)|$ EXAFS

spectra between experimental and MD simulation, the first peaks of both spectra as shown in Figure 3.47 are good agreement. That mean the radial structures in the first solvation shell of the experimental data are nearly the same with MD results. Debye-Waller factors (σ^2) reflect the structural disorder of the system. The Debye-Waller factors determined from simulation ($\sigma_G^2 = 0.0098$ Å^2.) is smaller than those determined form analysis of EXAFS measurements (σ_i^2=0.0110 Å^2.). Indicate that the structural disorder of experimental data is more than those of the simulation data. Again, there is a remarkably good agreement between the radial structures of experimental and simulated data.

Figure 3.46 Comparison of calcium EXAFS k^2-weighted $\chi(k)$ plots for Ca^{2+}/Polygalacturonate from experiment and MD simulation.
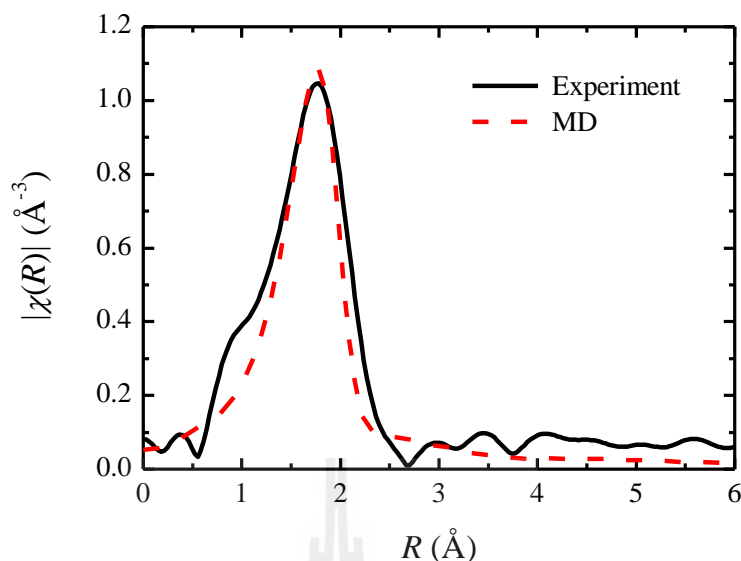
Figure 3.47 The $|\chi(R)|$ plots corresponding to the Fourier transformed $k^2\chi(k)$ as shown in Figure 3.46.

3.6.4 Results and Discussions of Calcium ion/Alginate

3.6.4.1 Radial Distribution Function (Ca^{2+}/Alginate)

Figure 3.48 shows the atom labeling of polyguluronate. The RDFs of Ca^{2+}– O1–, Ca^{2+}– O2h, and Ca^{2+}– O2e were calculated from MD trajectories to obtain the characteristic parameters including, the peak position (R_0) and its coordination number (CN) that are summarized in Table 3.13. The simulated RDF of calcium ion and oxygen atoms, for Ca^{2+}/Alginate complex are shown in Figures 3.49, to compare the coordination of Ca^{2+} by all oxygen species. RDFs were calculated and plotted separately as seen in Figure 3.50, to examine how Ca^{2+} cations are coordinated by oxygen atoms.

Figure 3.49 shows that the O1-, O2h, and O2e groups are located within the first shell of the Calcium ion ($r \leq 2.75$ Å). The center of the first peak of the O1-groups is smaller than O2h and O2e groups, thus the interaction between the O1-

groups and calcium ion could be stronger than that between the O2h or O2e groups and the calcium ion. Due to the strong interaction between Ca^{2+} and polyguluronate, Ca^{2+} can also act as a transient cross-linker to enlarge the interaction of functional groups of polyguluronate. The representative model of Ca^{2+} ion solvated in polyguluronate matrix is given in Figure 3.51, Ca^{2+} ion was wrapped by seven oxygen atoms from two polyguluronate chains. Ca^{2+} ions were trapped within the chelation structure between polyguluronate that corresponded to a stable Ca^{2+}/ polyguluronate complex formation.
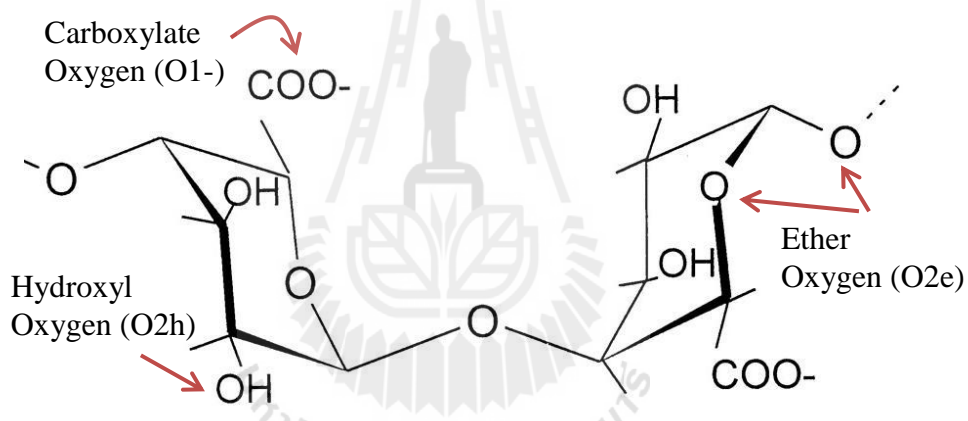
Figure 3.48 Atom labeling of Alginate (polyguluronate).
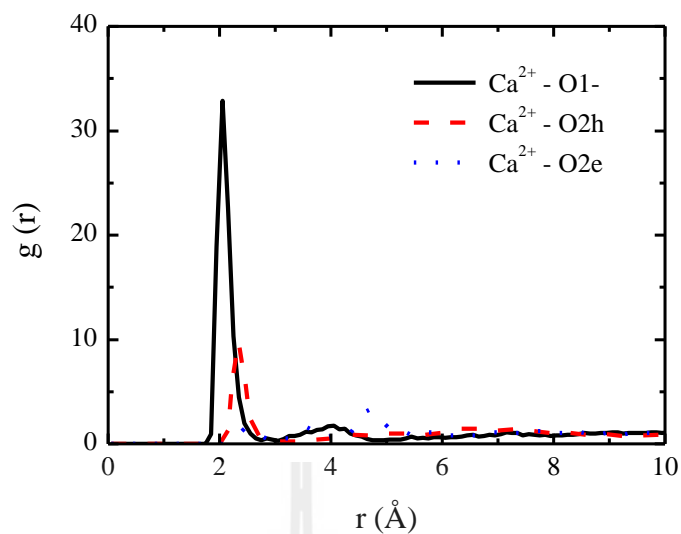
Figure 3.49 Radial distribution functions of Ca^{2+}/Polyguluronate.
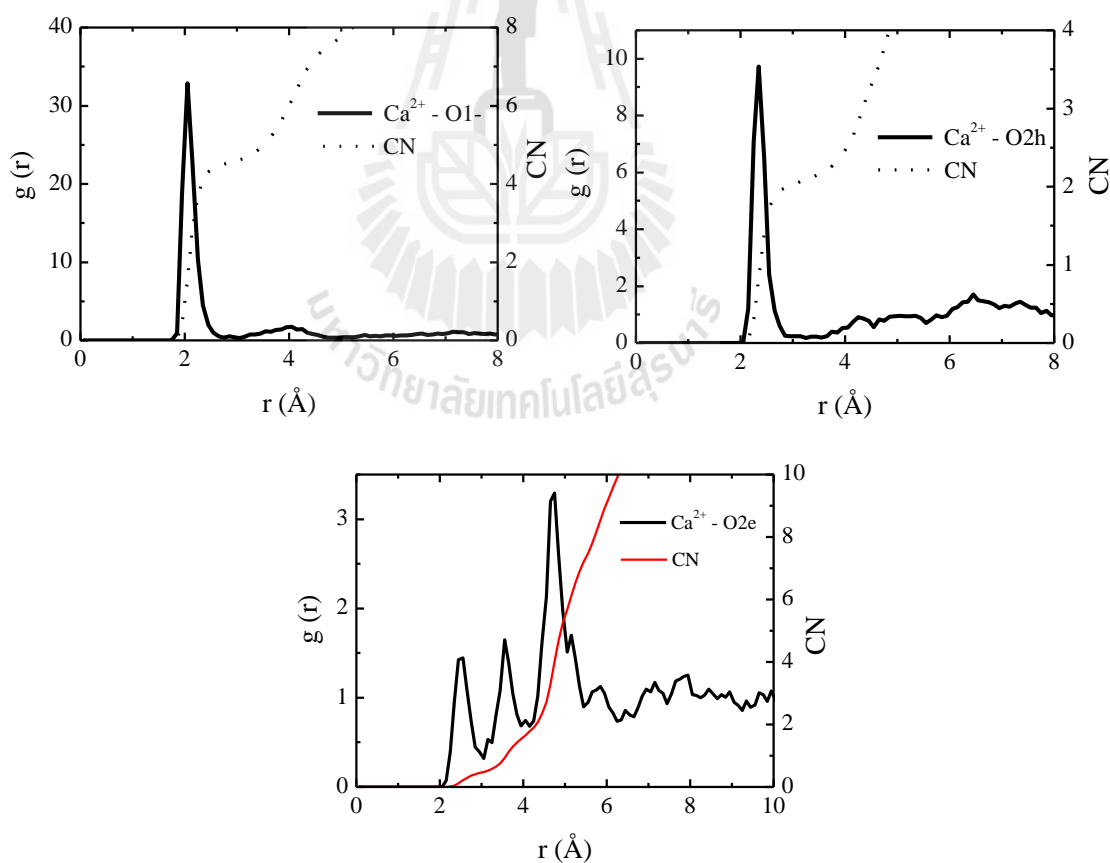
Figure 3.50 Radial distribution functions of Ca^{2+}/Polyguluronate, plotted separately.

Table 3.13 Parameter characterizing the first peak of RDF determined from MD at
298 K for Ca^{2+}/polyguluronate.

Atom Pair	R_0 (Å)	CN	limited of integration
Ca^{2+}- O1-	2.07	4.4	$0 \le R \le 2.55$
Ca^{2+}- O2h	2.35	1.9	$0 \le R \le 2.75$
Ca^{2+}- O2e	2.53	0.5	$0 \le R \le 3.05$
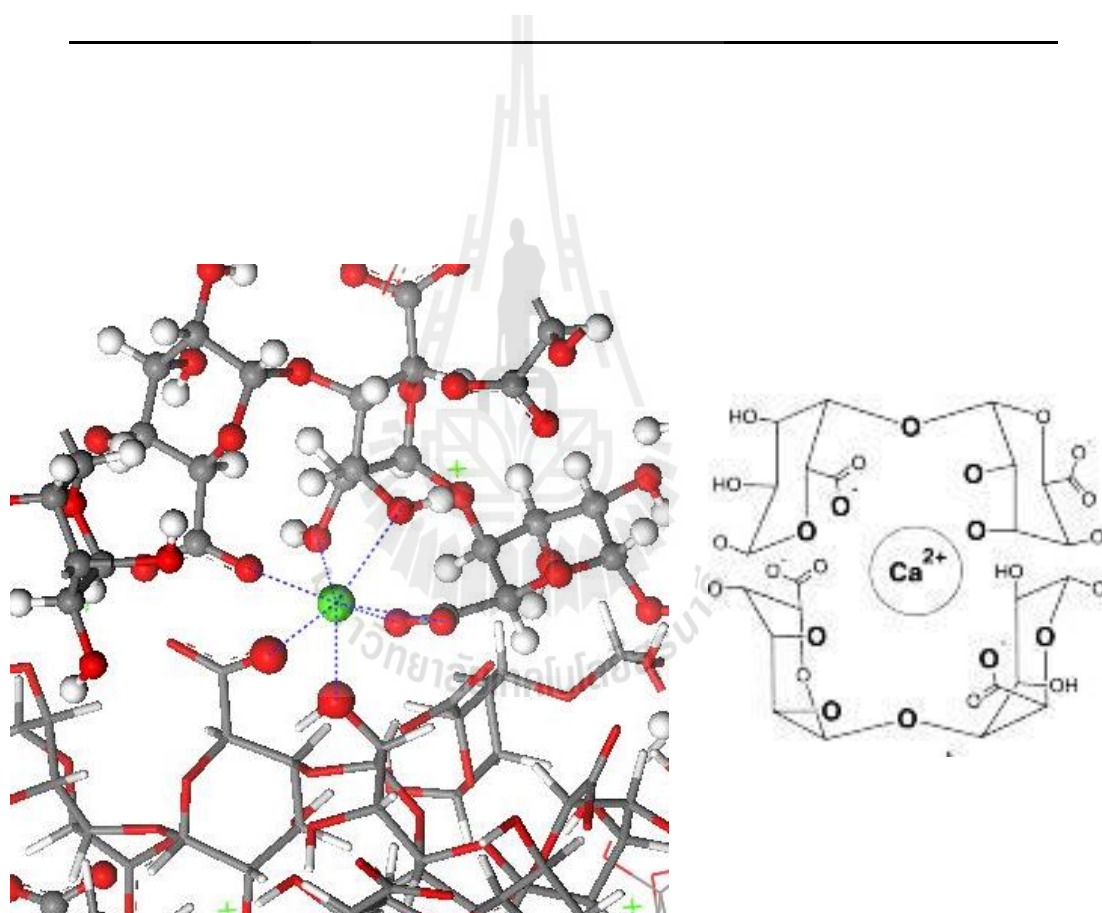
Figure 3.51 Schematics show that how Ca^{2+} ions are coordinated by polyguluronate.
(Colors: calcium cations–green, oxygen atoms–red, carbon atom–gray,
and hydrogen atoms–white).

3.6.4.2   MD-EXAFS

A comparison of k^2-weighted EXAFS spectra of $CaCl_2$/polyguluronate sample between an experiment and MD simulation are presented in Figure 3.52. The curves are in good agreement for frequency and fair agreement for the amplitude of the oscillations over the k range from 2 to 10 Å^{-1}, it is evident that the peak position is consistent between experimental and MD-EXAFS spectra. The $|\chi(R)|$ from both experiment and simulation are compared in Figure 3.53. The $|\chi(R)|$ was generated by Fourier transform of the $k^2\chi(k)$ data. There is little or no evidence of Ca-C scattering from $-CH_2-$ or $-CH_3$ in the experiment that means there is a large amount of position disorder for Ca-C distance. For the comparison of $|\chi(R)|$ EXAFS spectra between experimental and MD simulation, the first peaks of both spectra as shown in Figure 3.53 are in good agreement. That means the radial structures in the first solvation shell of the experimental data are nearly the same with MD results. Debye-Waller factors (σ^2) reflect the structural disorder of the system. The Debye-Waller factors determined from simulation ($\sigma_G^2 = 0.0112$ Å^2) is smaller than those determined form analysis of EXAFS measurements ($\sigma_i^2 = 0.0118$ Å^2). Indicate that the structural disorder of experimental data is more than those of the simulation data. Again, there is a remarkably good agreement between the radial structures of experimental and simulated data.
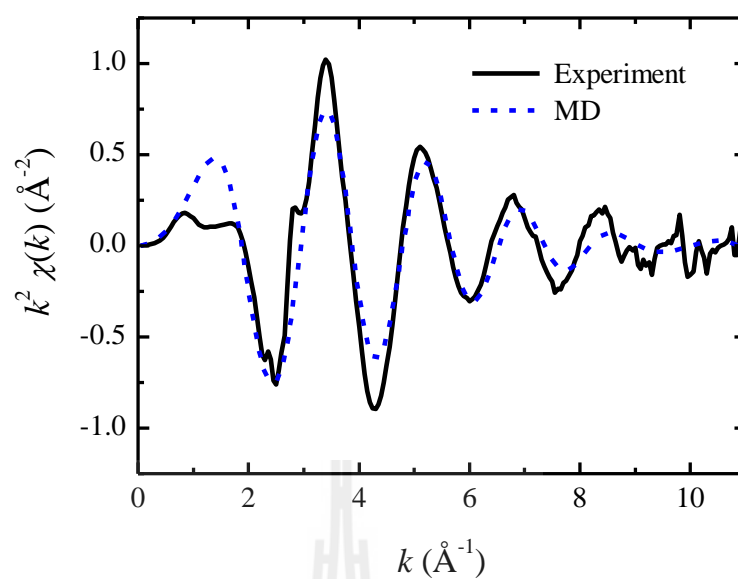
Figure 3.52 Comparison of calcium EXAFS k^2-weighted $\chi(k)$ plots for Ca^{2+}/Polyguluronate from experiment and MD simulation.
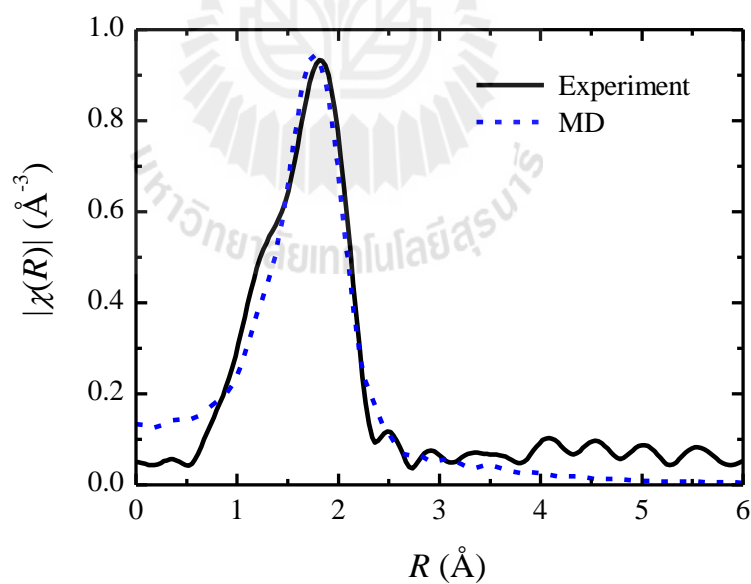
Figure 3.53 The $|\chi(R)|$ plots corresponding to the Fourier transformed $k^2\chi(k)$ as shown in Figure 3.52.

3.7 Conclusion

Molecular Dynamics simulation and the Extended X-ray Absorption Fine Structure (EXAFS) spectroscopy were employed to study the atomistic solvation structure of calcium ion in water, ethanol, isopropanol, poly(vinyl alcohol), Poly(acylic acid), pectin, and alginate. The simulated and Experimental EXAFS spectra were directly compared and were in good agreement. Ca^{2+}–Cl^- contact ion pairing has also been examined. The MD result indicated that the first coordination shell of Ca^{2+} (at distance ≤ 2.75 Å) in the water, ethanol, isopropanol, PVA, and PAA includes only oxygen atoms without chloride ion. The experimental EXAFS result indicated that, for dilute composition (with Ca^{2+}:O ratio = 1:50, 1:25, and 1:17) there is no contact Ca^{2+}– Cl^- pair and the ion environment is nearly independent of salt concentration. The complexation of Ca^{2+} ion with oxygen is a short range interaction and influences only the local structures of PVA and PAA chain.

For the calcium ion in Pectin and Alginate, the result is shown that the carboxylate oxygen, hydroxyl oxygen, and ether oxygen are located within the first shell of the Ca^{2+} ion ($r \leq 2.75$ Å). The interaction between the carboxylate oxygen and calcium ion is stronger than that between the hydroxyl oxygen or ether oxygen and the calcium ion. Due to the strong interaction between Ca^{2+} and polymer, Ca^{2+} can act as a transient cross-linker to enlarge the interaction of functional groups of polymer. Ca^{2+} ion was wrapped mostly by seven oxygen atoms from two polymer chains. Ca^{2+} ions were trapped within the chelation structure between polymer that corresponded to a stable Ca^{2+}/polymer complex formation.

CHAPTER IV

# PREPARATION AND CHARACTERIZATION OF

POLY(VINYL ALCOHOL)/POLY(ACRYLIC ACID)

HYDROGEL

4.1 Abstract

In this work, hydrogel films based on poly(vinyl alcohol), PVA, and poly(acrylic acid), PAA, blend, with various polymer composition were prepared and investigated. Attenuated total reflectance-Fourier transform infrared (ATR FT-IR) spectroscopy, swelling properties, rheological properties, and glass transition temperature of the films were employed to study the structure and their properties of this hydrogel. Differential scanning calorimeter (DSC) of the blends films showed only a single glass transition temperature (Tg) for each sample, indicating good miscibility between PAA and PVA. FT-IR spectra analysis showed that new interaction hydrogen bonds between PVA and PAA were formed. Swelling property of the films in pH = 7.4 buffer solution was also studied. The swelling ratio was increased with increasing PAA content in the blended films, and it was decreased with increasing PVA content. The rheological behavior of PAA/PVA gel systems (the elastic storage modulus G' and the viscous loss modulus G'') exhibited the typical gel-type mechanical spectra ($G' > G''$) in the entire frequency range examined, and there is little frequency dependence of the moduli.

4.2 Introduction

Hydrogel are polymeric networks which can absorb a large amount of solvent in the aqueous medium and swell without being dissolved. PVA and PAA are hydrophilic polymers that have been used in many biomedical researches as the active hydrogels. There are several ways to crosslink PVA, such as gamma radiation (Shin, Kim, and Lee, 1997), chemical crosslinking agents (Basiuk *et al.*, 2009), and heat treatment (Vázquez-Torres, Cauich-Rodríguez, and Cruz-Ramos, 1993). Preparing polymer blends is another useful method of simply controlling the hydrogel behavior. Crosslinking PVA/PAA blends by heat treatment leads to the stable hydrogels that can be used to deliver drugs such as insulin indentured through acidic media of stomach (Vázquez-Torres, Cauich-Rodríguez, and Cruz-Ramos, 1993). In this work we used these two polymers with different composition to prepare of PVA/PAA hydrogel blended films in order to have stable materials by heat treatment.

4.3 Experimental Details

4.3.1 Sample Preparation

Preparation of PVA/PAA blends films; PVA (98% hydrolyzed, Weight-average molecular weight Mw ~125,000 g/mol; manufacture's data) and Poly(acrylic acid) solution 35%(wt) in H_2O, MW = 100,000 g/mol, from Aldrich were used without further purification. Distilled, deionized water was use throughout.

PVA was dissolved in distilled, deionized water at 100°C for 3 hours to obtain the homogeneous PVA solution. After the solution was cooled down to room temperature, PAA aqueous solution was added (according to the desired ratio; 0.25, 0.33, 0.50, and 1.0 mol ratio of nOH/nCOOH). PVA/PAA mixture solutions were

stirred overnight at room temperature to achieve complete dissolution, then the solution was transferred to plastic plates and allowed to dry and solidity at an atmosphere condition in a dust free chamber and then the resulting dried films were cut into a small film size 1.5 cm. × 2.5 cm. and then dried in vacuum oven at 70°C for 24 h. In order to have the gel crosslink, thermal treatment was performed at 130°C for 20 min (Manavi-Tehrani, Rabiee, Parviz, Tahriri, and Fahimi, 2010), after that the blends films were kept in zipper plastic bag and stored in desiccators until future use.

4.3.2 Sample Characterization

Thermal Characterization: DSC (differential scanning calorimetry) was measured on Seiko Instruments Inc., DSC6220. About 5 mg of dried film samples were scanned from 40 to 250°C at a heating rate of 10°C/min under N_2 flow.

ATR-FTIR studies: Attenuated total reflectance-Fourier transform infrared spectroscopy (ATR-FTIR) was performed at Synchrotron Light Research Institute (SLRI) of Thailand on a Bruker Vertex 70 FT-IR spectrometer, and the spectra were signal averaged over 128 scans at a resolution of 4 cm^{-1} in a measurement rage of 4000 to 600 cm^{-1}.

Rheological measurement: Rheological measurements were performed at Kyushu university, Japan, on a rheometer (Anton Parr MCR300 rheometer) using 8 mm diameter (ϕ) parallel plates. The frequency sweep measurements are carried out at 30°C.

Swelling Studies: Swelling behavior of this polymer gel films in phosphate-buffered solution (pH 7.4) were evaluated. Dried polymer films were weighed and then immersed in the buffer solution (for 48 h to reach the swelling equilibrium) at

30°C. Then the free liquid on the surface of the swellen films was removed quickly with filter paper, and the weights of the samples were measured again. The swelling ratio was calculated by the following equation:

$$\% \, water \, uptake = \frac{W_{swell} - W_{dry}}{W_{dry}} \times 100\% \qquad (4.1)$$

where W_{swell} is the weight of swollen samples and W_{dry} is the weight of dried sample.

4.4   Results and Discussions

4.4.1   Thermal Property

From the glass transition (Tg) measurement, only a single (Tg) for all PVA/PAA films was observed (Figure 4.2). Indicating that the PVA/PAA films have an excellent miscibility in the blends they have formed. For this PVA/PAA blend, there is a strong interaction existing between the two polymers. The possible interaction may be hydrogen bonding between PVA and PAA component which would be later proved by using FT-IR in next section.
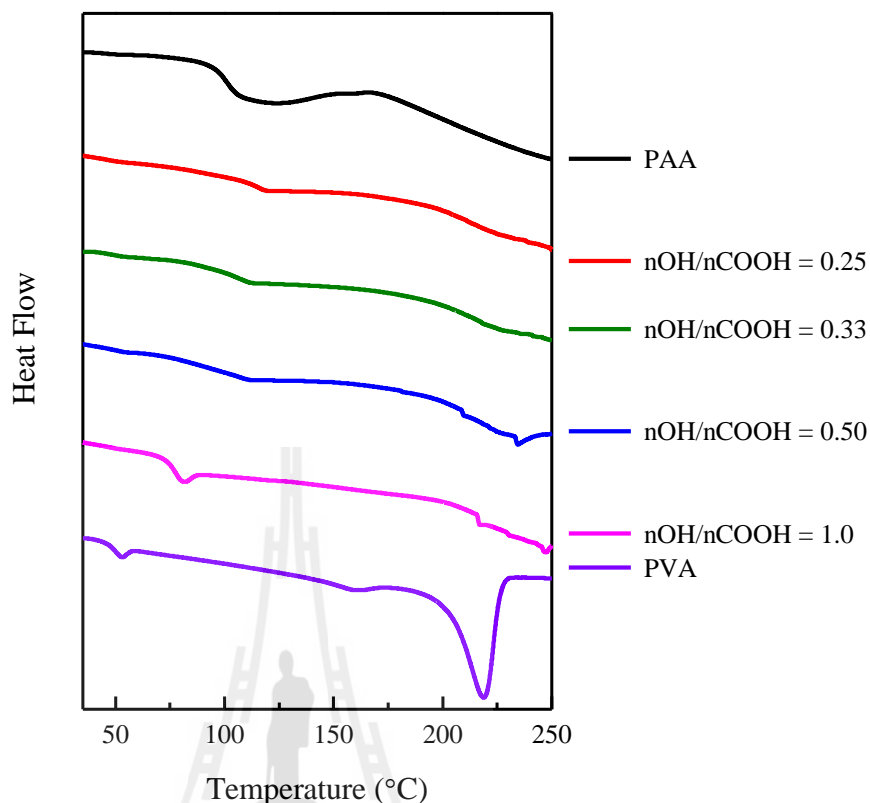
Figure 4.1 DSC curves of PAA, PVA, and PVA/PAA blends.

4.4.2 Interaction Between PVA and PAA in Blend Films

Figure 4.2 shows the ATR-IR spectra of the PVA/PAA films, several differences are apparent with different blended composition. The peak of O-H stretching vibration at 3280 cm^{-1} from neat PVA films, when compared with that of the blends, was gradually shifted to higher wave number, weakened intensity, and broadened with increasing PAA content in the blends. The wave number of the peak from 3280 cm^{-1} for neat PVA shifted to higher wave number when complex with PAA. This peak (O-H stretching vibration), was broaden and weaken and almost overlap with the broad peak of 3500–2400 cm^{-1} of COOH with an increase of PAA content, and then it was not evident at nOH/nCOOH = 0.5. These results suggest that

there is the replacement of the hydrogen bonding interaction among PVA chains and gradually replaced by the hydrogen bonding between PVA and PAA chains as the increased PAA content.

Moreover, the peak of O-H stretching vibration for the neat PVA at 3280 cm^{-1}, was broadened and weakened, while the C-O stretching vibration at 1089 cm^{-1} was slightly strengthened. This may be caused by the esterification reaction between carboxylic acid groups in PAA and hydroxyl groups in PVA.
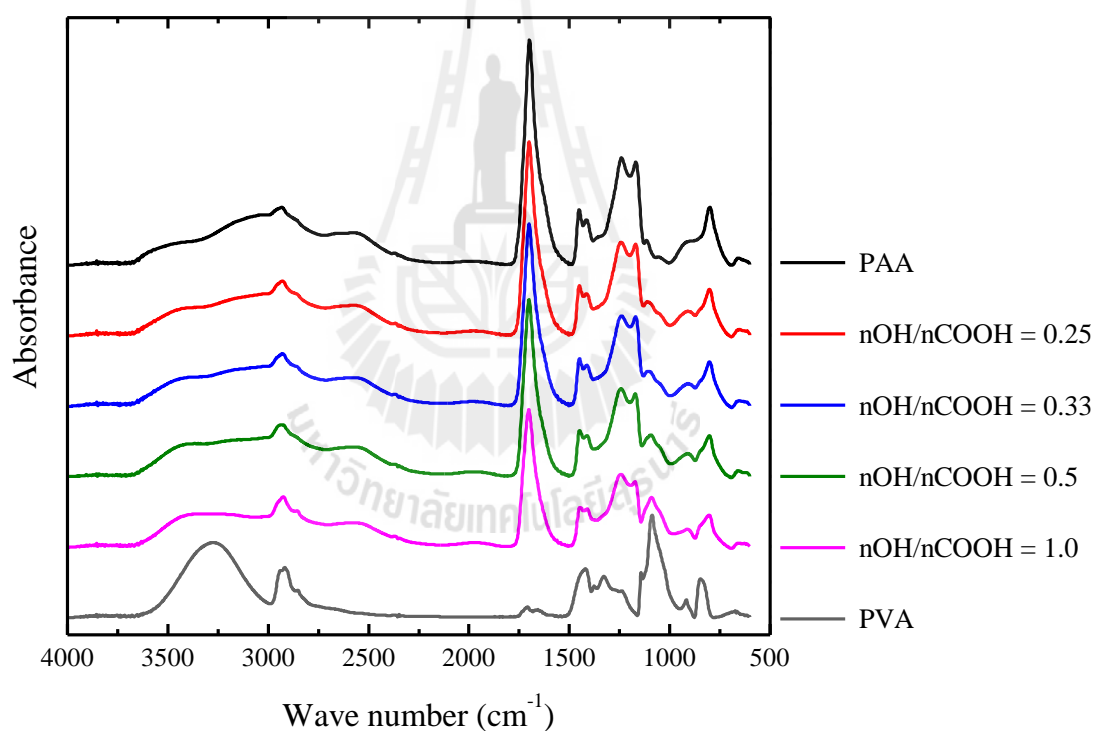
Figure 4.2 ATR-FTIR spectra of PAA, PVA, and PVA/PAA blends.

4.4.3 Rheological Properties

Mechanically, a gel is a soft material, having both solid and liquid-like characteristics (Clark and Ross-Murphy, 1987; Almdal *et al*., 1993). The application of oscillating small strains to the material allows us to obtain two dynamic moduli, namely, the storage modulus, (G'), a measure of the elasticity, and the loss modulus, (G''), representing the viscous component, at a given frequency of oscillation (Rao and Steffe, 1992; Ross-Merphy, 1994). A gel should exhibit a solid-like mechanical spectrum; that is, $G' > G''$ throughout the experimentally accessible frequency range and there is little frequency dependence of the moduli (Clark and Ross-Murphy, 1987; Almdal *et al*., 1993).

The rheological behavior of PVA/PAA gel systems (elastic modulus G', viscous modulus G'' presented in Figure 4.3. All samples exhibited the typical gel-type mechanical spectra; i.e., $G' > G''$ for the entire frequency range examined, and there is little frequency dependence of the moduli. These data support that PVA-PAA crosslink can occur in this polymer blend. Figure 4.4 shows that the G' is increased with increasing PVA content. It is indicated that PVA can cause this hydrogel to have more solid-like behavior.
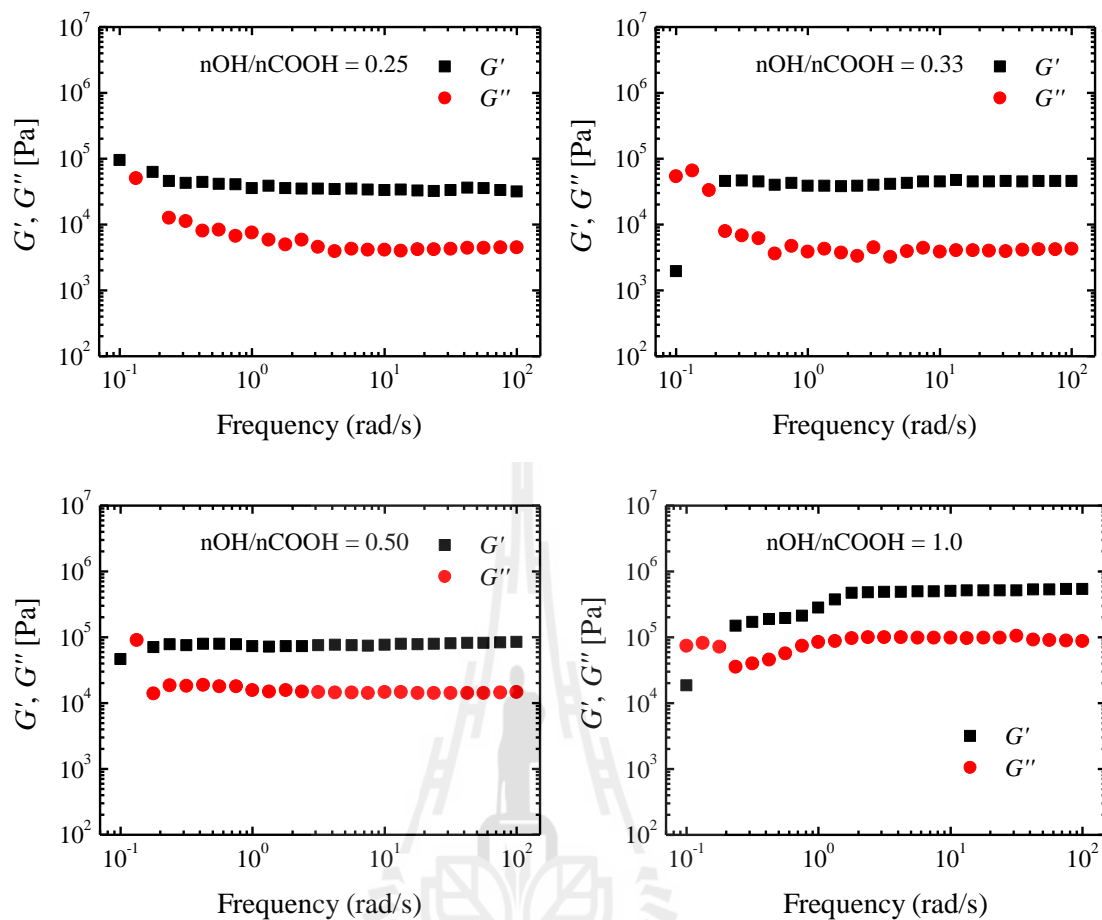
Figure 4.3 Frequency dependence of G' and G'' of PVA/PAA hydrogels.
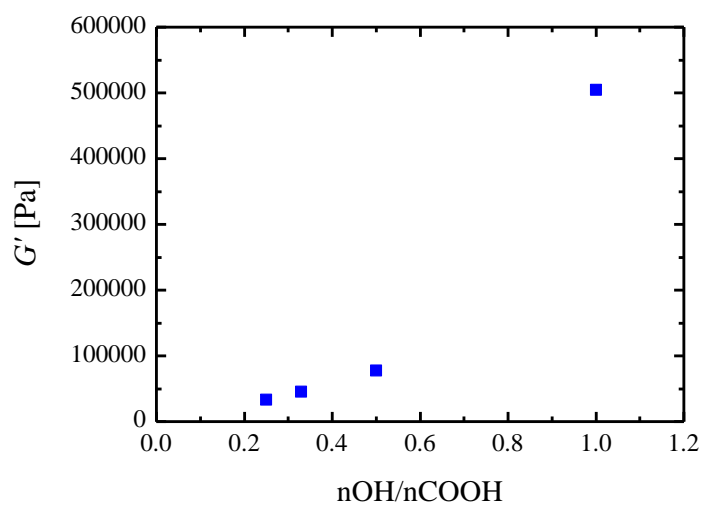
Figure 4.4 G' of PVA/PAA hydrogels as a function of PVA content (nOH/nCOOH).

4.4.4   Swelling Behavior

Figure 4.5 and 4.6 present the swelling behavior of thermally crosslinked PVA/PAA hydrogels in buffer solution (pH = 7.4). Figure 4.5 confirms that all hydrogel samples reached the equilibrium after about 12 h.

As can be seen from Figure 4.6, the swelling ratio in buffer solution pH = 7.4 is increased with increasing PAA content for PVA/PAA hydrogel, is should be noted that adding PAA to the mixture enhance the mixture to be more hydrophilic. Because of the carboxylic acid groups, the swelling behavior of the PVA/PAA hydrogel was highly dependent on the pH of the surrounding medium. Because the pKa of PAA was 4.75, so at pH = 7.4 phosphate buffer solution, the PAA carboxyl groups should be in the ionized form. Thus, the ionic repulsion caused by the formation of carboxylation allowed the hydrogel to swell.

Having more PAA content in this PVA/PAA hydrogel can cause a higher swelling ratio in pH = 7.4 phosphate buffer solution. Meanwhile, we can also observb that the swelling ratio was decreased with an increasing PVA content. This was because the reaction between OH and COOH groups to form the ester bonds that caused the number of hydrophilic COOH groups was lower, while the number of nodes of the networks was increased.
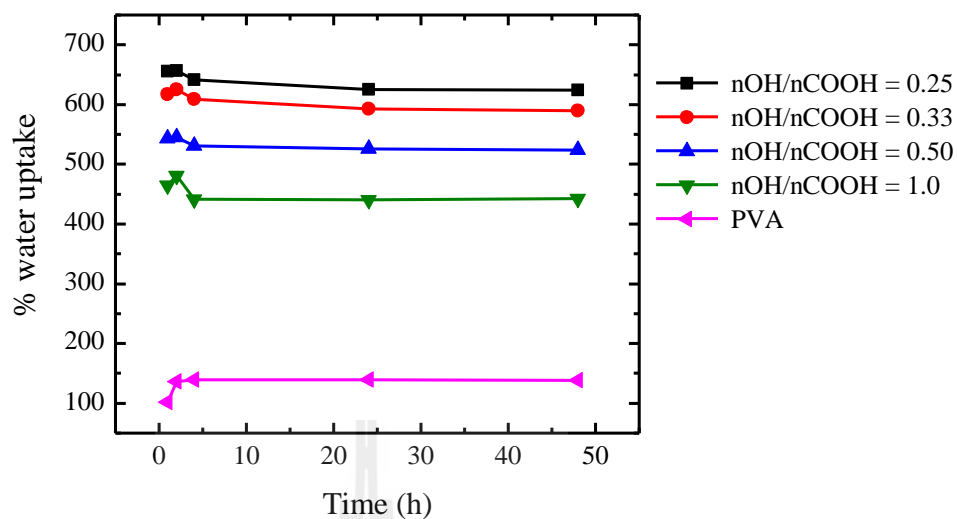
Figure 4.5 Swelling behavior of PVA/PAA hydrogels for the various PVA contents, as a function of time.
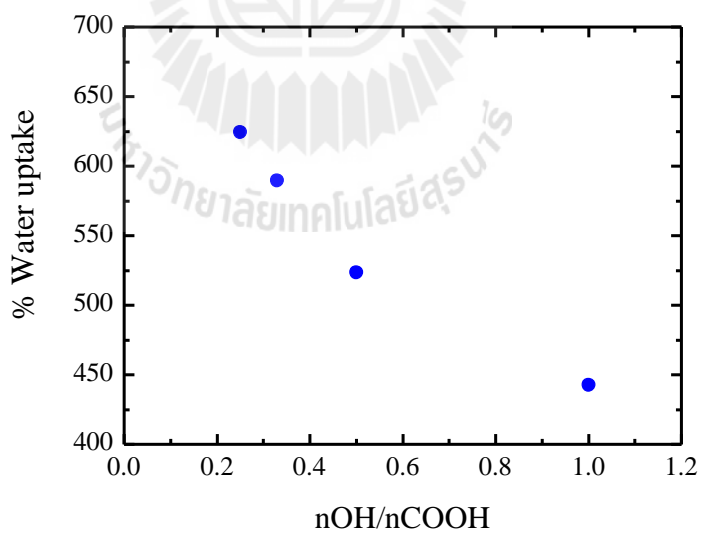
Figure 4.6 Swelling behavior of PVA/PAA hydrogels as a function of PVA contents.

4.5 Conclusion

In this work, PVA/PAA hydrogels were prepared through thermal crosslinking condition. The miscibility of PVA/PAA was confirmed by DSC. The DSC of the blended films showed only a single glass transition temperature (Tg) for each sample, indicating the good miscibility between PAA and PVA. FTIR spectra analysis suggests that there are interaction i.e. hydrogen bonds and ester bonds forming in PVA/PAA blends system. PVA/PAA hydrogels exhibit a solid-like mechanical spectrum; that is, $G' > G''$ throughout the experimentally accessible frequency range. These data support that PVA-PAA crosslink can occur in this polymer blend system. The G' was increased with an increasing PVA content. This indicates that PVA can cause these hydrogels to have more solid-like characteristics. Swelling properties of the films showed that the swelling ratio was decreased with increasing PVA content. This was because the interaction between OH and COOH to form ester bonds, this ester bonds was decreased the number of hydrophilic (COOH) groups and increased the number of nodes of networks.

CHAPTER V

MONTE CARLO SIMULATION STUDIES OF LINEAR

AND CYCLIC POLY(ETHYLENE OXIDE) IN THE

MELT STATE

5.1 Abstract

A coarse-grained Monte Carlo algorithm on a modified diamond lattice has been used to study the statics and dynamics properties of cyclic poly(ethylene oxide) molecules and linear poly(ethylene oxide) chains in the melt state. The simulations were performed at 373 K for the chain length from 25 to 200 repeating units. Three series of systems are studied in the simulation. Series I, studies the properties of the pure cyclic PEO molecules. Series II, studies the dependence of the statics and dynamics properties of cyclic and linear PEO on the mass fraction of the linear molecules, X_L. Series III, investigates the dependence of the statics and dynamics properties of cyclic PEO on the size of the cyclic matrix, N_C, and size of linear matrix, N_L.

Series I, the result suggests that the linear PEO are almost twice the size of the cyclic PEO. The diffusion coefficients of cyclic chains were higher than linear chains at high molecular weight. At the same molecular size (same $\langle R_g^2 \rangle$ value) the diffusion of linear chains is always larger than the cyclic molecules. Series II, for the blend of cyclic/linear chains, the sizes of linear and cyclic polymers are independent of the

blend composition. The diffusion coefficient of both cyclic and linear decrease as the linear fraction increases. Series III, diffusion coefficient of C-C is larger than C-L. The molecular topology can have an effect on the diffusion of cyclic polymers. Because of circular molecules are more compact than linear molecules.

5.2 Introduction

In the current report, our goal is to study the properties of cyclic and linear PEO systems. We employ MC simulations along with Metropolis rules (Metropolis *et al.*, 1953) for a pure cyclic PEO, pure linear PEO and their blends in the melt state. The simulation temperature is at 373 K, which is well above the melting temperature of the PEO chains (Tm of PEO is about 353 K). Poly(ethylene oxide) PEO was chosen as the subject of these study for variety of reason. (1) Linear POE has low entanglement molecular weight (Me ~ 2 kg/mol) and critical molecular weight for entanglement (Mc ~ 5.87 kg/mol), which means that unentangled and entangled regimes can be studied without simulated high-MW molecules with large box size that cause time consuming. (2) PEO structure is not too complicated for mapping in to coarse-grained beads and (3) the melt dynamics of cyclic POE or its blends with linear had not yet been reported.

5.3 Computational Details

5.3.1 Model

The MC simulations were performed on a high coordination lattice using coarse-grained PEO chains. Schematically, the mapping from a realistic chain to the coarse-grained chain is illustrated in Figure 5.1. In this simulation for PEO chains,

which have (CH$_2$-CH$_2$-O) repeat units, either one of CH$_2$ groups is represented as a single united atom as well as O atoms. In Figure 5.1, every second bead on the main chain, regardless of C or O, is taken out, and the remainder of united atoms is connected. In this particular kind of coarse-graining approach, every single bead has to be treated identically. There is no difference between C-O or C-C contacts in terms of the long-range (LR) interactions, but there exist a bit of ambiguity regarding the short-range (SR) interactions about which details are given in the next sections.

Fully Atomistic Representation

Exclusion of Hydrogen Atoms

Missing Atom

Coarse-Grained PEO Chain
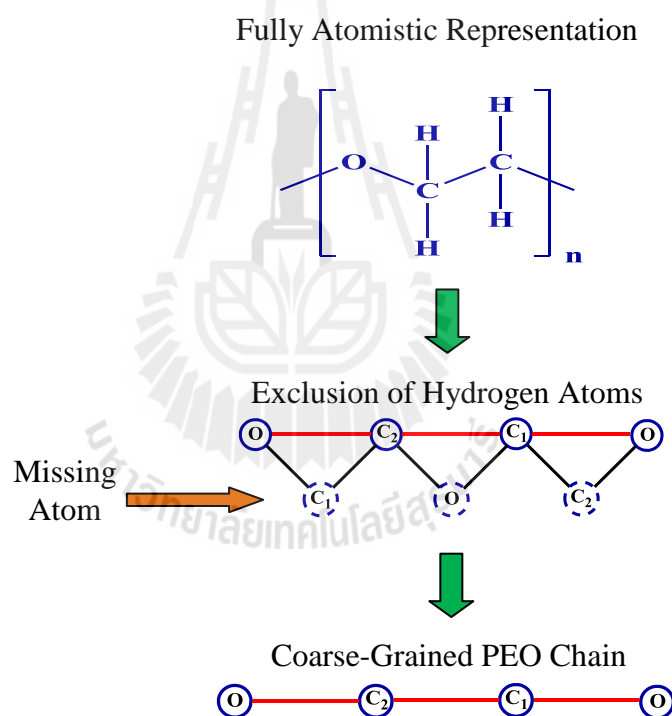
Figure 5.1 Example of the mapping of a real chain into lattice by coarse graining.

As shown in Figure 5.2, the 2nnd lattice can be considered as a distorted cubic lattice with 60° angle between any two axes. Because of that, each lattice site of the 2nnd lattice can be assigned with integer numbers, which expedites the RIS

calculations of interest. By its geometry, the 2nnd bond length (or step length) can also be calculated. The 2nnd lattice spacing, or step length, for a coarse-grained PEO chain is 2.39 Å. When the melt density of PEO is satisfied at the simulation temperature (373 K), the 2nnd lattice has an occupancy value of 20%. It should be noted that, most of the simulations presented in this work are done for dense melt systems.
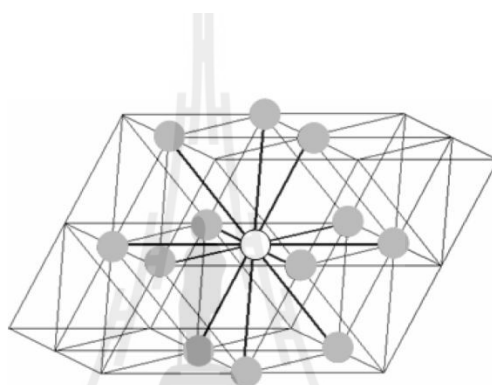
Figure 5.2 The 2nnd lattice. The gray spheres represent the possible twelve coordination lattice sites around the central bead (open circle).

5.3.2 Energy

5.2.2.1 Short-range Interaction

The short-range (SR) interactions basically enforce the local conformational preferences of the polymer chains. As emphasized before, the reproduction of realistic polymer chains on the 2nnd lattice necessitates the use of realistic interaction potentials. Compared to a simple random walk case, torsion potential energy functions for real chains are definitely far more complex. In this report, short range interactions are represented by a model based on the Rotational Isomeric State (RIS) model.

The RIS model (Flory, 1988; Mattice and Suter, 1994) is very good at describing the conformational properties of the chain molecules. Therefore, Abe *et al.* calculated configuration-dependent properties of PEO chains by means of RIS calculations (Abe, Tasaki, and Mark, 1985). These calculations are based on a symmetric three-fold torsion potential with nearest neighbor interdependence. Along the main backbone of a PEO chain one can find three different types of bonds: *C-C*, *C-O*, and *O-C*. Thereby, each torsion potential in their RIS model representation is peculiar in the sense that each of them belongs to a certain bond family.

The RIS model is known to work properly to reveal the local characteristics of polymer chains. In addition, the diamond lattice is also considered a good candidate for on-lattice polymer simulations. Thus, the RIS approximation should be considered a good way to model PEO chains on the diamond lattice. However, in order to describe the short-range interactions on the 2nnd lattice properly, a mapping procedure, which will define the torsion angles in the real chains on the 2nnd lattice, is needed.
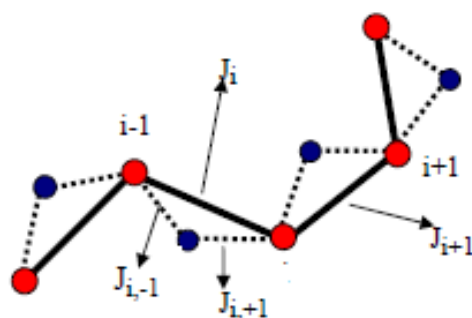
Figure 5.3 Schematic representation of 2nnd sub-chain composed of 4 coarse-grained bonds (solid lines). The dashed lines denote the corresponding real bonds on the underlying diamond lattice.

There are three available rotational isomeric states, which are *trans* (*t*), *gauche*$^+$ (*g*$^+$), and *gauche*$^-$ (*g*$^+$) for every single bond on the diamond lattice. As shown in Figure 5.3, for a 9-atom polymer sub-chain there are 8 bonds on the tetrahedral lattice. With further coarse-graining, i.e. after switching to the 2nnd lattice, half of the bonds on the diamond lattice will disappear and there will be only four 2nnd bonds left. Although half of the diamond lattice bonds disappear on the 2nnd lattice, we still keep track of their information at every single step throughout the MC simulations.

The RIS calculations are based on the probabilities of the rotational isomeric states of pairs of bonds on the main backbone. By combining the probabilities of the entire amount of rotational isomeric states, the probability of a certain multi-chain system can be calculated. As described in the previous paragraph, there exists an independent rotational isomeric state associated with each single bond. Each bond may be represented by one of *t*, *g*$^+$, or *g*$^-$ states. On the 2nnd lattice however, there will be only a coarse-grained single bond, whose rotational isomeric state is defined by that of former two tetrahedral bonds. For example, if the two corresponding rotational isomeric states of the two diamond-lattice bonds are *g*$^+$ and *g*$^-$; then the resulting 2nnd bond's rotational isomeric state will be defined by a double rotational isomeric state representation like "*g*$^+$*g*$^-$" instead of a single representation. In that sense, every single rotational isomeric state on the 2nnd lattice may have triple more possibilities (*tt*, *tg*$^+$, *tg*$^-$, *g*$^+$*t*, *g*$^+$*g*$^+$, *g*$^+$*g*$^-$, *g*$^-$*t*, *g*$^-$*g*$^+$, *g*$^-$*g*$^-$) when the torsions on the underlying diamond lattice are considered. The probability of a specific multi-chain system can be calculated in this way with the aid of the mapping technique. In

particular, a more detailed explanation of this mapping technique for polymer chains with (A-A-B) type of repeat unit, e.g. PEO, can be found.

Next, we present the related statistical weight matrices that determine the local conformation of the PEO chains used in the MC simulations (Doruker, Rapold, and Mattice, 1996). In the following three matrices (U_{C-C}, U_{C-O}, U_{O-C}), the rotational isomeric states of bonds $J_{i,-1}$ and $J_{i,+1}$ are represented by the rows and columns, respectively. There are three different statistical weight matrices, each representing a specific bond type. σ_{C-C} and σ_{O-O} are the statistical weights for the C-C and O-O type first-order interactions. ω_{C-C} and ω_{C-O} correspond to the second-order interactions. These numbers are calculated as the Boltzman factors (exp (-*E/RT*)) of the associated energy values listed in Table 5.1.

$$
U_{C-C} = \begin{array}{c} \\ t \\ g^+ \\ g^- \end{array} \begin{array}{ccc} t & g^+ & g^- \\ \left[\begin{array}{ccc} 1 & \sigma_{O-O} & \sigma_{O-O} \\ 1 & \sigma_{O-O} & \sigma_{O-O}\omega_{C-O} \\ 1 & \sigma_{O-O}\omega_{C-O} & \sigma_{O-O} \end{array} \right] \end{array} \tag{5.1}
$$

$$
U_{C-O} = \begin{array}{c} \\ t \\ g^+ \\ g^- \end{array} \begin{array}{ccc} t & g^+ & g^- \\ \left[\begin{array}{ccc} 1 & \sigma_{C-C} & \sigma_{C-C} \\ 1 & \sigma_{C-C} & \sigma_{C-C}\omega_{C-O} \\ 1 & \sigma_{C-C}\omega_{C-O} & \sigma_{C-C} \end{array} \right] \end{array} \tag{5.2}
$$

$$
U_{O-C} = \begin{array}{c} \\ t \\ g^+ \\ g^- \end{array} \begin{array}{ccc} t & g^+ & g^- \\ \left[\begin{array}{ccc} 1 & \sigma_{C-C} & \sigma_{C-C} \\ 1 & \sigma_{C-C} & \sigma_{C-C}\omega_{C-C} \\ 1 & \sigma_{C-C}\omega_{C-C} & \sigma_{C-C} \end{array} \right] \end{array} \tag{5.3}
$$

In summary, the rotational isomeric state of any 2nnd bond can be defined by those of its corresponding tetrahedral lattice bonds $J_{i,-1}$ and $J_{i,+1}$ For instance, if the 2nnd bond J_i in Figure 5.3 is a *C-C* type of a bond and the states of the real bonds $J_{i,-1}$ and $J_{i,+1}$ are g^+ and g^-, the resulting statistical weight of the 2nnd bond J_i will be equal to U_{C-C}, which is $\sigma_{O-O}\omega_{C-O}$. The values of the statistical weights σ_{O-O} and ω_{C-O} can be determined by substituting their related energy values, the simulation temperature, and the universal gas constant into the Boltzman factor. Obviously, the simulation temperature and the universal gas constant are pre-known parameters. So, the substitution of the true matrix element is the key point to the determination of the corresponding statistical weight of the bond J_i. Consequently, the same procedure is followed for all of the coarse-grained beads in the system. The combination of those leads to the configurational probability of the overall system.

Table 5.1   Fisrt- and Second-Order local interactions on the 2nnd lattice for PEO chains: RIS model approximation.

Interaction	(kJ/mol)
$E\sigma_{C-C}$	3.2
$E\sigma_{O-O}$	-2.2
$E\omega_{C-C}$	∞
$E\omega_{C-O}$	2.2

5.3.2.2 Long-range Interactions

The incorporation of the RIS model is not enough to describe the energetics of the melt system because the RIS model is a single chain model in the unperturbed state, (θ state). The model only accounts for the short-range intermolecular interaction up to next nearest neighbor bonds on the 2nnd lattice. For the remaining long-range intramolecular and intermolecular interaction, the Lennard-Jones pair potential, $u(r)$, seems to be a reasonable choice since there are only dispersive interactions in the PEO melt. Including the long-range interaction, the total energy which is used in Metropolis evaluation should be

$$E_{total} = E_{RIS} + E_{LJ} \tag{5.4}$$

The lattice representation of the continuous Lennard-Jones potential at the ith shell, u_i, is obtained from an averaged Mayer f-function which is used for the description of the second virtual coefficient of a non-ideal gas. The interaction parameter at the ith shell is defined through following equation.

$$\exp\left(-\frac{u_i}{k_B T}\right) - 1 \equiv \bar{f}_i \tag{5.5}$$

The average Mayer f-function at the ith shell, $\bar{f}_i$ is obtained by integrating $u(r)$ over the cells in the ith shell.

$$\bar{f}_i = \frac{\int_{cell} f \, dr}{\int_{cell} dr} \tag{5.6}$$

$$f = \exp\left(-\frac{u(r)}{k_B T}\right) - 1 \tag{5.7}$$

The set of the interaction parameters for 2nnd beads is derived from the Lennard-Jones potential for the methyl ether molecule (CH_3-O-CH_3). Table 5.2 gives a set of interaction parameters obtained by the averaging method. The detail about the long-range interaction is given by Cho and Mattice (1997). .

Table 5.2   Long-range interaction shell energy obtained from the averaging process.

Shell	Shell energy (kJ/mol)[a]
1	8.113
2	-0.213
3	-0.339
4	-0.067
5	-0.017

[a] In this example, the used LJ parameters are $\sigma = 3.76$ Å and $\varepsilon/k = 154$ K and the interaction shell energies are derived at 373 K.

The single bead move was always employed in this study with the restriction that a chain cannot pass through itself, as in a self-avoiding random walk. A randomly chosen bead can move to a vacant site in the first shell when the attempt

does not change the bond length to its two bonded neighbors. Even though the relaxation or equilibration of a system is quite slow with the single bead move, the move provides the reliable dynamic properties at the time scale of Monte Carlo step (MCS). One MCS is defined as the simulation length when every bead in the system has attempted one move, on average.

5.3.3   System Description

The simulations for studies the properties of cyclic and linear PEO are performed in a periodic box with 40 steps lengths (step length = 2.39 Å) on each side of the 2nnd lattice; i.e., Lx = Ly = Lz = 40. For all systems, simulations were conducted at 373 K (which is well above the melting temperature of the PEO chains (Tm of PEO is about 353 K)) with the density of 1.06 g/cm^3 (Orwoll, 1996), which was archived with an occupancy of 21% of the sites on the lattice. Three series of systems are studied in the simulation.

Series I: the properties of the pure cyclic PEO molecules and pure linear PEO chain. In this series, the sizes of the pure linear and pure cyclic molecules are 25, 50, 100, and 200 beads on the simulation box.

Series II: the dependence of the statics and dynamics properties of cyclic and linear PEO on the mass fraction of the linear molecules, X_L. In this series, the size of the linear and cyclic molecules are the same, (1) $N_C = N_L = 25$, (2) $N_C = N_L = 50$, (3) $N_C = N_L = 100$, and (4) $N_C = N_L = 200$. The mass fraction of the linear molecules, (X_L), varies from 0 to 1. The number of the linear and cyclic molecules changes with the X_L, but the total number of molecules in the system remains the same.

Series III: the dependence of the static and dynamic properties of cyclic PEO on the (1) size of the cyclic PEO matrix, (N_C), and (2) size of linear PEO matrix, (N_L). The mass fraction of cyclic, (Xc), remained at 0.5 for different N_C and N_L. The size of the probed cyclic molecules was 100 beads. The size of the matrix (N_C, N_L) changed from 25, 50, 100, and 200 beads.

For every system, the initial configuration contained cyclic molecules with the shape of a deformed rectangle, which were placed at different position, and the linear chains were randomly distributed in the periodic box. Since unphysical collapses can exist in the initial cyclic molecules, a short MC simulation was performed to remove this possible conformation. Next, a sufficiently long simulation was run until the system achieved the equilibrium. After equilibration, an additional 10 million Monte Carlo Steps (MCS) were performed to evaluate the properties of the cyclic PEO molecules and the linear PEO chains. The configurations were recorded every 10,000 MCS.

5.4 Results and Discussion for Pure Cyclic and Pure Linear PEO

5.4.1 Equilibration of the System

Equilibration of the systems can be determined by evaluating the mean-square displacement of the center-of-mass (MSD). The MSD is shown in Figure 5.4 for the pure cyclic and pure linear PEO system with chain length equal to 200 beads. This parameter is evaluated separately for the linear and cyclic molecules. When MSD reaches the mean-square radius of gyration, $\langle R_g^2 \rangle$, the molecules have translated away from their initial positions. From Figure 5.4, it is well-confirmed that the system can reach to equilibrium conditions at the early stages of simulations. The other systems

in this study showed similar results for MSD as shown in Figure 5.4. The MSD indicate that the movement of the chains equilibrates rapidly so 1,000,000 MCS were used for equilibration.
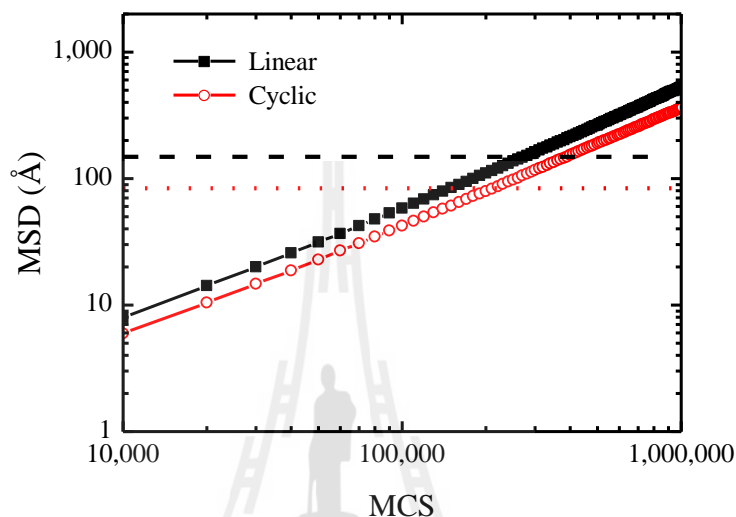
Figure 5.4   Mean-square displacement of the center-of-mass (MSD) of pure linear chains (square) and pure cyclic molecules (circle) as a function of Monte Carlo step (MCS) for the system with $N_C = N_L = 200$. The horizontal lines are the mean-square radius of gyration ($\langle R_g^2 \rangle$) of the linear chain (dashed line) and the cyclic molecule (dotted line).

5.4.2   Size of Pure Cyclic and Pure Linear PEO

The sizes of the cyclic and linear PEO were compared in terms of $\langle R_g^2 \rangle$ (Figures 5.5 and 5.6). Figure 5.5 shows that the relative size of linear/cyclic is $\langle R_g^2 \rangle_{linear}/$ $\langle R_g^2 \rangle_{cyclic} \approx 2$. The linear PEO are almost twice the size of the cyclic PEO, as expected for long random flight chains (Rubinshtein and Collby, 2003). The chain length dependence of radius of gyration for linear and cyclic chain can be described

by a scaling law as $\langle R_g^2 \rangle_{linear} \sim N^{1.037}$ and $\langle R_g^2 \rangle_{cyclic} \sim N^{0.969}$ as shown in Figure 5.6. The scaling law index of 1.04 and 0.97 are close to the recent results based on the bond-fluctuation MC simulation of 1.02 and 0.86 for linear and cyclic chains, respectively (Müller, Wittmer, and Cates, 1996). This result suggests that long cyclic chains in the condensed system have smaller dimensions than those of linear chains with the same molecular weight.
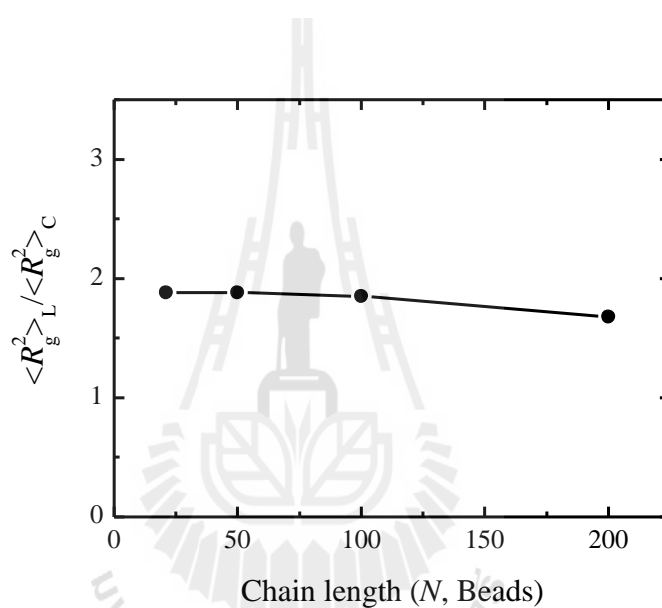
Figure 5.5 The ratio of the mean-square radius of gyration ($\langle R_g^2 \rangle$) of linear chains to cyclic molecules (same molecular weight) as a function of chain length (N, beads).

Figure 5.6 The mean-square radius of gyration ($\langle R_g^2 \rangle$) of linear chains (square) and cyclic molecules (circle) as a function of chain length (N, beads).

5.4.3. Motion of Pure Cyclic and Pure Linear PEO

The long time Einstein diffusion coefficients of all systems are shown in Figure 5.7 with respect to N, and in Figure 5.8 with respect to the radius of gyration. The crossover between the linear and cyclic diffusion coefficient (D) is clearly seen in Figure 5.7.

The lower diffusion coefficient (D) of the cyclic chains at low N (see Figure 5.7) can be explained by a combination of factors, mainly by the smaller size of the cyclic chains and the local density produced by segments from the same molecule. Because of the smaller size of cyclic PEO, the density of these segments inside the volume occupied by a cyclic PEO is higher than that of a linear PEO. At low N, linear chains with high amount of end beads move easier than the cyclic molecules and result in higher diffusion coefficient.

The higher diffusion coefficient (D) (see Figure 5.7) of cyclic PEO at high N may be due to the different manner in which entanglements affect linear and cyclic PEO when N is slightly higher than the entanglement length, for the linear chain. The linear chains are slowed down by the existence of entanglements. Contrarily, cyclic molecules do not experience entanglements at this N due to their smaller size, which isolates them from other neighboring molecules.

At high molecular weights, the size of chain may become more important as the entanglements dominate the dynamics of the linear chains. The smaller size of the cyclic molecules might result in less interpenetration between molecules, and therefore shields them from forming entanglements at the molecular weight where the linear chains do. As a result, the dynamics of the cyclic molecules remain unaffected, whereas the linear chains suffer from the entanglements effect.

Figure 5.8 shows that, there is no crossover in the radius of gyration, and therefore the behavior of the radius of gyration does not cause the crossover observed in diffusion coefficient (D). If a comparison is made for the chains with the same molecular size (same $\langle R_g^2 \rangle$ value) as shown in Figure 5.8, the diffusion of linear chains is always larger than the cyclic molecules. This is expected from an increase almost $2N$ for cyclic chain to have the same molecular size as the linear analog.
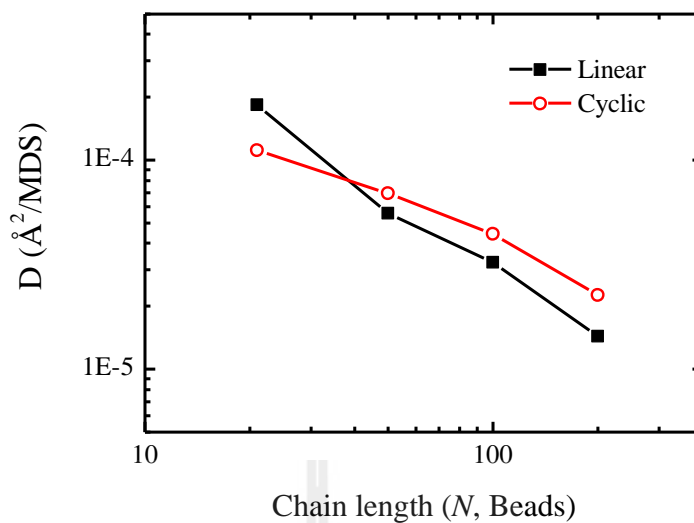
Figure 5.7 Diffusion coefficients of linear chains (square) and cyclic molecules (circle) as a function of chain length (N, beads).
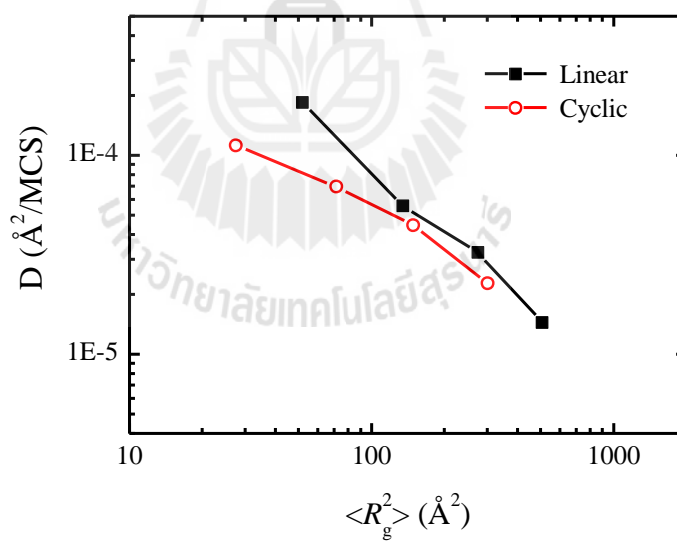
Figure 5.8 Diffusion coefficients of linear chains (square) and cyclic molecules (circle) as a function of mean-square radius of gyration, $\langle R_g^2 \rangle$.

4.5 Results and Discussion for Cyclic and Linear PEO in the Blends

The cyclic molecules and the linear chains are the same chemical species - $(CH_2\text{-}CH_2\text{-}O)$-. However, the cyclic molecules have the constraint that the head and tail beads are connected. This constraint may possibly influence the interactions of the system and cause some segregation to occur between the cyclic molecules and the linear chains. To verify that the system has not segregated, the intermolecular pair correlation function (PCF) is evaluated for the various systems included in the study. This function gives the probability of finding a particle A at a specified distance from another particle A defined by Equation (5.8) on the high coordination lattice (Xu and Mattice, 2002).

$$g_{AA}(i) = \frac{n_{AA}(i)}{(10_i^2 + 2)V_A} \tag{5.8}$$

In Equation (5.8), $n_{AA}(i)$ is the number occupancy of A in the ith shell from another A particle and V_A is the volume fraction of A in the entire system. The beads on the same chain are ignored in the evaluation of the intermolecular PCF.

For the system with $Xc = 0.5$, the intermolecular PCF as a function of shell number, which indicates the distance away from a given bead, is shown in Figure 5.9. Four PCFs are calculated. Two PCFs analyze similar pairs of molecules, such as linear-linear and cyclic-cyclic. The third one is for dissimilar pairs, linear-cyclic. Finally, the fourth, which is the total PCF, is for all pairs in the system. Although the values of the four PCFs in the second shell in Figure 5.9 are not the same, their differences do not exceed the sums of the standard deviations. This result indicates

that a linear chain (cyclic molecule) is equally likely to find a cyclic molecule (linear chain) nearby as opposed to a linear chain (cyclic molecule).

The sizes of the cyclic and linear PEO in the blends were compared in terms of $\langle R_g^2 \rangle$. For the blend of cyclic/linear chains, the size of linear and cyclic polymers is not sensitive to the composition as presented in Figure 5.10 for the system of $N = 100$ and Figure 5.11 for the system of $N = 200$. As expected, $\langle R_g^2 \rangle$ for the linear chains and the cyclic molecules are independent of X_L.

Figure 5.12 and Figure 5.13 show the variation of the diffusivity as a function of the fraction of linear chains for $N = 100$ and $N = 200$ respectively. As linear fraction increases, the diffusivities of both linear and cyclic (D_L and D_C) decrease, while D_C drops more sharply. These results support that the diffusion coefficients of cyclic polymers are extremely sensitive to linear contaminants. This finding is in accordance with recent results of an enhancement of the terminal relaxation time of a polystyrene cyclic-linear blend with 5 vol% of the linear component (McKenna and Plazek, 1986).
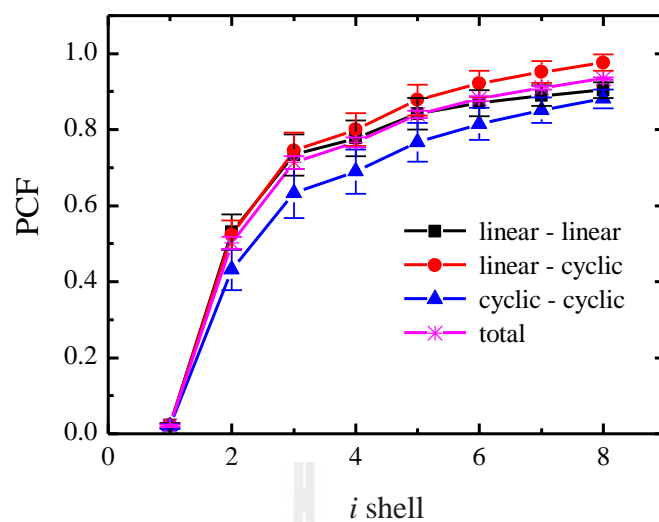
Figure 5.9 Intermolecular pair correlation functions (PCFs) as a function of shell number for the system with $Xc = 0.5$ and $N_C = N_L = 100$.

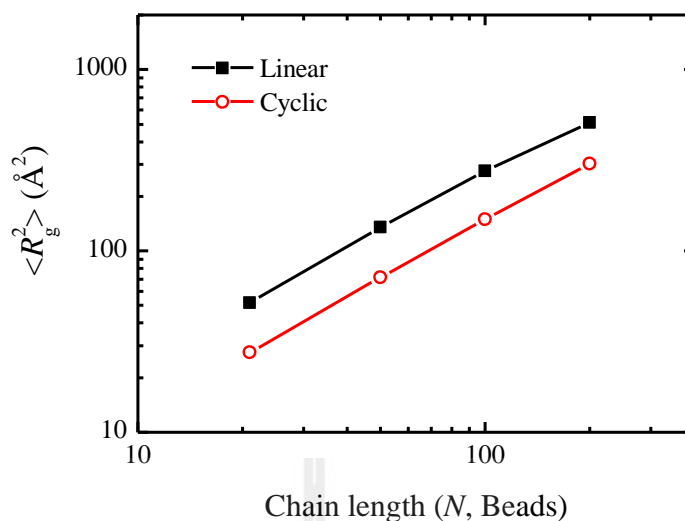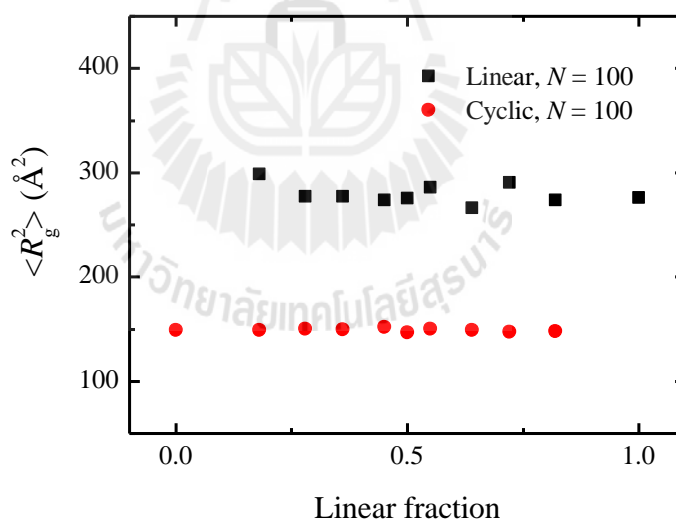**Figure 5.10** The mean-square radius of gyration, $\langle R_g^2 \rangle$, of linear chains (square) and cyclic molecules (circle) for $N_C = N_L = 100$ beads at different blend compositions.
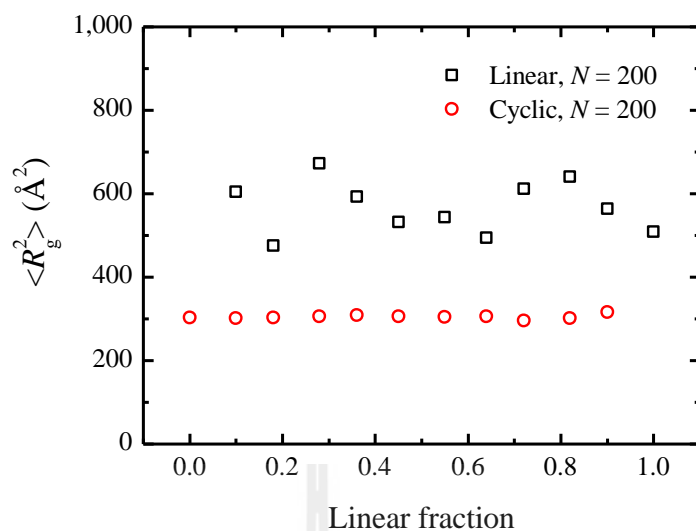
Figure 5.11 The mean-square radius of gyration, $\langle R_g^2 \rangle$, of linear chains (square) and cyclic molecules (circle) for $N_C = N_L = 200$ beads at different blend compositions.
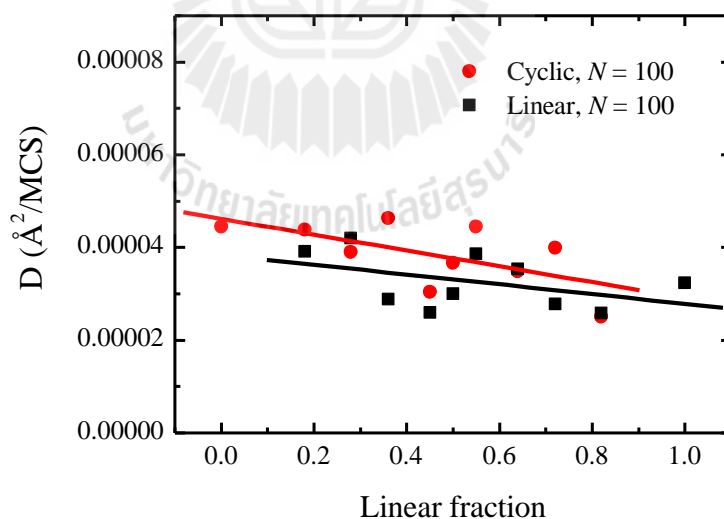
Figure 5.12 Diffusion coefficients of linear chains (square) and cyclic molecules (circle) for $N_C = N_L = 100$ beads at different blend compositions.
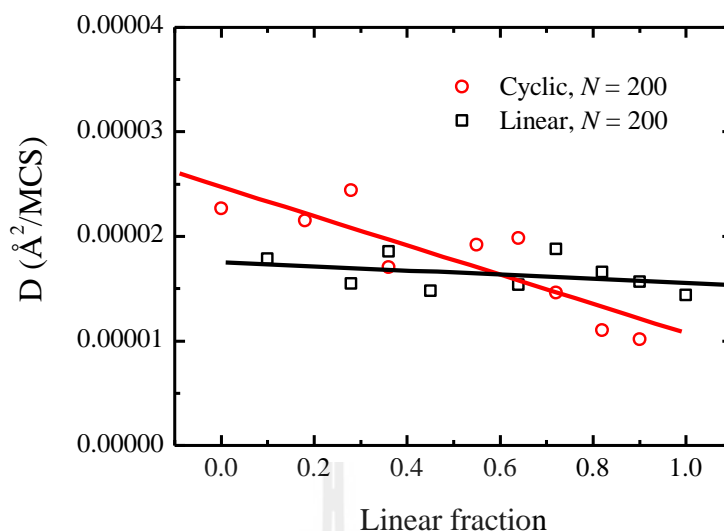
Figure 5.13 Diffusion coefficients of linear chains (square) and cyclic molecules (circle) for $N_C = N_L = 200$ beads at different blend compositions.

5.6 Results and Discussion for the Effect of Matrix Topology on the Properties of Cyclic PEO

Figure 5.14 is shown that the $\langle R_g^2 \rangle$ of cyclic molecules in linear matrix (C-L) is larger than $\langle R_g^2 \rangle$ of cyclic molecules in cyclic matrix (C-C), indicating that the size of the cyclic molecules in cyclic matrix are larger than the cyclic molecules in linear matrix. The $\langle R_g^2 \rangle$ of C-C and $\langle R_g^2 \rangle$ of C-L have more different when the chain length of the matrix is increased. Figure 5.15 shows that the diffusion coefficient (*D*) of C-C is larger than C-L. Because C-C have smaller size, lower local density, so it easier to move compare with cyclic in linear chain that threaded even may occur. The length dependences are shown in Figure 5.15. We find $D_{C-C} > D_{C-L}$ for all lengths. This behavior is similar to that found by NMR for the *C-C* and *C-L* mixture (Cosgrove, Griffiths, Hollingshurst, Richards, and Semlyen, 1992; Cosgrove *et al.*, 1996; von

Meerwall, Ozisik, Mattice, and Pfister, 2003). This result shows that molecular topology of the matrix can have an effect on the diffusion of cyclic polymers. Because cyclic molecules are more compact than linear molecules, it has been argued that circles would form entanglements less effectively (Brown and Szamel, 1998).
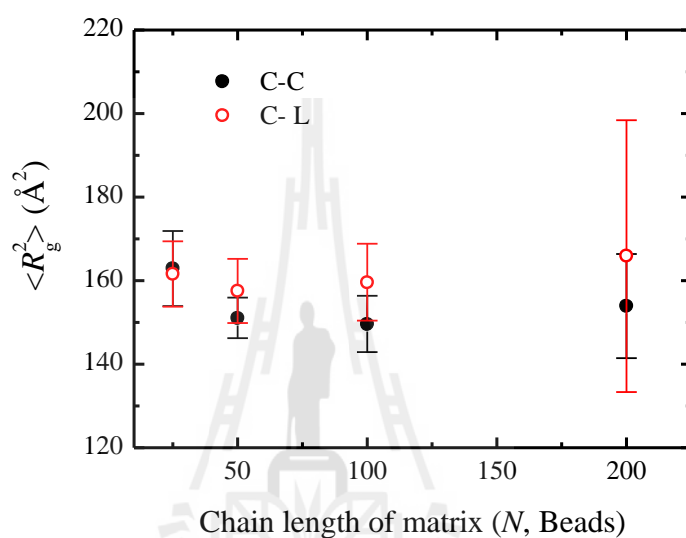
Figure 5.14 The mean-square radius of gyration ($\langle R_g^2 \rangle$) of cyclic PEO ($N = 100$) in cyclic matrix (filled circles), and linear matrix (open circles) as a function of matrix chain length.
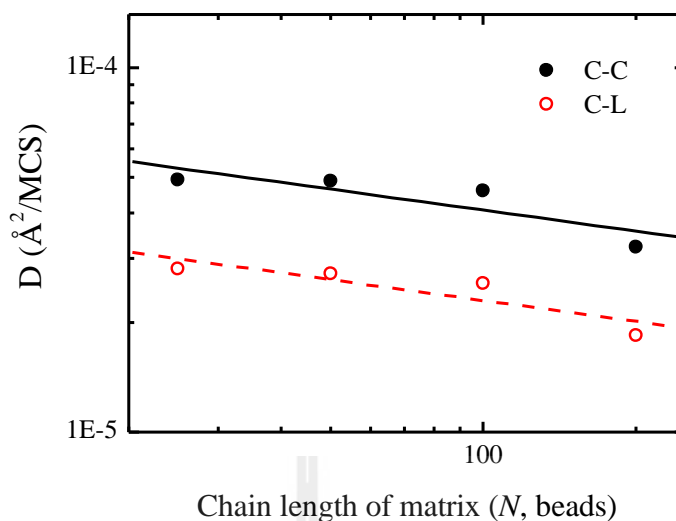
Figure 5.15 Diffusion coefficients of cyclic PEO ($N = 100$) in cyclic matrix (filled circles), and linear matrix (open circles) as a function of matrix chain length.

5.7 Conclusion

A lattice Monte Carlo (MC) simulation of coarse-grained polymer model was developed to study the conformation and diffusion of cyclic and linear poly(ethylene oxide), PEO, blends, at 373 K for $N = 25$ to 200 beads. The results suggest that large cyclic molecules in the condensed system have smaller dimensions than those of linear chains with the same molecular weight. The diffusion coefficients of cyclic chains were higher than linear chains at high molecular weight. The linear chains were slowed down by the existence of entanglements. In contrast, cyclic molecules do not an experience the entanglement at this N due to their smaller size, which isolated them from other neighboring molecules. At the same molecular size (same $\langle R_g^2 \rangle$ value) the diffusion of linear chains is always larger than that of cyclic molecules. This is

expected from an increase almost 2N for cyclic molecules to have the same molecular size as the linear analog.

For the blend of cyclic/linear chains, the sizes of linear and cyclic polymers are independent of the blend composition. As the linear fraction increases, the diffusivities of both cyclic (D_C) and linear (D_L) decrease. In comparison, D_C drops more than D_L especially at longer chain length.

The molecular topology of the matrix can have an effect on the diffusion of cyclic polymers. Because cyclic molecules are more compact than that of linear molecules, it has been argued that cyclic would form entanglements less effectively.
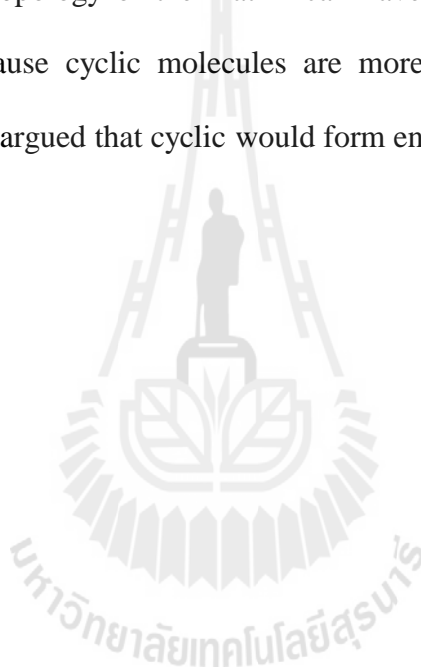
CHAPTER VI

CONCLUSION

This main purpose of this research in addition toward an application biomedical application is to study the structures of the physical polymer hydrogel at the atomistic and molecular level by both experimental and computational approaches, at the atomistic level, MD simulations of calcium ion in small solvent molecules including water, ethanol, and isopropanol, two synthetic polymers i.e. poly(vinyl alcohol) (PVA) poly(acrylic acid), (PAA), two natural polymers i.e. pectin (polygalacturonate), and alginate (polyguluronate) were performed to obtain the solvation structure around calcium cation. Theoretical EXAFS spectra were also computed and compared with experimental EXAFS spectra with good agreement both in k and r space. Ca^{2+}–Cl^- contact ion pairing was also examined. The MD results indicated that the first coordination shell of Ca^{2+} ion (at r ≤ 2.75 Å) in water, ethanol, isopropanol, PVA, and PAA includes only oxygen with very small and unimportant amount of chloride ion. The experimental EXAFS results indicated that, for dilute composition (with Ca^{2+}:O ratio = 1:50, 1:25, and 1:17) there is no contact Ca^{2+}– Cl^- pair and the ion environment is nearly independent of salt concentration. The complexation of Ca^{2+} ion with oxygen is a short range interaction and influences only the local structures of PVA and PAA chain. For calcium ion in pectin and alginate, the results shown that the O1-, O2h, and O2e groups were located within the first shell of the Calcium ion (r ≤ 2.75 Å). The interaction between the O1- groups and

calcium ion is the strongest compared to those between the O2h or O2e groups and calcium ion. Due to the strong interaction between Ca^{2+} ion and polymer, Ca^{2+} ion can act as a transient cross-linker to enlarge the interaction of functional groups of these polysaccharides. Ca^{2+} ion was wrapped mostly by seven oxygen atoms from four polysaccharide chains. Ca^{2+} ions were trapped within the chelation structure between polysaccharide chains corresponding to a stable Ca^{2+}/polymer complex formation.

In addition, Polymer hydrogels of PAA/PVA have been prepared through thermal crosslinking condition in order to have stable materials not having leaching crosslinking agents. ATR-FTIR spectroscopy, swelling properties, Rheological properties, and glass transition temperature of the films were investigated. DSC of the blends films showed only a single glass transition temperature (Tg) for each sample, indicating the good miscibility between PAA and PVA. The FTIR spectra analysis showed that the interaction hydrogen bonds and ester bonds in PAA/PVA blends system were formed. PAA/PVA hydrogels exhibit a solid-like mechanical spectrum; that is, $G' > G''$ throughout the experimentally accessible frequency range. These data support that PAA-PVA crosslink can occur in polymer blend system. The more PAA content in the hydrogels caused the higher swelling ratio in pH 7.4 phosphate buffer solution. Meanwhile, we can also see that swelling ratio decreased with increasing PVA. This was because the interaction between OH and COOH to form ester bonds was decreased the number of hydrophilic COOH and increased the number of nodes of networks.

To understand the other type physical polymer hydrogel caused by chain entangled networking structure at the molecular level, a novel Monte Carlo (MC) simulation of coarse-grained polymer model was developed to investigate the

properties of linear and cyclic poly(ethylene oxide) (PEO) both in pure component and their mixtures. PEO was chosen as the subject of this study for variety of reasons. (1) Linear PEO has low entanglement molecular weight (Me ~ 2 kg/mol) and critical molecular weight for entanglement (Mc ~ 5.87 kg/mol), which means that unentangled and entangled regimes can be studied by simulation. (2) PEO structure is not too complicated for mapping in to coarse-grained beads using our Monte Carlo simulation method and (3) the melt dynamics of cyclic POE or its blends with linear had not yet conclusively been reported in the literatures.

Monte Carlo (MC) simulation of coarse-grained PEO model was then developed to study the conformation and diffusion of cyclic and linear PEO blends at 373 K for N = 25 - 200 beads (each bead representing either CH_2CH_2 or CH_2O unit). The results suggest that large cyclic molecules in the condensed system have smaller dimensions than those of linear chains with the same molecular weight. The diffusion coefficients of cyclic chains were higher than that of linear chains at high molecular weight. The linear chains are slowed down by an existence of chain entanglement. In contrast, cyclic molecules do not experience chain entanglement at this N due to their smaller size, which isolates them from other neighboring molecules. At the same molecular size (same $\langle R_g^2 \rangle$ value) the diffusion of linear chains is always larger than the cyclic molecules.

For the cyclic/linear chains blend, the sizes of linear and cyclic polymers are independent of the blend composition. As the linear fraction increases, the diffusivities of both cyclic (D_C) and linear (D_L) decrease. In comparison, D_C drops more than D_L especially at longer chain length. The molecular topology of the matrix for cyclic/cyclic (C/C) and cyclic/linear (C/L) can have an effect on the diffusion of

the probed cyclic PEO. Because cyclic polymers are more compact shape than the linear analogs, it has been argued that cyclic polymer would form entanglements less effectively and result in larger mobility of cyclic polymer in C/C than that of C/L system.

REFERENCES
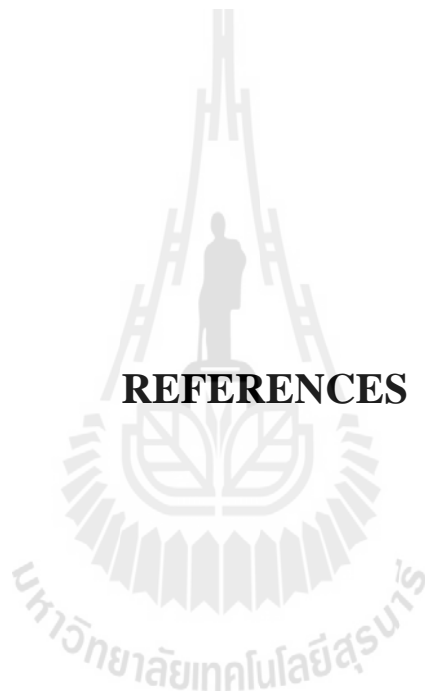
REFERENCES

Abe, A., and Mark, J.E. (1976). Conformational energies and the random-coil dimensions and dipole moments of the polyoxides CH3O[(CH2)yO]xCH3. **J. Am. Chem. Soc.** 98: 6468-6476.

Allen, M.P., and Tildeslet, D.J. (1987). **Computer Simulation of Liquids**. 1st ed. Oxford University Press, New York, 385p.

Allen, M.P. (2004). Introduction to molecular dynamics simulation [On-line]. Available: http://dasher.wustl.edu/chem478/reading/md-intro-2.pdf.

Almdal, K., Dyre, J., Hvidt, S., and Kramer, O. (1993). Towards a phenomenological definition of the term "gel". **Polym. Gels and Networks.** 1: 5-17.

Ananth, A.N., Daniel, S.C.G.K., Sironmani, T.A., and Umapathi, S. (2011). PVA and BSA stabilized silver nanoparticles based surface–enhanced plasmon resonance probes for protein detection. **Colloids Surf., B.** 85: 138-144.

Andrade, J.R., Raphael, E., and Pawlicka, A. (2009). Plasticized pectin-based gel electrolytes. **Electrochim. Acta.** 54: 6479-6483.

Anspoks, A., and Kuzmin, A. (2011). Interpretation of the Ni K-edge EXAFS in nanocrystalline nickel oxide using molecular dynamics simulations. **J. Non-Cryst. Solids.** 357: 2604-2610.

Antonietti, M., Coutandin, J., Gruetter, R., and Sillescu, H. (1984). Diffusion of labeled macromolecules in molten polystyrenes studied by a holographic grating technique. **Macromolecules.** 17: 798-802.

Arrighi, V., Gagliardi, S., Dagger, A.C., Semlyen, J.A., Higgins, J.S., and Shenton, M.J. (2004). Conformation of Cyclics and Linear Chain Polymers in Bulk by SANS. **Macromolecules.** 37: 8057-8065.

Bae, Y., and Kataoka, K. (2006). Significant enhancement of antitumor activity and bioavailability of intracellular pH-sensitive polymeric micelles by folate conjugation. **J. Controlled Release.** 116: e49-e50.

Basiuk, E.V., Anis, A., Bandyopadhyay, S., Alvarez-Zauco, E., Chan, S.L.I., and Basiuk, V.A. (2009). Poly(vinyl alcohol)/CNT composites: An effect of cross-linking with glutaraldehyde. **Superlattices Microstruct.** 46: 379-383.

Beaman, D.K., Robertson, E.J., and Richmond, G.L. (2012). Metal Ions: Driving the Orderly Assembly of Polyelectrolytes at a Hydrophobic Surface. **Langmuir.** 28: 14245-14253.

Bhargav, P.B., Mohan, V.M., Sharma, A.K., and Rao, V.V.R.N. (2009). Investigations on electrical properties of (PVA:NaF) polymer electrolytes for electrochemical cell applications. **Curr. Appl Phys.** 9: 165-171.

Borodin, O., and Smith, G.D. (1998). Molecular Dynamics Simulations of Poly(ethylene oxide)/LiI Melts. 1. Structural and Conformational Properties. **Macromolecules.** 31: 8396-8406.

Brown, S., and Szamel, G. (1998). Computer simulation study of the structure and dynamics of ring polymers. **J. Chem. Phys.** 109: 6184-6192.

Chen, P. (2005). Self-assembly of ionic-complementary peptides: a physicochemical viewpoint. **Colloids Surf., A.** 261: 3-24.

Chen, S., Li, Y., Guo, C., Wang, J., Ma, J., Liang, X., Yang, L.-R., and Liu, H.-Z. (2007). Temperature-Responsive Magnetite/PEO−PPO−PEO Block

Copolymer Nanoparticles for Controlled Drug Targeting Delivery. **Langmuir.** 23: 12669-12676.

Chen, X., Martin, B.D., Neubauer, T.K., Linhardt, R.J., Dordick, J.S., and Rethwisch, D.G. (1995). Enzymatic and chemoenzymatic approaches to synthesis of sugar-based polymer and hydrogels. **Carbohydr. Polym.** 28: 15-21.

Chialvo, A.A., and Simonson, J.M. (2003). The structure of CaCl[sub 2] aqueous solutions over a wide range of concentration. Interpretation of diffraction experiments via molecular simulation. **J. Chem. Phys.** 119: 8052-8061.

Cho, J., and Mattice, W.L. (1997). Estimation of Long-Range Interaction in Coarse-Grained Rotational Isomeric State Polyethylene Chains on a High Coordination Lattice. **Macromolecules.** 30: 637-644.

Cho, J.D., Lyoo, W.S., Chvalun, S.N., and Blackwell, J. (1999). X-ray Analysis and Molecular Modeling of Poly(vinyl alcohol)s with Different Stereoregularities. **Macromolecules.** 32: 6236-6241.

Clark, A., and Ross-Murphy, S. (1987). Structural and mechanical properties of biopolymer gels. **Biopolymers**, Springer Berlin Heidelberg. 83: 57-192.

Connal, L.A., Li, Q., Quinn, J.F., Tjipto, E., Caruso, F., and Qiao, G.G. (2008). pH-Responsive Poly(acrylic acid) Core Cross-Linked Star Polymers: Morphology Transitions in Solution and Multilayer Thin Films. **Macromolecules.** 41: 2620-2626.

Corkhill, P.H., Hamilton, C.J., and Tighe, B.J. (1989). Synthetic hydrogels VI. Hydrogel composites as wound dressings and implant materials. **Biomaterials.** 10: 3-10.

Cosgrove, T., Griffiths, P.C., Hollingshurst, J., Richards, R.D.C., and Semlyen, J.A. (1992). Self-diffusion and spin-spin relaxation in cyclic and linear polydimethylsiloxane melts. **Macromolecules.** 25: 6761-6764.

Cosgrove, T., Turner, M.J., Griffiths, P.C., Hollingshurst, J., Shenton, M.J., and Semlyen, J.A. (1996). Self-diffusion and spin-spin relaxation in blends of linear and cyclic polydimethylsiloxane melts. **Polymer.** 37: 1535-1540.

Curtiss, L.A., and Gordon, M.S. (2004). **Computational materials chemistry: Methods and applications.** 1st ed. Kluwer Academic Publishers, Netherlands, 377p.

D'Angelo, P., Nola, A.D., Giglio, E., Mangoni, M., and Pavel, N.V. (1995). EXAFS Study of Micellar Aggregates of Bile Acid Rubidium Salts. **J. Phys. Chem.** 99: 5471-5480.

D'Angelo, P., and Pavel, N.V. (1999). Evidence of three-body correlation functions in Rb[sup +] and Sr[sup 2+] acetonitrile solutions. **J. Chem. Phys.** 111: 5107-5115.

D'Angelo, P., Di Nola, A., Filipponi, A., Pavel, N.V., and Roccatano, D. (1994). An extended x-ray absorption fine structure study of aqueous solutions by employing molecular dynamics simulations. **J. Chem. Phys.** 100: 985-994.

D'Angelo, P., Di Nola, A., Mangoni, M., and Pavel, N.V. (1996). An extended x-ray absorption fine structure study by employing molecular dynamics simulations: Bromide ion in methanolic solution. **J. Chem. Phys.** 104: 1779-1790.

D'Angelo, P., Petit, P.-E., and Pavel, N.V. (2004). Double-Electron Excitation Channels at the Ca2+ K-Edge of Hydrated Calcium Ion. **J. Phys. Chem. B.** 108: 11857-11865.

Dang, L.X., Schenter, G.K., and Fulton, J.L. (2003). EXAFS Spectra of the Dilute Solutions of Ca2+ and Sr2+ in Water and Methanol. **J. Phys Chem. B.** 107: 14119-14123.

Dang, L.X., Schenter, G.K., Glezakou, V.-A., and Fulton, J.L. (2006). Molecular Simulation Analysis and X-ray Absorption Measurement of Ca2+, K+ and Cl- Ions in Solution. **J. Phys. Chem. B.** 110: 23644-23654.

De La Rosa, A., Heux, L., Cavaillé, J.Y., and Mazeau, K. (2002). Molecular modeling of the mobility of poly(allyl alcohol), PAA, and poly(vinyl alcohol), PVA. **Polymer.** 43: 5665-5677.

Di Cicco, A., Minicucci, M., and Filipponi, A. (1997). New Advances in the Study of Local Structure of Molten Binary Salts. **Phys. Rev. Lett.** 78: 460-463.

Di Cicco, A., Rosolen, M.J., Marassi, R., Tossici, R., Filipponi, A., and Rybicki, J. (1996). Short-range order in solid and liquid KBr probed by EXAFS. **J. Phys. Condens. Matter.** 8: 10779-10798.

Dodgson, K., and Semlyen, J.A. (1977). Studies of cyclic and linear poly(dimethyl siloxanes): 1. Limiting viscosity number-molecular weight relationships. **Polymer.** 18: 1265-1268.

Dong, H., Hyun, J.-K., Rhodes, C.P., Frech, R., and Wheeler, R.A. (2002). Molecular Dynamics Simulations and Vibrational Spectroscopic Studies of Local Structure in Tetraglyme:Sodium Triflate ($CH_3O(CH_2CH_2O)_4CH_3$: $NaCF_3SO_3$) Solutions. **J. Phys. Chem. B.** 106: 4878-4885.

Doruker, P., Rapold, R.F., and Mattice, W.L. (1996). Rotational isomeric state models for polyoxyethylene and polythiaethylene on a high coordination lattice. **J. Chem. Phys.** 104: 8742-8749.

Eichenbaum, G.M., Kiser, P.F., Dobrynin, A.V., Simon, S.A., and Needham, D. (1999). Investigation of the Swelling Response and Loading of Ionic Microgels with Drugs and Proteins: The Dependence on Cross-Link Density. **Macromolecules.** 32: 4867-4878.

Ende, M.T.A., and Peppas, N.A. (1996). Transport of ionizable drugs and proteins in crosslinked poly(acrylic acid) and poly(acrylic acid-co-2-hydroxyethyl methacrylate) hydrogels. I. Polymer characterization. **J. Appl. Polym. Sci.** 59: 673-685.

Fan, C.F., and Hsu, S.L. (1991). Application of the molecular simulation technique to generate the structure of an aromatic polysulfone system. **Macromolecules.** 24: 6244-6249.

Freifelder, D., Kleinschmidt, A. K., Sinscheimer, R. L. (1964). Electron Microscopy of Single-Stranded DNA: Circularity of DNA of Bacteriophage ϕX174. **Science**. 146: 254-255.

Filipponi, A., and Di Cicco, A. (1995). Short-range order in crystalline, amorphous, liquid, and supercooled germanium probed by x-ray-absorption spectroscopy. **Phys. Rev. B.** 51: 12322-12336.

Flory, P.J. (1988). **The Statistical Mechanics of Chain Molecules**. New York: Hanser.

Fulton, J.L., Heald, S.M., Badyal, Y.S., and Simonson, J.M. (2003). Understanding the Effects of Concentration on the Solvation Structure of Ca^{2+} in Aqueous

Solution. I: The Perspective on Local Structure from EXAFS and XANES. **J. Phys. Chem. A.** 107: 4688-4696.

Fundueanu, G., Constantin, M., and Ascenzi, P. (2008). Preparation and characterization of pH- and temperature-sensitive pullulan microspheres for controlled release of drugs. **Biomaterials.** 29: 2767-2775.

Galindo-Rodríguez, S.A., Puel, F., Briançon, S., Allémann, E., Doelker, E., and Fessi, H. (2005). Comparative scale-up of three methods for producing ibuprofen-loaded nanoparticles. **Eur. J. Pharm. Sci.** 25: 357-367.

Ganji, F., Vasheghani-Farahani, S., and Vasheghani-Farahani, E. (2010). Theoretical Description of Hydrogel Swelling:A Review. **Iran. Polym. J.** 19: 375-398.

Gibson, H.W., Bheda, M.C., Engen, P., Shen, Y.X., Sze, J., Zhang, H., Gibson, M.D., Delaviz, Y., and Lee, S.-H. (1994). Synthesis and Characterization of Large (30-60-Membered) Aliphatic Crown Ethers. **J. Org. Chem.** 59: 2186-2196.

Ghi, P., Hill, D.J.T., and Whittaker, A.K. (2000). Water sorption by poly(tetrahydrofurfuryl methacrylate-co-2-hydroxyethyl methacrylate). I. A mass-uptake study. **J. Polym. Sci., Part B: Polym. Phys.** 38: 1939-1946.

Glezakou, V.-A., Chen, Y., Fulton, J., Schenter, G., and Dang, L. (2006). Electronic structure, statistical mechanical simulations, and EXAFS spectroscopy of aqueous potassium. **Theor. Chem Acc.** 115: 86-99.

Grulke, E.A. (1999). Solubility parameter values. **Polymer Handbook**. J. Brandrup and E.H. Immergut. New York, Wiley.

Gudeman, L.F., and Peppas, N.A. (1995). pH-sensitive membranes from poly(vinyl alcohol)/poly(acrylic acid) interpenetrating networks. **J. Mem. Sci.** 107: 239-248.

Hasimi, A., Stavropoulou, A., Papadokostaki, K.G., and Sanopoulou, M. (2008). Transport of water in polyvinyl alcohol films: Effect of thermal treatment and chemical crosslinking. **Eur. Polym. J.** 44: 4098-4107.

He, C., Kim, S.W., and Lee, D.S. (2008). In situ gelling stimuli-sensitive block copolymer hydrogels for drug delivery. **J. Controlled Release.** 127: 189-207.

Hewish, N.A., Neilson, G.W., and Enderby, J.E. (1982). Environment of Ca^{2+} ions in aqueous solvent. **Nature.** 297: 138-139.

Hoare, T.R., and Kohane, D.S. (2008). Hydrogels in drug delivery: Progress and challenges. **Polymer.** 49: 1993-2007.

Hoffman, A.S. (2002). Hydrogels for biomedical applications. **Adv. Drug Delivery Rev.** 54: 3-12.

Hoffman, A.S. (2012). Hydrogels for biomedical applications. **Adv. Drug Delivery Rev.** 64: 18-23.

Hoffmann, M.M., Darab, J.G., Palmer, B.J., and Fulton, J.L. (1999). A Transition in the Ni2+ Complex Structure from Six- to Four-Coordinate upon Formation of Ion Pair Species in Supercritical Water: An X-ray Absorption Fine Structure, Near-Infrared, and Molecular Dynamics Study. **J. Phys. Chem. A.** 103: 8471-8482.

Hua, S., Ma, H., Li, X., Yang, H., and Wang, A. (2010). pH-sensitive sodium alginate/poly(vinyl alcohol) hydrogel beads prepared by combined Ca^{2+} crosslinking and freeze-thawing cycles for controlled release of diclofenac sodium. **Int. J. Biol. Macromol.** 46: 517-523.

Huh, K.M., Ooya, T., Lee, W.K., Sasaki, S., Kwon, I.C., Jeong, S.Y., and Yui, N. (2001). Supramolecular-Structured Hydrogels Showing a Reversible Phase Transition by Inclusion Complexation between Poly(ethylene glycol) Grafted Dextran and α-Cyclodextrin. **Macromolecules.** 34: 8657-8662.

Huynh, D.P., Nguyen, M.K., Pi, B.S., Kim, M.S., Chae, S.Y., Lee, K.C., Kim, B.S., Kim, S.W., and Lee, D.S. (2008). Functionalized injectable hydrogels for controlled insulin delivery. **Biomaterials.** 29: 2527-2534.

Hyun, J.-K., Dong, H., Rhodes, C.P., Frech, R., and Wheeler, R.A. (2001). Molecular Dynamics Simulations and Spectroscopic Studies of Amorphous Tetraglyme ($CH_3O(CH_2CH_2O)_4CH_3$) and Tetraglyme:$LiCF_3SO_3$ Structures. **J. Phys. Chem. B.** 105: 3329-3337.

Inger Martínez de, A., Emiliano, M., and Jose-Ramon, S. (2012). Analysis of the Miscibility of Polymer Blends Through Molecular Dynamics Simulations.

Ishizu, K., and Akiyama, Y. (1997). Synthesis of cyclic polyethers. **Polymer.** 38: 491-494.

Jabbari, E., and Nozari, S. (2000). Swelling behavior of acrylic acid hydrogels prepared by γ-radiation crosslinking of polyacrylic acid in aqueous solution. **Eur. Polym. J.** 36: 2685-2692.

Jacob, F.; Wollman, E. L. (1958) Genetic and physical determinations of chromosomal segments in Escherichia coli. **Symp. Soc. Exp. Biol.** 12: 75-92.

Jalilehvand, F., Spångberg, D., Lindqvist-Reis, P., Hermansson, K., Persson, I., and Sandström, M. (2001). Hydration of the Calcium Ion. An EXAFS, Large-

Angle X-ray Scattering, and Molecular Dynamics Simulation Study. **J. Am. Chem. Soc.** 123: 431-441.

Jawalkar, S.S., Adoor, S.G., Sairam, M., Nadagouda, M.N., and Aminabhavi, T.M. (2005). Molecular Modeling on the Binary Blend Compatibility of Poly(vinyl alcohol) and Poly(methyl methacrylate): An Atomistic Simulation and Thermodynamic Approach. **J. Phys. Chem. B.** 109: 15611-15620.

Jawalkar, S.S., and Aminabhavi, T.M. (2006). Molecular modeling simulations and thermodynamic approaches to investigate compatibility/incompatibility of poly(l-lactide) and poly(vinyl alcohol) blends. **Polymer.** 47: 8061-8071.

Jeong, S.-K., Jo, Y.-K., and Jo, N.-J. (2006). Decoupled ion conduction mechanism of poly(vinyl alcohol) based Mg-conducting solid polymer electrolyte. **Electrochim. Acta.** 52: 1549-1555.

Jiang, H., Su, W., Mather, P.T., and Bunning, T.J. (1999). Rheology of highly swollen chitosan/polyacrylate hydrogels. **Polymer.** 40: 4593-4602.

Juntanon, K., Niamlang, S., Rujiravanit, R., and Sirivat, A. (2008). Electrically controlled release of sulfosalicylic acid from crosslinked poly(vinyl alcohol) hydrogel. **Int. J. Pharm.** 356: 1-11.

Kan, M., Wang, F., Xu, J., Crabb, J.W., Hou, J., and McKeehan, W.L. (1993). An Essential Heparin-Binding Domain in the Fibroblast Growth Factor Receptor Kinase. **Science.** 259: 1918-1921.

Kashyap, N., Kumar, N., and Kumar, M.N.V.R. (2005). Hydrogels for Pharmaceutical and Biomedical Applications. **Crit. Rev. Ther. Drug Carr. Syst.** 22: 107-150.

Katime, I., Novoa, R., Díaz de Apodaca, E., and Rodríguez, E. (2004). Release of theophylline and aminophylline from acrylic acid/n-alkyl methacrylate hydrogels. **J. Polym. Scie., Part A: Polym. Chem.** 42: 2756-2765.

Kim, J., Conway, A., and Chauhan, A. (2008). Extended delivery of ophthalmic drugs by silicone hydrogel contact lenses. **Biomaterials.** 29: 2259-2269.

Kurkuri, M.D., and Aminabhavi, T.M. (2004). Poly(vinyl alcohol) and poly(acrylic acid) sequential interpenetrating network pH-sensitive microspheres for the delivery of diclofenac sodium to the intestine. **J. Controlled Release.** 96: 9-20.

Kurkuri, M.D., Nussio, M.R., Deslandes, A., and Voelcker, N.H. (2008). Thermosensitive Copolymer Coatings with Enhanced Wettability Switching. **Langmuir.** 24: 4238-4244.

Lee, K.Y., and Yuk, S.H. (2007). Polymeric protein delivery systems. **Prog. Polym. Sci.** 32: 669-697.

Lee, M.-H., Lin, H.-Y., Chen, H.-C., and Thomas, J.L. (2008). Ultrasound Mediates the Release of Curcumin from Microemulsions. **Langmuir.** 24: 1707-1713.

Lennard-Jones, J.E. (1931). **Cohesion. Proceeding of the Physical Society.** 43: 461-482.

Li, J., Ni, X., and Leong, K.W. (2003). Injectable drug-delivery systems based on supramolecular hydrogels formed by poly(ethylene oxide)s and α-cyclodextrin. **J. Biomed. Mater. Res. Part A.** 65A: 196-202.

Licheri, G., Picacaluga, G., and Pinna, G. (1976). X-ray diffraction study of the average solute species in CaCl2 aqueous solutions. **J. Chem. Phys.** 64: 2437-2441.

Lim, D.W., Nettles, D.L., Setton, L.A., and Chilkoti, A. (2007). Rapid Cross-Linking of Elastin-like Polypeptides with (Hydroxymethyl)phosphines in Aqueous Solution. **Biomacromolecules.** 8: 1463-1470.

Lung Ha, Y., and Chakraborty, A.K. (1994). Characterization of crown ethers as macrocyclic elements for rotaxane preparation: a Monte Carlo simulation. **Chem. Eng. Sci.** 49: 2859-2866.

Manavi-Tehrani, I., Rabiee, M., Parviz, M., Tahriri, M.R., and Fahimi, Z. (2010). Preparation, Characterization and Controlled Release Investigation of Biocompatible pH-Sensitive PVA/PAA Hydrogels. **Macromol. Symp.** 296: 457-465.

Manning, G.S. (1979). **Acc. Chem. Res.** 12: 443-449.

Mathiowetz, A.M. (1994). **Introduction** [On-line]. Available: http://www.wag. caltech.edu/publications/theses/alan/section1_6_0_1.html.

Masuda, K., and Horii, F. (1998). CP/MAS 13C NMR Analyses of the Chain Conformation and Hydrogen Bonding for Frozen Poly(vinyl alcohol) Solutions. **Macromolecules.** 31: 5810-5817.

Mattice, W.L., and Suter, U.W. (1994). **Conformational theory of large molecules: The rotational isomeric state model in macromolecular systems.** New York: Wiley.

McKenna, G.B., and Plazek, D.J. (1986) The viscosity of blends of linear and cyclic molecules of similar molecular mass **Polym. Commun.** 27: 304-306.

McKenna, G.B., Hostetter, B.J., Hadjichristidis, N., Fetters, L.J., and Plazek, D.J. (1989). A study of the linear viscoelastic properties of cyclic polystyrenes using creep and recovery measurements. **Macromolecules.** 22: 1834-1852.

Metropolis, N, Rosenbluth, A.W., Rosenbluth, M.N., Teller, A.H., and Teller, E. (1953). Equation of state calculations by fast computing machines. **J. Chem. Phys.** 21: 1087-1092.

Mohamad, A.A., Mohamed, N.S., Yahya, M.Z.A., Othman, R., Ramesh, S., Alias, Y., and Arof, A.K. (2003). Ionic conductivity studies of poly(vinyl alcohol) alkaline solid polymer electrolyte and its use in nickel–zinc cells. **Solid State Ionics.** 156: 171-177.

Mok, H., Park, J.W., and Park, T.G. (2008). Enhanced Intracellular Delivery of Quantum Dot and Adenovirus Nanoparticles Triggered by Acidic pH via Surface Charge Reversal. **Bioconjugate Chem.** 19: 797-801.

Mu, D., Li, J.-Q., and Zhou, Y.-H. (2011). Modeling and analysis of the compatibility of polystyrene/poly(methyl methacrylate) blends with four inducing effects. **J. mol. Model.** 17: 607-619.

Müller, M., Wittmer, J.P., and Cates, M.E. (1996). Topological effects in ring polymers: A computer simulation study. **Physical Review E.** 53: 5063-5074.

Munjeri, O., Collett, J.H., and Fell, J.T. (1997). Hydrogel beads based on amidated pectins for colon-specific drug delivery: the role of chitosan in modifying drug release. **J. Controlled Release.** 46: 273-278.

Nakamura, K., Maitani, Y., Lowman, A.M., Takayama, K., Peppas, N.A., and Nagai, T. (1999). Uptake and release of budesonide from mucoadhesive, pH-sensitive copolymers and their application to nasal delivery. **J. Controlled Release.** 61: 329-335.

Newville, M. (2001). IFEFFIT : interactive XAFS analysis and FEFF fitting. **J. Synchrotron Rad.** 8: 322-324.

Newville M. (2004). **Fundamentals of XAFS**, http://xafs.org/Tutorials?action= AttachFile&do=get&target=Newville_xas_fundamentals.pdf [14 September 2012].

Nguyen, D.N., Raghavan, S.S., Tashima, L.M., Lin, E.C., Fredette, S.J., Langer, R.S., and Wang, C. (2008). Enhancement of poly(orthoester) microspheres for DNA vaccine delivery by blending with poly(ethylenimine). **Biomaterials.** 29: 2783-2793.

Nguyen, K.T., and West, J.L. (2002). Photopolymerizable hydrogels for tissue engineering applications. **Biomaterials.** 23: 4307-4314.

Nolkrantz, K., Farre, C., Brederlau, A., Karlsson, R.I.D., Brennan, C., Eriksson, P.S., Weber, S.G., Sandberg, M., and Orwar, O. (2001). Electroporation of Single Cells and Tissues with an Electrolyte-filled Capillary. **Anal. Chem.** 73: 4469-4477.

Ohtaki, H., and Radnai, T. (1993). **Chem. Rev.** 93: 1157-1204.

Orrah, D.J., Semlyen, J.A., and Ross-Murphy, S.B. (1988). Studies of cyclic and linear poly(dimethylsiloxanes): 27. Bulk viscosities above the critical molar mass for entanglement. **Polymer.** 29: 1452-1454.

Orwoll, R.A. (1996) In **Physical Properties of Polymers Handbook**; Mark, J. E., Ed.; American Institute of Physics: Woodbury. p. 82.

Owczarek, E., and Hawlicka, E. (2006). Molecular Dynamics Study of CaCl2 in Methanol. **J. Phys. Chem. B.** 110: 22712-22718.

Owczarek, E., Rybicki, M., and Hawlicka, E. (2007). Solvation of Calcium Ions in Methanol−Water Mixtures: Molecular Dynamics Simulation. **J. Phys. Chem. B.** 111: 14271-14278.

Pakula, T., and Geyler, S. (1988). Cooperative relaxations in condensed macromolecular systems. 3. Computer-simulated melts of cyclic polymers. **Macromolecules.** 21: 1665-1670.

Peppas, N.A., Bures, P., Leobandung, W., and Ichikawa, H. (2000). Hydrogels in pharmaceutical formulations. **Eur. J. Pharm. Biopharm.** 50: 27-46.

Peppas, N.A., Hilt, J.Z., Khademhosseini, A., and Langer, R. (2006). Hydrogels in Biology and Medicine: From Molecular Principles to Bionanotechnology. **Adv. Mater.** 18: 1345-1360.

Pillay, V., and Fassihi, R. (1999). In vitro release modulation from crosslinked pellets for site-specific drug delivery to the gastrointestinal tract: I. Comparison of pH-responsive drug release and associated kinetics. **J. Controlled Release.** 59: 229-242.

Ponomariova, T., Melnichenko, Y., Albouy, P.A., and Rault, J. (1997). Influence of the crosslinks density on the crystallization of water in PAA gels. **Polymer.** 38: 3561-3564.

Probst, M.M., Radnai, T., Heinzinger, K., Bopp, P., and Rode, B.M. (1985). Molecular dynamics and x-ray investigation of an aqueous calcium chloride solution. **J. Phys. Chem.** 89: 753-759.

Qi, M., Gu, Y., Sakata, N., Kim, D., Shirouzu, Y., Yamamoto, C., Hiura, A., Sumi, S., and Inoue, K. (2004). PVA hydrogel sheet macroencapsulation for the bioartificial pancreas. **Biomaterials.** 25: 5885-5892.

Qiu, Y., and Park, K. (2001). Environment-sensitive hydrogels for drug delivery. **Adv. Drug Deliv. Rev.** 53(3): 321-339.

Rao, M.A., Steffe, J.F., Eds. (1992) **Viscoelastic Properties of Foods**; Elsevier Applied Science: London, U.K.

Rhim, J.-W. (2004). Physical and mechanical properties of water resistant sodium alginate films. **LWT - Food Science and Technology.** 37: 323-330.

Ritger, P.L., and Peppas, N.A. (1987). A simple equation for description of solute release II. Fickian and anomalous release from swellable devices. **J. Controlled Release.** 5: 37-42.

Robertson, R.M., and Smith, D.E. (2007). Self-Diffusion of Entangled Linear and Circular DNA Molecules: Dependence on Length and Concentration. **Macromolecules.** 40: 3373-3377.

Roccatano, D., Berendsen, H.J.C., and D'Angelo, P. (1998). Assessment of the validity of intermolecular potential models used in molecular dynamics simulations by extended x-ray absorption fine structure spectroscopy: A case study of Sr[sup 2+] in methanol solution. **J. Chem. Phys.** 108: 9487-9497.

Roovers, J. (1988). Viscoelastic properties of polybutadiene rings. **Macromolecules.** 21: 1517-1521.

Ross-Murphy, S.B. (1994). **Rheological methods.** In Physical Techniques for the Study of Food Biopolymers; Ross-Murphy, S. B., Ed.; Blackie Academic & Professional: London, U.K., 343-392.

Roy, I., and Gupta, M.N. (2003). Smart Polymeric Materials: Emerging Biochemical Applications. **Chemistry & Biology.** 10: 1161-1171.

Rubinshtein, M., Colby, R.H. (2003) **Polymer Physics**. Oxford University Press.

Sandolo, C., Matricardi, P., Alhaique, F., and Coviello, T. (2009). Effect of temperature and cross-linking density on rheology of chemical cross-linked guar gum at the gel point. **Food Hydrocolloids.** 23: 210-220.

Shah, N.M., Pool, M.D., and Metters, A.T. (2006). Influence of Network Structure on the Degradation of Photo-Cross-Linked PLA-b-PEG-b-PLA Hydrogels. **Biomacromolecules.** 7: 3171-3177.

Shefer, A., Grodzinsky, A.J., Prime, K.L., and Busnel, J.P. (1993). Novel model networks of poly(acrylic acid): synthesis and characterization. **Macromolecules.** 26: 5009-5014.

Shin, H.S., Kim, S.Y., and Lee, Y.M. (1997). Indomethacin release behaviors from pH and thermoresponsive poly(vinyl alcohol) and poly(acrylic acid) IPN hydrogels for site-specific drug delivery. **J. Appl. Polym. Sci.** 65: 685-693.

Silverstein, R.M., Bassler, G.C., and Morrill, T.C. (1991). **Spectrometric Identification of Organic Compounds**. 5th ed. Wiley, New York, 419p.

Singh, T.J., Ganeshsanjeev, Siddappa, K., and Bhat, S.V. (2004). Large enhancement of the ionic conductivity in an electron-beam-irradiated [poly(ethylene glycol)]xLiClO4 solid polymer electrolyte. **J. Polym. Sci., Part B: Polym. Phys.** 42: 1299-1311.

Smirnov, P., Yamagami, M., Wakita, H., and Yamaguchi, T. (1997). An X-ray diffraction study on concentrated aqueous calcium nitrate solutions at subzero temperatures. **J. Mol. Liq.** 73,74: 305-316.

Spångberg, D., Hermansson, K., Lindqvist-Reis, P., Jalilehvand, F., Sandström, M., and Persson, I. (2000). Model Extended X-ray Absorption Fine Structure

(EXAFS) Spectra from Molecular Dynamics Data for Ca2+ and Al3+ Aqueous Solutions. **J. Phys. Chem. B.** 104: 10467-10472.

Sriamornsak, P., and Kennedy, R.A. (2007). Effect of drug solubility on release behavior of calcium polysaccharide gel-coated pellets. **Eur. J. Pharm. Sci.** 32: 231-239.

Sriamornsak, P., and Kennedy, R.A. (2008). Swelling and diffusion studies of calcium polysaccharide gels intended for film coating. **Int. J. Pharm.** 358: 205-213.

Stringer, J.L., and Peppas, N.A. (1996). Diffusion of small molecular weight drugs in radiation-crosslinked poly(ethylene oxide) hydrogels. **J. Controlled Release.** 42: 195-202.

Sun, H. (1998). COMPASS: An ab Initio Force-Field Optimized for Condensed-Phase ApplicationsOverview with Details on Alkane and Benzene Compounds. **J. Phys. Chem. B.** 102: 7338-7364.

Sun, T., Yu, G.-E., Price, C., Booth, C., Cooke, J., and Ryan, A.J. (1995). Cyclic polyethers. **Polymer.** 36: 3775-3778.

Tamilvanan, S., Venkateshan, N., and Ludwig, A. (2008). The potential of lipid- and polymer-based drug delivery carriers for eradicating biofilm consortia on device-related nosocomial infections. **J. Controlled Release.** 128: 2-22.

Tang, Y., and Singh, J. (2008). Controlled delivery of aspirin: Effect of aspirin on polymer degradation and in vitro release from PLGA based phase sensitive systems. **Int. J. Pharm.** 357: 119-125.

Vázquez-Torres, H., Cauich-Rodríguez, J.V., and Cruz-Ramos, C.A. (1993). Poly(vinyl alcohol)/poly(acrylic acid) blends: Miscibility studies by DSC

and characterization of their thermally induced hydrogels. **J. Appl. Polym. Sci.** 50: 777-792.

von Meerwall, E., Ozisik, R., Mattice, W.L., and Pfister, P.M. (2003). Self-diffusion of linear and cyclic alkanes, measured with pulsed-gradient spin-echo nuclear magnetic resonance. **J. Chem.Phy.** 118: 3867-3873.

Wang, J., and Lei, J. (2012). Influence of DC electric field on both crystalline structure and conductivity of poly(ethylene oxide)10:LiClO4 electrolyte. **J. Polym. Sci., Part B: Polym. Phys.** 50: 656-667.

Wang, Y.-C., Liu, X.-Q., Sun, T.-M., Xiong, M.-H., and Wang, J. (2008). Functionalized micelles from block copolymer of polyphosphoester and poly(ε-caprolactone) for receptor-mediated drug delivery. **J. Controlled Release.** 128: 32-40.

Watanabe, M., Kawano, K., Toma, K., Hattori, Y., and Maitani, Y. (2008). In vivo antitumor activity of camptothecin incorporated in liposomes formulated with an artificial lipid and human serum albumin. **J. Controlled Release.** 127: 231-238.

Westedt, U., Kalinowski, M., Wittmar, M., Merdan, T., Unger, F., Fuchs, J., Schäller, S., Bakowsky, U., and Kissel, T. (2007). Poly(vinyl alcohol)-graft-poly(lactide-co-glycolide) nanoparticles for local delivery of paclitaxel for restenosis treatment. **J. Controlled Release.** 119: 41-51.

Wichterle, O., and Lim, D. (1960). Hydrophilic Gels for Biological Use. **Nature.** 185: 117-118.

Witkowska, A., Rybicki, J., Panfilis, S.D., and Cicco, A.D. (2006). The structure of liquid lead: EXAFS and MD studies. **J. Non-Cryst. Solids.** 352: 4351-4355.

Wolf, R.M., and Suter, U.W. (1984). Conformational characteristics of poly(vinyl alcohol). **Macromolecules.** 17: 669-677.

Wu, J., Morimyo, M., Hongo, E., Higashi, T., Okamoto, M., Kawano, A., and Ohmachi, Y. (2006). Radiation-induced germline mutations detected by a direct comparison of parents and first-generation offspring DNA sequences containing SNPs. **Mutation Research/Fundamental and Molecular Mechanisms of Mutagenesis.** 596: 1-11.

Xu, G., and Mattice, W.L. (2002). Monte Carlo simulation of the crystallization and annealing of a freestanding thin film of n-tetracontane. **J. Chem. Phys.** 116: 2277-2283.

Yamaguchi, T., Hayashi, S., and Ohtaki, H. (1989). X-ray diffraction study of calcium(II) chloride hydrate melts: CaCl2.cntdot.RH2O (R = 4.0, 5.6, 6.0, and 8.6). **Inorg. Chem.** 28: 2434-2439.

Yang, D., Li, Y., and Nie, J. (2007). Preparation of gelatin/PVA nanofibers and their potential application in controlled release of drugs. **Carbohydr. Polym.** 69: 538-543.

Zabinsky, S.I., Rehr, J.J., Ankudinov, A., Albers, R.C., and Eller, M.J. (1995). Multiple-scattering calculations of x-ray-absorption spectra. **Phys. Rev. B.** 52: 2995-3009.

Zavitsas, A.A. (2005). Aqueous Solutions of Calcium Ions: Hydration Numbers and the Effect of Temperature. **J. Phys. Chem. B.** 109: 20636-20640.

Zhang, Q.G., Liu, Q.L., Zhu, A.M., Xiong, Y., and Ren, L. (2009). Pervaporation performance of quaternized poly(vinyl alcohol) and its crosslinked membranes for the dehydration of ethanol. **J. Membr. Sci.** 335: 68-75.

APPENDIX

APPENDIX

IR ABSORPTION FREQUENCIES OF FUNCTIONAL

GROUPS

A.1 Characteristic IR Absorption Frequencies of Organic Functional Groups[a]

Functional Group	Type of Vibration	Characteristic Absorptions (cm-1)	Intensity
Alcohol			
O-H	(stretch, H-bonded)	3200-3600	strong, broad
O-H	(stretch, free)	3500-3700	strong, sharp
C-O	(stretch)	1050-1150	strong
Alkane			
C-H	stretch	2850-3000	strong
-C-H	bending	1350-1480	variable
Alkene			
=C-H	stretch	3010-3100	medium
=C-H	bending	675-1000	strong

C=C	stretch	1620-1680	variable

Alkyl Halide

C-F	stretch	1000-1400	strong
C-Cl	stretch	600-800	strong
C-Br	stretch	500-600	strong
C-I	stretch	500	strong

Alkyne

C-H	stretch	3300	strong,sharp
$-C\equiv C-$	stretch	2100-2260	variable

Amine

N-H	stretch	3300-3500	medium
C-N	stretch	1080-1360	medium-weak
N-H	bending	1600	medium

Aromatic

C-H	stretch	3000-3100	medium
C=C	stretch	1400-1600	medium-weak, multiple bands

Analysis of C-H out-of-plane bending can often distinguish substitution patterns

Carbonyl		Detailed Information on Carbonyl IR	
C=O	stretch	1670-1820	strong

(conjugation moves absorptions to lower wave numbers)

Ether			
C-O	stretch	1000-1300 (1070-1150)	strong
Nitrile			
CN	stretch	2210-2260	medium
Nitro			
N-O	stretch	1515-1560 & 1345-1385	strong, two bands

(a) Silverstein, R.M., Bassler, G.C., and Morrill, T.C. (1991). **Spectrometric Identification of Organic Compounds**. 5th ed. Wiley, New York, 419p.
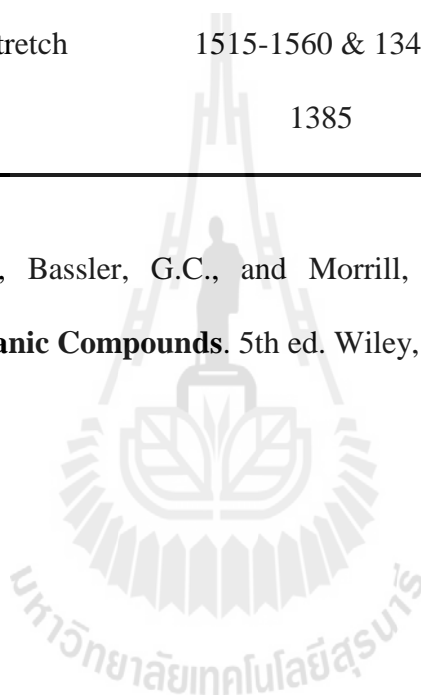
A.2 IR Absorption Frequencies of Functional Groups Containing a Carbonyl (C=O)[a]

Functional Group	Type of Vibration	Characteristic Absorptions (cm-1)	Intensity
Carbonyl			
C=O	stretch	1670-1820	strong
(conjugation moves absorptions to lower wave numbers)			
Acid			
C=O	stretch	1700-1725	strong
O-H	stretch	2500-3300	strong, very broad
C-O	stretch	1210-1320	strong
Aldehyde			
C=O	stretch	1740-1720	strong
=C-H	stretch	2820-2850 & 2720-2750	medium, two peaks
Amide			
C=O	stretch	1640-1690	strong
N-H	stretch	3100-3500	unsubstituted have two bands
N-H	bending	1550-1640	

Anhydride			
C=O	stretch	1800-1830 & 1740-1775	two bands
Ester			
C=O	stretch	1735-1750	strong
C-O	stretch	1000-1300	two bands or more
Ketone			
acyclic	stretch	1705-1725	strong
cyclic	stretch	3-membered - 1850	strong
		4-membered - 1780	
		5-membered - 1745	
		6-membered - 1715	
		7-membered - 1705	
α,β- unsaturated	stretch	1665-1685	strong
aryl ketone	stretch	1680-1700	strong

(a) Silverstein, R.M., Bassler, G.C., and Morrill, T.C. (1991). **Spectrometric Identification of Organic Compounds**. 5th ed. Wiley, New York, 419p.

CURRICULUM VITAE

Name   Miss Kesorn Merat

Date of Birth   7 February 1983

Place of Birth   Roi-Et, Thailand

Education:

2002 - 2005   B.Sc. Chemistry (Second Class Honors), Mahasarakham University, Thailand

2006 - 2007   Grad. Dip. (Teaching Profession), Mahasarakham University, Thailand

Publications

1. **Merat, K.,** Chaodamrongsakul, J., Tanthanuch, W., Vao-soongnern V. (2013). J. Non-Cryst. Solids, 371-372: 47-52.

Grants and Fellowships

1. Bachelor Degree and Graduate Diploma grant from The Institute for the Promotion of Teaching Science and Technology (IPST), Thailand. Name of scholarship "The Project for the Promotion of Science and Mathematics Talented Teachers (PSMT)" (2002 - 2006).

2. Ph.D. grant (GS-50D04) from Synchrotron Light Research Institute (Public Organization): SLRI, Thailand (2007 - 2013).

3. Japan Student Services Organization (JASSO) offers Student Exchange Support Program, Scholarship for Short-term Study in Japan (2010).